SHEAR-INDUCED TRANSPORT PROPERTIES OF GRANULAR MATERIAL FLOWS

Thesis by

Shu-San Hsiau

In Partial Fulfillment of the Requirements

for the Degree of

Doctor of Philosophy

California Institute of Technology

Pasadena, California

1993

(Submitted January 5, 1993)

Acknowledgements

I would like to thank my advisor, Professor Melany Hunt. She has guided my research and taught me the spirit of research. Without her encouragement and patience, this research could not be achieved. I also want to thank Professors Rolf Sabersky and Christopher Brennen. They are always nice to me and willingly discuss any problems with me. I wish to express my appreciation to Professor Allan Acosta for his invaluable advice.

I am grateful to Professors Shih-Tuen Lee, Jing T. Kuo and Shyan-Fu Chou at National Taiwan University who taught me the fundamentals of Thermo-Fluids when I was undergraduate student. I cannot forget Gary Fan's help when I first arrived United States four and a half years ago.

I am pleased to acknowledge Marty Gould who helped me with the machinery work. Thanks to Brian Rague for his help in electronic instruments. Special thanks go to Cecilia Lin who aided me in preparing some figures.

I would especially like to thank my parents. They taught me how to be a good person from when I was a child. Without them, I would not have any accomplishments. My deepest thanks go to my girlfriend, Jen-Fen Su. Although she is in Taiwan, far away from here, she continues to give me support, motivation and love.

Abstract

A granular flow is a two-component flow with an assembly of discrete solid particles dispersed in a fluid. Because of the similarity between the random motion of particles in a granular flow and the motion of molecules in a gas, the dense-gas kinetic theory has been broadly employed to analyze granular flows. However, most research only discusses aspects of momentum transport; three issues have received less attention: the diffusion process, the heat transfer problem, and the behavior of binary mixtures. The current research emphasizes these aspects.

A granular flow diffusion experiment was conducted in a vertical channel to investigate the effects that result in mixing of the material. The mean velocities, the longitudinal fluctuating velocities, and the mixing-layer thickness were measured. A simple analysis based on the diffusion equation shows that the thickness of the mixing layer increases with the square-root of downstream distance and depends on the magnitude of the velocity fluctuations relative to the mean velocity. The experimental velocity profiles were also compared with profiles calculated from theoretical analysis based on kinetic theory.

The analytical relations were developed for the flow-induced particle diffusivity and the thermal conductivity based on dense-gas kinetic theory. The two coefficients

were found to increase with the square-root of the granular temperature, a term that quantifies the specific kinetic energy of the flow. The theoretical particle diffusivity was used to compare with the current experimental measurements involving the granular flow mixing layer. The analytical expression for the effective thermal conductivity was also compared with experimental measurements. The differences between the predictions and the measurements suggest limitations in some of the underlying kinetic-theory assumptions.

The constitutive relations were presented for a binary-mixture of granular materials as derived from the revised Enskog theory. The current research focuses on the process of granular thermal diffusion — a diffusion process resulting from the granular temperature gradient. A granular flow of binary-mixtures in an oscillatory no-flow system, in a sheared system, and in a vertical channel were examined, and indicated a complete segregation when granular thermal diffusion effect was sufficiently large.

Table of Contents

List of Figures

Chapter 1

Introduction

A granular material is an assembly of a large number of discrete solid components that are dispersed in a fluid. This class of two-phase flow occurs in many industrial situations such as the transport of ore, coal, mineral concentrate, sand, powders, food products or tablets. Avalanches of snow (Hopfinger 1983), motion of ice sheets (Longwell et al. 1948), slides of rock debris (Hsu 1975), and submarine debris flows (Middleton and Hampton 1976) are some examples in the geophysical field. In the chemical industry more than 30% of products are formed as particles (Shamlou 1988). Examples of related heat and mass transfer problems include the handling and conveying of frozen foods prior to packaging, the drying, heating or cooling of grains, the calcination of limestone, and the gasification of solid waste in moving beds and rotary kilns (Kunii 1980; Richard and Raghavan 1984; Ferron and Singh 1991). An important aspect in many of these applications is the degree of mixing that occurs in the handling of the materials (Clump 1967). Most modeling efforts

rely on empirical information that is difficult to apply to a range of material flow rates and different types of material (Stephens and Bridgwater 1978; Bridgwater et al. 1985). In order to efficiently handle the transport processes in industrial fields, an understanding of the rheological behavior of granular material flows is important.

1.1 Research Developments for Granular Material Flows

Bagnold is the pioneer of the field of granular flows. Three regimes of granular flow behavior were classified by Bagnold (1954): the macroviscous, the transitional, and the grain-inertia. These three regimes were distinguished by a dimensionless parameter, the "Bagnold number" Ba,

$$Ba = \Lambda^{\frac{1}{2}} \rho_p \sigma^2 \Big(\frac{du_x}{dy}\Big) \Big/ \mu_f, \tag{1.1}$$

where Λ is a function of the solid fraction, ρ_p is the particle density, σ is the particle diameter, du_x/dy is the shear rate, and μ_f is the dynamic viscosity of the interstitial fluid. Like the Reynolds number, the Bagnold number denotes the ratio of the inertia force to the viscous force in the granular material flow. For $Ba < 40$, the flow is in the macroviscous regime where the viscosity of the interstitial fluid is dominant in the flow. For $Ba > 450$, the flow corresponds to the grain-inertia regime, where the interstitial fluid plays little role in the mechanics of the flow. Instead, the inter-particle collisions govern the flow behavior. The current study only addresses in this regime. The flows with a Bagnold number between the two limits are within the transitional regime, where both the interstitial fluid and the collisions between particles are important.

In the grain-inertia regime (rapid-flow regime), the particles are much denser than the interstitial fluid or are closely packed, so the interstitial fluid is neglected in the bulk flow behavior. The particle-to-particle collisions are dominant in the flows (Savage 1984; Campbell 1990), and result in a random motion of the particles. The similarity between the random motion of the particles in a granular flow and the motion of molecules in a gas drew recent researchers to use the term granular temperature to quantify the mean-square value of the fluctuating velocities (Ogawa 1978). Although the granular temperature plays a similar role as the thermal temperature in the gas kinetic theory, it does not have the dimension of temperature (K or °C) but has the dimension of specific energy (m^2/sec^2).

In the grain-inertia regime of granular flows, similar to dense gases, there are two important mechanisms that influence the transport properties: the streaming or kinetic mode, and the collisional mode (Campbell 1990). The streaming or kinetic mode accounts for the transfer of particle properties as the particles freely move between collisions. The collisional mode accounts for the transfer of the properties during collisions. The streaming mode is dominant for the dilute flows that have larger mean-free paths. The collisional mode is more important for the high-solid-fraction flows because of the higher collisional frequency.

In recent years the field of granular material flows has significantly progressed through the application of gas kinetic theory. Savage and Jeffrey (1981) employed the Maxwellian distribution function to model the random motion of the particles and assumed binary collisions between particles. They analyzed the stress tensor in a granular flow at high flow rates. They assumed the particles were perfectly elastic,

which was not true in all the applications.

Similar to Savage and Jeffrey (1981), Jenkins and Savage (1983) assumed the fluctuating velocity distribution function was Maxwellian and derived the conservation equations of mass, momentum and fluctuating energy for the rapid flow of identical, smooth, nearly elastic, spherical particles. The integral forms for the stress, fluctuating energy flux and energy dissipation were also derived. However, only the collisional contributions to the transfer of stress and fluctuating energy were considered in these two studies.

Based on Chapman-Enskog dense-gas kinetic theory (Chapman and Cowling 1970), Lun et al. (1984) derived the kinetic theory for a granular flow of nearly elastic particles. Not only the collisional contribution but also the kinetic mode were considered, so the theory is also applicable to a dilute system which is dominated by the kinetic mode. The importance of the research by Lun et al. (1984) is that the velocity distribution function was not assumed to be Maxwellian as the earlier studies. Since gradients in the velocity, the granular temperature and the number density exist in the granular flows, the system is not in an equilibrium state and the velocity distribution function should not be Maxwellian. Lun et al. successfully developed the first order correction term for the velocity distribution function and applied the theory to more general flow fields. However, in order to use the modified Maxwellian distribution function, the collisions were assumed to be isotropic. This assumption did not have to be made in the studies by Savage and Jeffrey (1981) and Jenkins and Savage (1983). The details of the dense-kinetic theory are discussed in Section 2.1. The governing equations, the stress tensor and the fluctuating energy

flux derived by Lun et al. (1984) are described in Sections 2.2 and 2.3.1.

Besides the inelasticity, many granular materials are not perfectly-frictionless and the rotational inertia of the particles should be included in the analysis. Jenkins and Richman (1985) employed the Grad's method of moments to derive the governing equations and the constitutive relations for plane flows of a dense gas of identical, rough, inelastic circular disks. Based on the theory derived by Jenkins and Savage (1983) and Lun et al. (1984), Lun and Savage (1987) extended the theory for granular flow of rough, inelastic spherical particles; however, only the collisional mode was considered in their analysis. Lun (1991) continued to work on the kinetic theory for slightly inelastic and slightly rough spheres by considering both the kinetic and the collisional modes. Because of the complexity of these theories and the number of parameters used, the calculations are too complicated to be applied to general flows.

The no-slip velocity conditions on the boundary are widely used in fluid mechanics. However, this is not true in a granular flow. In a granular flow, the boundary generates shear work and fluctuating energy. The energy is also dissipated due to inelastic collisions between the particles and the boundary. To solve the governing equations for a granular flow, the boundary conditions can be prescribed by specific values from experimental results (Ahn et al. 1992). Otherwise, the boundary conditions have to be found from their dependence on the whole flow field. Jenkins and Richman (1986) derived the boundary conditions for plane flows of smooth, nearly elastic, circular disks with a bumpy boundary. Based on the kinetic theory and assuming a Maxwellian distribution function for the fluctuating velocity, they balanced the transfer rates and dissipation rates of momentum and energy between the flows

and the boundary and finally they could express the boundary conditions implicitly. Richman (1988) improved Jenkins and Richman's (1986) theory by using a modified Maxwellian distribution function and derived the boundary conditions for the flow of smooth, nearly elastic spheres with a bumpy wall.

Johnson and Jackson (1987) derived the constitutive relations for granular materials including frictional effects. Different from Lun's (1991) analysis, in which the velocity distribution function was derived by considering the rotational inertia, Johnson and Jackson calculated the frictional contributions to the stress and the energy based on some empirical results. The kinetic and the collisional contributions were calculated from the results from Lun et al. (1984). The boundary conditions were also derived by balancing the momentum and the energy transfer similar to Richman's (1988) analysis. Frictional effects were also included in the derivation of the boundary condition. The theory was applied to plane shear flows in the same study. Johnson et al. (1990) continued to apply this theory to flows in the chutes in a later study. However, there are still several assumptions that remain questionable, e.g., the dependence of the frictional normal stress on the solid fraction, and the continuum assumption when the depth of the flow was only a few particle diameters.

There are relatively few experimental studies of granular flows. Measurements of velocity, granular temperature and solid fraction are the most difficult aspects of the experimental work. Some examples of experimental studies of granular material flows in shear cells are Savage and McKeown (1983), Savage and Sayed (1984), Hanes and Inman (1985), and Wang and Campbell (1992); that in the vertical channels are Takahashi and Yanai (1973), Savage (1979) and Nedderman and Laohakul (1980);

and that in the inclined chutes are Roberts (1969), Ridgway and Rupp (1970), Augenstein and Hogg (1974, 1978), Bailard (1978), Savage (1979), Ishida and Shirai (1979), Patton et al. (1987), Johnson et al. (1990) and Ahn et al. (1991). Most of these experiments measured the normal stresses, shear stresses, average solid fractions for certain regions, or mass flow rates. Using high-speed camera technology (Roberts 1969; Nedderman and Laohakul 1980) or the fibre optic probes (Savage 1979; Ishida and Shirai 1979; Johnson et al. 1990; Ahn et al. 1991) the point velocity profiles were also measured. The fluctuating velocities in the flow direction and the 1-D solid fractions were first successfully measured by Ahn et al. (1991) by using fibre optic probes. However, the granular temperature and the solid fraction still can not be measured directly, although Ahn et al. used the one-dimensional information to predict these values.

Due to the difficulty in the real measurements, computer simulation methods have become an important vehicle in understanding the rheology of the granular material flows. By putting a number of imaginary particles (or disks) in a control volume bounded by periodic boundaries and giving them initial translational velocities and angular rotational velocities which are randomly distributed about the flow field, the particles start to collide with each other and finally reach a steady state. The interactions between particles only occur at particle-particle contact points. Only binary collisions are considered and the interstitial fluid effects are neglected. Some examples are Walton (1984), Campbell and Brennen (1985a,b), Campbell and Gong (1986, 1987), Walton (1986), Walton and Braun (1986a,b), Campbell (1988,1989), Walton et al. (1988), Louge et al. (1990), Kim and Rosato (1992) and Walton (1992).

Through computer simulations, statistical calculations of the velocities, granular temperatures and solid fractions become possible. The computer simulation results of Campbell and Brennen (1985b) indicated that the velocity distribution functions are close to Maxwellian. The results also indicated that the granular temperatures are not perfectly-isotropic; however, the isotropy of the granular temperature is a general assumption in the kinetic theory. The technology of computer simulation was also extended to calculate the self-diffusion coefficients (Savage 1992).

Heat transfer problems are important in industry, especially for the drying, heating or cooling of grains. Most of the heat transfer studies discuss convection and have many similarities to convection in fluidized beds. Sullivan and Sabersky (1975) investigated the convective heat transfer from a flat plate which was immersed in a flow of granular medium. The convective heat transfer to the granular flow in an inclined chute was also studied by Patton et al. (1986) and Ahn (1989). These three studies included experimental and analytical works; however, the theories did not include the effects of particle mixing, and the kinetic theory was not employed.

By mean-free-path argument and assuming that the fluctuating velocity distribution was Maxwellian, Hunt and Hsiau (1990) developed a theory for the effective thermal conductivity of low-density granular flows. Wang and Campbell (1992) performed a heat transfer experiment in an annular shear cell. By measuring the temperatures and the heat flux, the effective thermal conductivity was determined.

1.2 Topics of the Present Research

Most of the developments about dense-gas kinetic theory are described in Chapter 2. Sections 2.1 and 2.2 describe the background of the kinetic theory and the governing equations for flows of granular materials. The results of the stress tensor and the fluctuating flux derived by Lun et al (1984) are given in Section 2.3.1. In Sections 2.3.2 and 2.3.3, the analytical relations for the flow-induced particle diffusivity and the thermal conductivity are derived based on the kinetic theory of dense gases. The particle diffusivity and the effective thermal conductivity are found to increase with the square-root of the granular temperature. Section 2.4 describes the kinetic theory for a binary-mixture of granular materials which were derived by López de Haro et al (1983) and Jenkins and Mancini (1989) by employing the revised Enskog theory.

Chapter 3 describes the experimental study of granular flows in a vertical channel. The first part of the experiment concerns the measurement of the local velocity and the fluctuating velocity in the flow direction. These quantities were measured using fibre optic probe technology. The second part is a particle diffusion experiment which was conducted in the same vertical channel. Two differently-colored and otherwise-identical particle streams were mixed in the channel. A frame grabber and an image processing system were employed to measure the mixing layer thickness. Section 3.1 describes the experimental apparatus and the procedures; the data are presented in Section 3.2.

In Chapter 4 the theoretical results from Section 2.3 are used to predict the experimental results. By solving the momentum and the fluctuating energy equations,

the velocity and the granular temperature profiles are obtained. The results and the comparison with the experimental velocity profiles are shown in Section 4.1. The expression of the self-diffusion coefficient derived in Section 2.3.2 is used to calculate the mixing layer thickness profiles in the vertical channel. Section 4.2 shows the comparison with the experimental results described in Chapter 3. In Section 4.3, the expression for the effective thermal conductivity is compared with Wang and Campbell's (1992) experimental results.

Chapter 5 presents the study of granular thermal diffusion in a binary mixture. Due to the granular temperature gradient, the phenomenon called granular thermal diffusion occurs. This issue has not been previously discussed in the research field of granular flows. By using the theory derived by Jenkins and Mancini (1989) which is introduced in Section 2.4, the granular thermal diffusion process is studied. The theory is applied to calculate granular thermal diffusion in an oscillatory system, a sheared flow and a flow in a vertical channel.

Chapter 2

Dense-Gas Kinetic Theory

2.1 Background

The interactions between particles are the most important mechanisms in the grain-inertia regime of granular flows. Similar to a molecular gas, the collisions result in a random motion of the particles. In recent years, researchers (Savage 1984; Campbell 1990) have started to employ the dense-gas kinetic theory to develop the governing equations and the constitutive relations for granular flows. Different from the perfectly elastic molecules in gases, the particles in granular flows are not elastic and energy is dissipated due to the inelastic collisions. Hence, the particle motion is not self-sustaining and the energy should be generated by the shearing of the flows or by the vibration of the boundaries.

The modeling of the random motion of the particles is an important aspect in analyzing granular flows. Employing the dense-gas kinetic theory, the fluctuating

velocities of the particles are assumed to follow the singlet velocity distribution, $f^{(1)}(\mathbf{r}, \mathbf{c}; t)$. Since the particle motion is not self-sustaining, the velocity distribution function is not Maxwellian. In this case, the singlet velocity distribution function $f^{(1)}(\mathbf{r}, \mathbf{c}; t)$ is assumed to be

$$f^{(1)}(\mathbf{r}, \mathbf{c}; t) = f^{(0)}(\mathbf{r}, \mathbf{c}; t)(1 + \Phi), \tag{2.1}$$

where $\mathbf{c}$ is the particle's local velocity, $\mathbf{r}$ is the particle location, t is the time, Φ is a perturbation term where $\Phi \ll 1$, and $f^{(0)}(\mathbf{r}, \mathbf{c}; t)$ is the well-known Maxwellian distribution function:

$$f^{(0)}(\mathbf{r}, \mathbf{c}; t) = \frac{n}{(2\pi\Upsilon)^{\frac{3}{2}}} \exp\left(-\frac{C^2}{2\Upsilon}\right). \tag{2.2}$$

In the Maxwellian distribution function, n is the number density, C is the magnitude of the fluctuating velocity $\mathbf{C}$, and Υ is the granular temperature. The fluctuating velocity $\mathbf{C}$ is the local velocity deviation from the mean velocity $\mathbf{u}$, $\mathbf{u} = < \mathbf{c} >$, $\mathbf{C} = \mathbf{c} - \mathbf{u}$. Analogous to the thermal temperature in the gases, the granular temperature quantifies the specific kinetic energy of the particles and is defined by $\Upsilon = < C^2 > /3$. The symbol $< >$ represents the ensemble-average quantity. The ensemble-average of the local property, Ψ, is determined by averaging the single-particle properties over the entire velocity space:

$$< \Psi > = \frac{1}{n} \int \Psi f^{(1)}(\mathbf{r}, \mathbf{c}; t) d\mathbf{c}, \tag{2.3}$$

where the product $f^{(1)}(\mathbf{r}, \mathbf{c}; t)d\mathbf{c}$ represents the probable number of particles per unit volume with local velocities within the velocity element $d\mathbf{c}$ centered at $\mathbf{c}$ and $d\mathbf{c} = dc_x dc_y dc_z$. In Equation (2.3), Ψ denotes the local particle properties, such as

mass, momentum, or energy. Due to the random movements of the particles, these properties may vary from the ensemble-average value.

Except for the sections on binary mixtures, the present work assumes all the particles are identical, spherical, smooth and nearly elastic. The collisions are instantaneous and only binary collisions are considered. To analyze a binary collision, the pair-distribution function $f^{(2)}(\mathbf{r}-\frac{1}{2}\sigma\mathbf{k},\mathbf{c}_1,\mathbf{r}+\frac{1}{2}\sigma\mathbf{k},\mathbf{c}_2;t)$ is used instead of the single-particle velocity distribution function (Chapman and Cowling 1970; Lun et al. 1984), where the subscripts 1 and 2 represent two different particles, σ denotes the particle diameter and $\mathbf{k}$ is the unit vector directed from the center of particle 1 to particle 2, as shown in Figure 2.1. Using the Enskog assumption for dense gases, Lun et al. (1984) defined the pair-distribution function from the product of the single-particle velocity distribution functions for particles 1 and 2, and a correction factor $g_0(\nu)$,

$$f^{(2)}(\mathbf{r}-\frac{1}{2}\sigma\mathbf{k},\mathbf{c}_1,\mathbf{r}+\frac{1}{2}\sigma\mathbf{k},\mathbf{c}_2;t)=g_0(\nu)f^{(1)}(\mathbf{r}-\frac{1}{2}\sigma\mathbf{k},\mathbf{c}_1;t)f^{(1)}(\mathbf{r}+\frac{1}{2}\sigma\mathbf{k},\mathbf{c}_2;t). \quad (2.4)$$

The correction factor $g_0(\nu)$ in Equation (2.4) is referred to as the radial distribution function evaluated when the particles are in contact and ν is the solid fraction. The radial distribution function equals unity for low-density flows and approaches infinity as the flow approaches a packed, rigid state. An empirical form of this radial distribution function was given by Carnahan and Starling (1969) as follows :

$$g_0(\nu)=(2-\nu)/[2(1-\nu)^3]. \quad (2.5)$$

This expression becomes poor when solid fraction is higher than 0.5. For sheared

granular flows, the work by Lun and Savage (1986) suggests the following form :

$$g_0(\nu) = (1 - \nu/\nu^*)^{-2.5\nu^*}, \tag{2.6}$$

where ν^* is the maximum shearable solid fraction for spherical particles. This expression is more appropriate for the high-solid-fraction flows. The radial distribution functions as given by Equations (2.5) or (2.6) assume an isotropic distribution of collision angles between the two colliding spheres. The expression in Equation (2.6) is used in the present study.

Therefore, the number of pairs of particles 1 and 2 that are in contact that have impact velocities within the range $\mathbf{c}_1$ to $\mathbf{c}_1 + d\mathbf{c}_1$ and $\mathbf{c}_2$ to $\mathbf{c}_2 + d\mathbf{c}_2$ could be expressed as

$$f^{(2)}(\mathbf{r} - \frac{1}{2}\sigma\mathbf{k}, \mathbf{c}_1, \mathbf{r} + \frac{1}{2}\sigma\mathbf{k}, \mathbf{c}_2; t)\sigma^2(\mathbf{c}_{12} \cdot \mathbf{k})d\mathbf{k}d\mathbf{c}_1 d\mathbf{c}_2,$$

where $\mathbf{c}_{12}$ is the relative velocity of the two impacting particles, $\mathbf{c}_{12} = \mathbf{c}_1 - \mathbf{c}_2$.

2.2 Governing Equations

Lun et al. (1984) modified the equation for the rate of change of $< n\Psi >$ given by Reif (1965) as

$$\frac{\partial}{\partial t} < n\Psi >= n < \mathbf{F} \cdot \frac{\partial \Psi}{\partial \mathbf{c}} > -\nabla \cdot < n\mathbf{c}\Psi > -\nabla \cdot \mathbf{\Theta}(\Psi) + \chi(\Psi), \tag{2.7}$$

where $\mathbf{F}$ is the specific external force of the particles. The first term on the right hand side of Equation (2.7) is the time rate of change of $< n\Psi >$ that results from the variation in the local velocity $\mathbf{c}$ due to the external force field. The second term

is the "convection" term which represents the rate of change of $< n\Psi >$ due to the net influx to the volume of the flow. The last two terms account for the change rate of $< n\Psi >$ per unit volume due to the inter-particle collisions. The collisional contribution was derived by Lun et al. (1984) and decomposed into two parts: one is the collisional "source-like" contribution χ,

$$\begin{aligned}\chi(\Psi) &= \frac{\sigma^2}{2}\int_{\mathbf{c}_{12}\cdot\mathbf{k}>0}(\Psi_2' + \Psi_1' - \Psi_2 - \Psi_1)(\mathbf{c}_{12}\cdot\mathbf{k}) \\ &\times \quad f^{(2)}(\mathbf{r} - \tfrac{1}{2}\sigma\mathbf{k}, \mathbf{c}_1, \mathbf{r} + \tfrac{1}{2}\sigma\mathbf{k}, \mathbf{c}_2; t)\; d\mathbf{k}d\mathbf{c}_1 d\mathbf{c}_2, \end{aligned} \tag{2.8}$$

and the other is the collisional flux $\mathbf{\Theta}$,

$$\begin{aligned}\mathbf{\Theta}(\Psi) &= -\frac{\sigma^3}{2}\int_{\mathbf{c}_{12}\cdot\mathbf{k}>0}(\Psi_1' - \Psi_1)(\mathbf{c}_{12}\cdot\mathbf{k})\mathbf{k} \\ &\times \quad f^{(2)}(\mathbf{r} - \tfrac{1}{2}\sigma\mathbf{k}, \mathbf{c}_1, \mathbf{r} + \tfrac{1}{2}\sigma\mathbf{k}, \mathbf{c}_2; t)\; d\mathbf{k}d\mathbf{c}_1 d\mathbf{c}_2, \end{aligned} \tag{2.9}$$

where $'$ denotes the properties after the collision.

By substituting $\Psi = m$, $m\mathbf{c}$ or $mc^2/2$ into Equation (2.7) respectively, the conservation equations of mass, momentum and fluctuating energy are obtained:

$$\frac{d\rho}{dt} = -\rho\nabla\cdot\mathbf{u}, \tag{2.10}$$

$$\rho\frac{d\mathbf{u}}{dt} = \rho\mathbf{F} - \nabla\cdot\mathbf{P}, \tag{2.11}$$

$$\frac{3}{2}\rho\frac{d\Upsilon}{dt} = -\mathbf{P}:\nabla\mathbf{u} - \nabla\cdot\mathbf{\Gamma} - \gamma, \tag{2.12}$$

where ρ is the bulk flow density, and is determined from the product of the particle mass, m, and the number density, $\rho = mn$, or from the product of the particle density, ρ_p, and the solid fraction, $\rho = \rho_p\nu$. In Equation (2.11), $\mathbf{P}$ is the pressure

tensor contributed from the streaming mode $\mathbf{P}_k$ and the collisional mode $\mathbf{P}_c$, as mentioned in the Section 1.1:

$$\mathbf{P} = \mathbf{P}_k + \mathbf{P}_c, \tag{2.13}$$

where

$$\mathbf{P}_k = \rho < \mathbf{CC} >, \tag{2.14}$$

$$\mathbf{P}_c = \mathbf{\Theta}(m\mathbf{C}). \tag{2.15}$$

Similar to the pressure tensor, the fluctuating energy flux denoted by $\mathbf{\Gamma}$ is also composed of the streaming mode $\mathbf{\Gamma}_k$ and the collisional mode $\mathbf{\Gamma}_c$:

$$\mathbf{\Gamma} = \mathbf{\Gamma}_k + \mathbf{\Gamma}_c, \tag{2.16}$$

where

$$\mathbf{\Gamma}_k = \frac{1}{2}\rho < C^2\mathbf{C} >, \tag{2.17}$$

$$\mathbf{\Gamma}_c = \mathbf{\Theta}(\frac{1}{2}mC^2). \tag{2.18}$$

The last term in Equation (2.12) γ represents the energy dissipated per unit volume due to the collisions and is expressed as:

$$\gamma = -\chi(\frac{1}{2}mC^2). \tag{2.19}$$

Note that when $\Psi = m\mathbf{C}$ substituted into Equation (2.8), $\chi(m\mathbf{c})$ is zero since $m\mathbf{c}$ is a summational invariant.

2.3 Transport Phenomena in a Single Species Granular Flow

2.3.1 Stress Tensor and Fluctuating Energy Flux

The key point in developing the transport equations for a non-uniform gas or a granular flow is to obtain the perturbation term of the singlet velocity distribution function, Φ. Using the Enskog theory, Chapman and Cowling (1970) assumed that the perturbation term is linearly dependent on the gradients of the pressure, the (granular) temperature, the flow velocity, and the diffusion force vector resulting from the deviation between the non-uniform flow and the uniform system. The diffusion force vector vanishes when the particles are identical. The details of the diffusion force vector are given in Section 2.4. Chapman and Cowling expressed the coefficients of the gradients in terms of Sonine polynomials. By keeping the first term in the expansions and they successfully derived the constitutive relations of the elastic dense gases. For flows of slightly inelastic particles, Lun et al. (1984) used a different approach and assumed a trial function as the perturbation function that satisfied the different moment equations generated by Equation (2.7). The perturbation function was then derived:

$$\Phi = a_1(\mathbf{CC} - \frac{1}{3}C^2\mathbf{I}) : \nabla\mathbf{u} + a_2\left(\frac{5}{2} - \frac{C^2}{2\Upsilon}\right)\mathbf{C}\cdot\nabla\ln\Upsilon + a_3\left(\frac{5}{2} - \frac{C^2}{2\Upsilon}\right)\mathbf{C}\cdot\nabla\ln n, \quad (2.20)$$

where

$$a_1 = -\frac{\mu}{\eta(2-\eta)\rho\Upsilon^2 g_0}\left[1 + \frac{8}{5}\eta(3\eta-2)\nu g_0\right], \quad (2.21)$$

$$a_2 = \frac{16\lambda}{5\eta(41-33\eta)\rho\Upsilon g_0}\left[1 + \frac{12\eta^2}{5}(4\eta-3)\nu g_0\right], \quad (2.22)$$

$$a_3 = \frac{192\lambda}{25(41-33\eta)\rho\Upsilon g_0}(2\eta-1)(\eta-1)\frac{d}{d\nu}(\nu^2 g_0), \tag{2.23}$$

and

$$\eta = \frac{1}{2}(1+e_p), \quad \mu = \frac{5m(\Upsilon/\pi)^{\frac{1}{2}}}{16\sigma^2}, \quad \lambda = \frac{75m(\Upsilon/\pi)^{\frac{1}{2}}}{64\sigma^2}.$$

Note that the restitution coefficient of the particles is denoted by e_p and $\mathbf{I}$ is the identity matrix. For the elastic particles, $e_p = 1$ and $\eta = 1$, and the perturbation function derived by Lun et al. is the same as the first approximation derived by Chapman and Cowling (1970).

Using Equation (2.20) in Equations (2.13)–(2.19), Lun et al. (1984) derived the stress tensor, the fluctuating energy flux and the energy dissipation as follows:

$$\mathbf{P} = \left[\rho_p g_1(\nu,e_p)\Upsilon - \rho_p\sigma\frac{8}{3\sqrt{\pi}}\eta\nu^2 g_0\Upsilon^{\frac{1}{2}}\nabla\cdot\mathbf{u}\right]\mathbf{I} - 2\rho_p\sigma g_2(\nu,e_p)\Upsilon^{\frac{1}{2}}\mathbf{S}, \tag{2.24}$$

$$\mathbf{\Gamma} = -\rho_p\sigma\left[g_3(\nu,e_p)\Upsilon^{\frac{1}{2}}\nabla\Upsilon + g_4(\nu,e_p)\Upsilon^{\frac{3}{2}}\nabla\nu\right], \tag{2.25}$$

$$\gamma = \frac{\rho_p}{\sigma}g_5(\nu,e_p)\Upsilon^{\frac{3}{2}}, \tag{2.26}$$

where

$$\mathbf{S} = \frac{1}{2}(u_{n,p}+u_{p,n}) - \frac{1}{3}u_{l,l}\delta_{np}, \qquad l,n,p = x,y,z \tag{2.27}$$

and the coefficients $g_1(\nu,e_p)$, $g_2(\nu,e_p)$, $g_3(\nu,e_p)$, $g_4(\nu,e_p)$ and $g_5(\nu,e_p)$ depend on ν and e_p and are expressed as follows:

$$g_1(\nu,e_p) = \nu + 4\eta\nu^2 g_0, \tag{2.28}$$

$$g_2(\nu,e_p) = \frac{5\sqrt{\pi}}{96}\left\{\frac{1}{\eta(2-\eta)g_0} + \frac{8}{5}\frac{3\eta-1}{2-\eta}\nu + \frac{64}{25}\eta\left(\frac{3\eta-2}{2-\eta}+\frac{12}{\pi}\right)\nu^2 g_0\right\}, \tag{2.29}$$

To determine the diffusive flux of particles 1 into particles 2, assume that transport by diffusion only occurs in the y-direction as shown in Figure 2.2. Then the determination of the mass flux is similar to the method used to determine the streaming contributions to the stress tensor and the kinetic-energy flux vector. The mass fluxes of the two groups of particles are

$$\frac{\dot{m}_1}{m} = \Sigma C_{1y} = \int C_{1y}\ f_1^{(1)}(\mathbf{r}_1, \mathbf{c}_1; t)\ d\mathbf{c}_1 = -D_{12}\frac{dn_1}{dy}, \tag{2.34}$$

$$\frac{\dot{m}_2}{m} = \Sigma C_{2y} = \int C_{2y}\ f_2^{(1)}(\mathbf{r}_2, \mathbf{c}_2; t)\ d\mathbf{c}_2 = -D_{21}\frac{dn_2}{dy}, \tag{2.35}$$

where ΣC_y symbolizes the y-direction fluctuating velocity integrated over the whole velocity space. Fick's law is used in Equations (2.34) and (2.35) to define the diffusion coefficients, D_{12} and D_{21}. If the velocity distribution function is Maxwellian ($\Phi = 0$), then the diffusive fluxes $\dot{m}_1$ and $\dot{m}_2$ are zero. Because of the concentration gradient, however, the flow is not in equilibrium and the perturbation term Φ should be included. Lun et al.'s singlet velocity distribution function cannot be used to derive the diffusion velocity since their perturbation function was developed for a single species. Instead the method by Kennard (1938) is used in which a correction term is added to the Maxwellian distribution function to represent the singlet velocity distribution function:

$$f_i^{(1)}(\mathbf{r}_i, \mathbf{c}_i; t) \ = \ f_i^{(0)}(\mathbf{r}_i, \mathbf{c}_i; t) \ + \ f_i^{(c)}(\mathbf{r}_i, \mathbf{c}_i; t)\ , \quad i = 1 \text{ or } 2. \tag{2.36}$$

Using this representation yields a non-zero diffusive flux. It should be noted that $f^{(c)}$ has the similar form as $\Phi f^{(0)}$, and $f^{(c)} \ll f^{(0)}$. A similar technique is applied here to derive the self-diffusion coefficient for granular material flows.

In kinetic theory, the Boltzmann equation is used to describe the rate of change in the velocity distribution function that results from particle collisions (Chapman and Cowling 1970). Similarly for granular-material flows, the Boltzmann equation could be used to determine the distribution functions $f_1^{(1)}$ and $f_2^{(1)}$. Assuming there are no external forces applied to the particles, the Boltzmann equation is

$$\frac{\partial f_i^{(1)}}{\partial t} + \mathbf{C}_i \cdot \nabla f_i^{(1)} = \left[\frac{\partial f_i^{(1)}}{\partial t}\right]_{coll}, \quad i = 1 \text{ or } 2 , \tag{2.37}$$

where the right-hand side represents the change of velocity distribution function due to the collisions. For steady-state conditions and assuming only variations in the y-direction, Equation (2.37) becomes

$$C_{iy}\frac{\partial f_i^{(1)}}{\partial y} = \left[\frac{\partial f_i^{(1)}}{\partial t}\right]_{coll}, \quad i = 1 \text{ or } 2 . \tag{2.38}$$

The general form for the distribution function, Equation (2.36), is substituted into Equation (2.38), and the derivative of the correction term is neglected since $f^{(c)} \ll f^{(0)}$. By noting that the collisions do not alter the Maxwellian distribution function, and assuming that Υ_1 is independent of y within the local region of interest, Equation (2.38) becomes

$$C_{iy}\frac{\partial f_i^{(0)}}{\partial y} = \frac{C_{iy}}{(2\pi\Upsilon_i)^{\frac{3}{2}}}\exp(-\frac{C_i^2}{2\Upsilon_i})\frac{dn_i}{dy} = \left[\frac{\partial f_i^{(c)}}{\partial t}\right]_{coll}, \quad i = 1 \text{ or } 2 , \tag{2.39}$$

As described by Kennard (1938), one method of solving Equation (2.39) is to substitute for the right-hand side an integral expression for the rate of change of the distribution function. The distribution function is then found by solving the integro-differential equation. A simpler method, referred to as the Maxwell-Chapman method as outlined by Kennard (1938), involves substituting an assumed form for

$f_1^{(c)}$. Following the arguments by Kennard, the form of Equation (2.39) suggests representations for the correction terms:

$$f_1^{(c)} = A_1 C_{1y} \exp(-\frac{C_1^2}{2\Upsilon_1}), \tag{2.40}$$

$$f_2^{(c)} = A_2 C_{2y} \exp(-\frac{C_2^2}{2\Upsilon_2}), \tag{2.41}$$

where A_1 and A_2 are coefficients that need to be determined. Since the particles are identical, the granular temperatures are equal, $\Upsilon_1 = \Upsilon_2 = \Upsilon$. Using Equation (2.40) and re-evaluating Equation (2.34) yields:

$$\frac{\dot{m}_1}{m} = \Sigma C_{1y} = A_1 \Upsilon^{\frac{5}{2}} (2\pi)^{\frac{3}{2}} = -D_{12} \frac{dn_1}{dy}. \tag{2.42}$$

A similar expression is obtained for $\dot{m}_2$. For a flow without a net mass flux, $\dot{m}_2$ is equal to $-\dot{m}_1$, and as a result A_2 must be equal to $-A_1$.

To find A_1 it is necessary to examine the rate of change of ΣC_{1y} by collisions. This quantity is determined by multiplying the Boltzmann equation by C_{1y} and integrating over the velocity space. From Equation (2.39) and using $D\Sigma C_{1y}$ to represent the rate of change of ΣC_{1y},

$$D\Sigma C_{1y} = \int C_{1y} \Big[\frac{\partial f_1^{(c)}}{\partial t}\Big]_{coll} d\mathbf{c}_1 = \Upsilon \frac{dn_1}{dy}. \tag{2.43}$$

The first step to determine $D\Sigma C_{1y}$ is to examine the effect of each collision on the velocity C_{1y}. To proceed, consider a collision between an incoming particle 1 and a scattering particle 2; the particles are of equal mass, smooth and slightly inelastic. By the conservation of linear momentum, the change in y-velocity of particle 1 is

$$C'_{1y} - C_{1y} = -C_{12,y}(1 + e_p)(1 - \cos\theta)/4, \tag{2.44}$$

where $'$ indicates the velocity after collision, $\mathbf{C}_{12}$ is the relative fluctuating velocity vector $\mathbf{C}_{12} = \mathbf{C}_1 - \mathbf{C}_2$, e_p is the coefficient of restitution between the inelastic particles, and θ is the angle through which $\mathbf{C}_{12}$ is turned during the collision. The next step is to consider all possible collisions between the scattering particle 2 and incoming particles 1. Using the scattering coefficient of $\sigma^2/4$, the fraction of incoming particles 1 per unit area scattered into the angle from θ to $\theta + d\theta$ is $2\pi(\sigma^2/4)\sin\theta d\theta$. The number of encounters between the pairs of particles 1 and 2 that result in the movement of particle 1 into an angle $d\theta$ centered at θ is found from the product of the scattering coefficient, $2\pi(\sigma^2/4)\sin\theta d\theta$, the relative velocity, C_{12}, and the pair-distribution function, $f^{(2)}(\mathbf{r} - \frac{1}{2}\sigma\mathbf{k}, \mathbf{c}_1, \mathbf{r} + \frac{1}{2}\sigma\mathbf{k}, \mathbf{c}_2; t)\ d\mathbf{c}_1 d\mathbf{c}_2$. Therefore, the total change in ΣC_{1y} is found by integrating over all possible angles $d\theta$ and over the velocity spaces $d\mathbf{c}_1$ and $d\mathbf{c}_2$,

$$\begin{aligned} D\Sigma C_{1y} &= \int_{-\infty}^{\infty}\int_{-\infty}^{\infty}\int_{0}^{\pi}(2\pi\frac{\sigma^2}{4}\sin\theta)C_{12}(C'_{1y} - C_{1y}) \\ &\times \quad f^{(2)}(\mathbf{r} - \tfrac{1}{2}\sigma\mathbf{k}, \mathbf{c}_1, \mathbf{r} + \tfrac{1}{2}\sigma\mathbf{k}, \mathbf{c}_2; t)\ d\theta d\mathbf{c}_1 d\mathbf{c}_2. \end{aligned} \tag{2.45}$$

Equation (2.45) is evaluated by substituting in Equations (2.2), (2.4), (2.36), (2.40), (2.41) and (2.44) and neglecting the second order terms, $f_1^{(c)} f_2^{(c)}$ and the terms involving the space derivative of the velocity distribution functions. The integral becomes

$$D\Sigma C_{1y} = -(A_1 n_2 - A_2 n_1)\frac{8\sqrt{2}}{3}\pi^2\sigma^2 g_0(\nu)(1 + e_p)\Upsilon^3. \tag{2.46}$$

By combining Equations (2.42), (2.43) and (2.46) with $A_2 = -A_1$ and $n = n_1 + n_2$, the self-diffusion coefficient is

$$D_{11} = \frac{\sigma\sqrt{\pi\Upsilon}}{8(1 + e_p)\nu g_0(\nu)}. \tag{2.47}$$

The same result is also derived using a momentum transfer method as outlined by Present (1958). The following is a brief outline of this method. Present used a modified Maxwellian velocity distribution function:

$$f^{(1)}(\mathbf{r},\mathbf{c};t) = \frac{n}{(2\pi\Upsilon)^{\frac{3}{2}}}\exp\Big[-\frac{C_x^2+(C_y-v_y)^2+C_z^2}{2\Upsilon}\Big], \tag{2.48}$$

where v_y is the diffusion velocity and $v_y \ll C_y$. Equation (2.48) is linearized which yields

$$f^{(1)}(\mathbf{r},\mathbf{c};t) = \frac{n}{(2\pi\Upsilon)^{\frac{3}{2}}}\exp(-\frac{C^2}{2\Upsilon})(1+\frac{v_y}{\Upsilon}C_y). \tag{2.49}$$

This distribution function has a similar correction form to the distribution function in Equations (2.40) and (2.41).

Let Ξ_{12} denote the average momentum transfer resulting from collisions between group 1 and group 2 per unit volume per unit time. For slightly-inelastic particles of uniform mass, using the conservation of linear momentum Ξ_{12} in y-direction is

$$\Xi_{12,y} = \frac{4}{3}(1+e_p)\sigma^2\sqrt{\pi\Upsilon}mg_0(\nu)n_1n_2(v_{1y}-v_{2y}). \tag{2.50}$$

From Equation (2.14), the kinetic normal stress in y-direction is

$$P_{1k,yy} = \rho_1 < C_{1y}C_{1y} >= mn_1\Upsilon. \tag{2.51}$$

If the granular temperature is constant in a small local region dy, then the net force acting on group 1 particles is $dP_{1k,yy} = m\Upsilon dn_1$ which is equivalent to $-dP_{2k,yy}$. By the conservation of momentum,

$$dP_{1k,yy} = -\Xi_{12,y}dy. \tag{2.52}$$

Using the fact that the total mass flux is zero, $n_1 v_{1y} = -n_2 v_{2y}$ and $n_1 + n_2 = n$, the self-diffusion coefficient is derived which results in the same relation as given by Equation (2.47).

Savage (1992) applied the Einstein relation (McQuarrie 1976) which relates the self-diffusion coefficient to the velocity autocorrelation function:

$$D_{11} = \frac{1}{3}\int_0^\infty < \mathbf{C}(0)\cdot\mathbf{C}(\tau) > d\tau, \tag{2.53}$$

where τ is a time variable. Savage followed kinetic-theory arguments and assumed that

$$< \mathbf{C}(0)\cdot\mathbf{C}(\tau) >=< C^2 > \exp(-\kappa t), \tag{2.54}$$

where κ^{-1}, a relaxation time, is influenced by the average momentum change due to collisions (McQuarrie 1976). When Equation (2.53) is evaluated, the resulting expression for the diffusion coefficient is the same as Equation (2.47).

Equation (2.47) indicates that the diffusion coefficient increases with square root of the granular temperature. For the elastic particles, $e_p = 1$, the self-diffusion coefficient in Equation (2.47) becomes the same as derived by Throne (Chapman and Cowling 1970).

2.3.3 Effective Thermal Conductivity

Different from gases, in granular flows, the heat is transferred due to the movements and the mixing of the particles. Hunt and Hsiau (1990) used mean-free-path arguments to develop analytical expressions for the effective thermal conductivity for low-density granular flows. They assumed constant properties and determined ex-

pressions for the effective thermal conductivity by integrating over the entire flow field. Instead of considering the entire flow with constant properties, a small local region is considered here and properties are assumed constant in this small region. The effective thermal conductivity due to the motion of the particles is developed from dense-gas kinetic theory. Since the heat capacity of the fluid is much smaller than that of the particles, the heat transfer due to the movement of the fluid is neglected. Sun and Chen (1988) verified that conduction between particles during collisions is negligible because of the short duration of the collision time and the small contact area. Therefore, only the heat transfer due to the streaming mode is considered for the heat transfer study and the heat flux could be determined from

$$\mathbf{q} = n < \Delta e \mathbf{C} >, \tag{2.55}$$

where Δe is the excess energy carried by a particle in the flows and is evaluated as follows. Note that the thermal radiation is neglected in the present analysis.

Consider a particle of thermal conductivity, k_p, heat capacity, c_p, total surface area, A, characteristic length, l_p, and a heat transfer coefficient between the particle and the fluid, h. The temperature gradient only exists in y-direction as shown in Figure 2.3. For Biot number, $Bi = hl_p/k_p$, less than 0.1, the lumped system analysis is applied and the energy equation becomes

$$mc_p \frac{dT}{dt} = hA(T_f - T), \tag{2.56}$$

where t is time variable, T is particle temperature and T_f is the local temperature of the surrounding fluid. As shown in Figure 2.3, consider a particle initially at the fluid temperate T_f that moves a short distance l to a new position with fluid temperature

$T_f' = T_f + l_y(dT/dy)$, where l_y is the y-component of l. Then at the new position, Equation (2.56) becomes

$$\zeta \frac{dT}{dt} = T_f + l_y \frac{dT}{dy} - T, \tag{2.57}$$

where $\zeta = mc_p/hA$. Suppose that the particle moves a distance l within a time τ to the position with surrounding fluid temperature of $T_f' = T_0 = T_f + l_y(dT/dy)$. Assume C_y is constant in this small local region, then the time and distance are related by $\tau = l/C = l_y/C_y$. Therefore Equation (2.57) could be solved:

$$T - T_0 + l_y \frac{dT}{dy} = tC_y \frac{dT}{dy} - \zeta C_y \frac{dT}{dy} + C_3 \exp(-t/\zeta), \tag{2.58}$$

where C_3 is a constant to be determined. By using the initial condition that the particle temperature equals the surrounding fluid temperature before the movement, i.e., $T = T_f = T_0 - l_y(dT/dy)$, the coefficient C_3 is found to be $\zeta C_y(dT/dy)$. Hence the particle temperature when $t = \tau = l_y/C_y$ is obtained:

$$T = T_0 - C_y \zeta \frac{dT}{dy}[1 - \exp(-l_y/\zeta C_y)]. \tag{2.59}$$

The group $l_y/\zeta C_y = \tau hA/mc_p$ is the product of the Biot number and the Fourier number, where the Fourier number is $Fo = k_p \tau A/l_p mc_p$. When the particle Biot-Fourier number is small, $BiFo \ll 1$, Equation (2.59) reduces to

$$T - T_0 = -l_y \frac{dT}{dy}, \tag{2.60}$$

The excess energy carried by the particle to this position relative to the surrounding fluid is $\Delta e = -mc_p l_y(dT/dy)$. The length l_y is found from the mean free path, λ_l, and the angle ξ between $\mathbf{C}$ and y-axis, $l_y = \lambda_l \cos\xi$. Therefore,

$$\Delta e = -mc_p \lambda_l \cos\xi \frac{dT}{dy}. \tag{2.61}$$

Similar to the streaming transport relations, the heat flux in the y-direction is found by integrating the product of C_y and the excess energy carried by particles over the entire velocity space:

$$q_y = n < \Delta e C_y >= \int \Delta e C_y \; f^{(1)}(\mathbf{r}, \mathbf{c}; t) \; d\mathbf{c}. \tag{2.62}$$

By substituting Equations (2.1) or (2.36) and (2.61) into Equation (2.62) and noting that the product of $\Delta e C_y$ and the correction term of velocity distribution function is an odd function, Equation (2.62) becomes

$$q_y = -\frac{2\sqrt{2}}{3\sqrt{\pi}} mnc_p \lambda_l \Upsilon^{\frac{1}{2}} \frac{dT}{dy}. \tag{2.63}$$

The next step is to find the mean free path by using techniques from dense-gas kinetic theory. Let $\mathbf{k}$ represent the unit vector from the center of particle 1 to particle 2. Then $\sigma^2(\mathbf{c}_{12} \cdot \mathbf{k})d\mathbf{k}$ is the oblique volume in which particle 2 will collide with particle 1 per unit time for particles 1 and 2 with the relative position vector between $\mathbf{k}$ and $\mathbf{k} + d\mathbf{k}$ (Chapman and Cowling 1970). The collision frequency is

$$\begin{aligned} \psi_c &= \sigma^2 \int_{\mathbf{c}_{12} \cdot \mathbf{k} > 0} (\mathbf{c}_{12} \cdot \mathbf{k}) \; f^{(2)}(\mathbf{r} - \tfrac{1}{2}\sigma\mathbf{k}, \mathbf{c}_1, \mathbf{r} + \tfrac{1}{2}\sigma\mathbf{k}, \mathbf{c}_2; t) \; d\mathbf{k} d\mathbf{c}_1 d\mathbf{c}_2 \\ &= 4n^2\sigma^2 g_0(\nu)\sqrt{\pi\Upsilon}. \end{aligned} \tag{2.64}$$

The collision interval, which is the mean time between two successive collisions, t_c, is

$$t_c = \frac{n}{\psi_c} = \frac{1}{4n\sigma^2 g_0(\nu)\sqrt{\pi\Upsilon}}. \tag{2.65}$$

The mean free path is the product of mean absolute velocity $\bar{C}$ and the collision interval, t_c, so

$$\lambda_l = \bar{C} t_c = \frac{\bar{C}}{4n\sigma^2 g_0(\nu)\sqrt{\pi\Upsilon}}, \tag{2.66}$$

where $\bar{C}$ in Equation (2.66) is defined as

$$\bar{C} = \int C\, f^{(1)}(\mathbf{r}, \mathbf{c}; t)\, d\mathbf{c} = \sqrt{\frac{8\Upsilon}{\pi}}. \tag{2.67}$$

By introducing Equation (2.67) into Equation (2.66) and using $\nu = \pi n \sigma^3/6$, the mean free path is

$$\lambda_l = \frac{\sigma}{6\sqrt{2}\nu g_0(\nu)}. \tag{2.68}$$

Finally, the local heat flux is determined,

$$q_y = -\frac{\rho c_p}{9\sqrt{\pi}} \frac{\sigma}{\nu g_0(\nu)} \Upsilon^{1/2} \frac{dT}{dy}, \tag{2.69}$$

and the effective conductivity k_{eff} is

$$k_{eff} = \frac{\rho c_p}{9\sqrt{\pi}} \frac{\sigma}{\nu g_0(\nu)} \Upsilon^{1/2}. \tag{2.70}$$

The expression for the effective conductivity is similar to that for the diffusion coefficient since each increases with σ and $\Upsilon^{1/2}$ and decreases with $g_0(\nu)$.

2.4 Binary Mixture of Granular Materials

2.4.1 Introduction

The three previous sections discuss the transport mechanisms in a single-sized granular flow. However, in real applications, the particle sizes are usually not uniform. Because of the complications involved in the transport of multicomponent mixtures, this topic receives little attention.

The following is a brief outline of the recent studies about a binary mixture of granular materials. Shen (1984) used mixing-length kinetic theory concepts to study

binary-sized mixtures in a highly-concentrated simple-shear flow. The particles were of the same material, frictionless, inelastic and spherical. Shen calculated the normal and the shear stresses and compared with Savage and Sayed's (1984) experimental results. Farrell et al. (1986) followed the dense-gas kinetic theory for mixtures to derive the governing equations for a binary-mixture of smooth, slightly inelastic, spherical granular particles. They also calculated the stresses generated in a simple shear flow with high solid fraction. The results were compared with Shen's (1984) theoretical and Savage and Sayed's (1984) experimental results. However, both of these theoretical studies only considered the collisional mode of the stresses. Jenkins and Mancini (1987) used the more rigorous kinetic theory to derive the balance laws and the constitutive relations for the plane flow of a dense, binary mixture of smooth, nearly elastic, circular disks. In this study, both the kinetic and the collisional modes were considered. Jenkins and Mancini (1989) used revised Enskog theory to develop the kinetic theory for binary mixtures of smooth, nearly elastic spheres. The current study follows the approach by Jenkins and Mancini (1989) but focuses on the granular thermal diffusion problems.

In binary or multisize mixtures, a phenomena called "segregation" may occur. Segregation may result from differences in the particle size, the particle mass, the properties of materials, and the angle-of-repose of the material (Johanson 1978). Savage and Lun (1988) proposed and analyzed two mechanisms due to size difference: "random fluctuating sieve" mechanism and "squeeze expulsion" mechanism. The random fluctuating sieve mechanism results from the induced gravity, in which the smaller particles more easily fill in the voids. The "squeeze expulsion" mechanism

describes the process in which a particle could be squeezed out to another layer because the contact forces are not balanced. Segregation is important and is broadly discussed in the industrial fields involving powders and granular materials (Johanson 1978). Some studies about this complicated phenomena have been reviewed by Savage (1987). However, the present study is interested in the segregation caused by the granular thermal diffusion.

2.4.2 Revised Enskog Theory and Governing Equations

Enskog was the first person to consider the collisional transfer in dense gases, but he only considered the single-sized particles. His theory and work in this field was fully described by Chapman and Cowling (1970). Throne extended Enskog theory to the binary mixtures of hard spheres. This extended theory was also outlined by Chapman and Cowling (1970).

Similar to the single species of dense gases, a radial distribution function describing the probability of the collisions between two particles should be evaluated. Since the particles are of different size and mass in the mixture, it is difficult to define the local density to evaluate the radial distribution function in a non-equilibrium flow. Barajas et al. (1973) evaluated the radial distribution function at three different locations: the midpoint of the line connecting the two colliding particles, the contact point, and the mass center of the two colliding particles. They found that neither of these choices was satisfactory because the diffusion force was in conflict with irreversible thermodynamics.

Instead of using a specific point to evaluate the radial distribution function in the

standard Enskog theory (SET), van Beijeren and Ernst (1973) proposed a modified Enskog theory (referred by López de Haro et al. (1983) as revised Enskog theory — RET) which took the radial distribution function at the contact point as a nonlocal functional of the density field. The results from the RET were found to be consistent with irreversible thermodynamics. López de Haro et al. (1983) employed the RET to the multicomponent mixtures and derived the linear transport theory. Jenkins and Mancini (1989) extended this theory to binary mixtures of smooth, nearly elastic spheres.

Let the subscripts α and β represent two different species in the binary-mixture, and i, j are either α or β. Similar to Equations (2.1)–(2.3) for the single species, the singlet velocity distribution functions $f_i^{(1)}(\mathbf{r}_i, \mathbf{c}_i; t)$, the Maxwellian distribution functions $f_i^{(0)}(\mathbf{r}_i, \mathbf{c}_i; t)$ and the ensemble-average of a single-particle property of the ith species Ψ_i are defined as

$$f_i^{(1)}(\mathbf{r}_i, \mathbf{c}_i; t) = f_i^{(0)}(\mathbf{r}_i, \mathbf{c}_i; t)\ (1 + \Phi_i), \tag{2.71}$$

$$f_i^{(0)}(\mathbf{r}_i, \mathbf{c}_i; t) = \frac{n_i}{(2\pi\Upsilon_i)^{\frac{3}{2}}} \exp\left(-\frac{(\mathbf{c}_i - \mathbf{u}_i)^2}{2\Upsilon_i}\right), \tag{2.72}$$

and

$$< \Psi_i >= \frac{1}{n_i} \int \Psi_i\ f_i^{(1)}(\mathbf{r}_i, \mathbf{c}_i; t)\ d\mathbf{c}_i, \tag{2.73}$$

where Υ_i is the granular temperature of species i defined by $\Upsilon_i \equiv < C_i^2 > /3$. The granular temperature of the mixture is defined by

$$\Upsilon = \frac{1}{m_0 n}(\rho_\alpha \Upsilon_\alpha + \rho_\beta \Upsilon_\beta), \tag{2.74}$$

where n is the total number density, $n = n_\alpha + n_\beta$, ρ_α and ρ_β are the bulk densities for the two species in the flows, $\rho_i = \rho_{pi}\nu_i = m_i n_i$, and m_0 is the sum of the masses

of particles α and β, $m_0 = m_\alpha + m_\beta$. For a binary mixture, the equipartition of fluctuating energy is assumed (Shen 1984; Farrell et al. 1986):

$$\frac{3}{2} m_\alpha \Upsilon_\alpha = \frac{3}{2} m_\beta \Upsilon_\beta. \tag{2.75}$$

Then the Maxwellian distribution function for the ith species is rewritten as

$$f_i^{(0)}(\mathbf{r}_i, \mathbf{c}_i; t) = n_i \Big(\frac{m_i}{2\pi m_0 \Upsilon}\Big)^{\frac{3}{2}} \exp\Big(-\frac{m_i C_i^2}{2 m_0 \Upsilon}\Big). \tag{2.76}$$

The pair-distribution function for particles i and j is defined as

$$\begin{aligned} f_{ij}^{(2)}(\mathbf{r} - \frac{1}{2}\sigma_{ij}\mathbf{k}, \mathbf{c}_i, \mathbf{r} + \frac{1}{2}\sigma_{ij}\mathbf{k}, \mathbf{c}_j; t) &= g_{ij}(\mathbf{r} - \frac{1}{2}\sigma_{ij}\mathbf{k}, \mathbf{r} + \frac{1}{2}\sigma_{ij}\mathbf{k}; t) \\ &\times f_i^{(1)}(\mathbf{r} - \frac{1}{2}\sigma_{ij}\mathbf{k}, \mathbf{c}_i; t) f_j^{(1)}(\mathbf{r} + \frac{1}{2}\sigma_{ij}\mathbf{k}, \mathbf{c}_j; t), \end{aligned} \tag{2.77}$$

where g_{ij} is the radial distribution function of two particles evaluated when particles are in contact, $\mathbf{k}$ is the unit vector directing from particle i to j, and σ_{ij} is the average diameter of the two particles, $\sigma_{ij} = (\sigma_i + \sigma_j)/2$ as shown in Figure 2.4.

The two kinetic equations derived by López de Haro et al. (1983) are

$$\begin{aligned} \Big(\frac{\partial}{\partial t} + \mathbf{c}_i \cdot \nabla + \mathbf{F}_i \cdot \frac{\partial}{\partial \mathbf{c}_i}\Big) f_i^{(1)}(\mathbf{r}_i, \mathbf{c}_i; t) &= \sum_{j=\alpha,\beta} \int_{\mathbf{c}_{ij}\cdot\mathbf{k}>0} \sigma_{ij}^2 (\mathbf{c}_{ij} \cdot \mathbf{k}) \\ \times \Big[& g_{ij}(\mathbf{r}, \mathbf{r} + \sigma_{ij}\mathbf{k}) f_i^{(1)}(\mathbf{r}, \mathbf{c}_i'; t) f_j^{(1)}(\mathbf{r} + \sigma_{ij}\mathbf{k}, \mathbf{c}_j'; t) \\ - \; & g_{ij}(\mathbf{r}, \mathbf{r} - \sigma_{ij}\mathbf{k}) f_i^{(1)}(\mathbf{r}, \mathbf{c}_i; t) f_j^{(1)}(\mathbf{r} + \sigma_{ij}\mathbf{k}, \mathbf{c}_j; t) \Big] d\mathbf{k} d\mathbf{c}_j, \end{aligned} \tag{2.78}$$

where $\mathbf{F}_i$ are the specific external forces of particles of species i, and $'$ means the velocities after the collision.

Similar to Equation (2.7), the change rate of $< n_i \Psi_i >$ is

$$\begin{aligned} \frac{\partial}{\partial t} < n_i \Psi_i > &= n_i < \mathbf{F}_i \cdot \frac{\partial \Psi_i}{\partial \mathbf{c}_i} > - \nabla \cdot < n_i \mathbf{c}_i \Psi_i > \\ &+ \sum_{j=\alpha,\beta} \Big[\chi_{ij}(\Psi_i) - \nabla \cdot \mathbf{\Theta}_{ij}(\Psi_i) \Big]. \end{aligned} \tag{2.79}$$

The last two terms represent the collisional contribution: χ_{ij} is the "source-like" contribution,

$$\begin{aligned}\chi_{ij}(\Psi_i) &= \frac{\sigma_{ij}^2}{2}\int_{\mathbf{c}_{ij}\cdot\mathbf{k}>0}(\Psi_i' + \Psi_j' - \Psi_i - \Psi_j)(\mathbf{c}_{ij}\cdot\mathbf{k}) \\ &\times f_{ij}^{(2)}(\mathbf{r} - \frac{1}{2}\sigma_{ij}\mathbf{k}, \mathbf{c}_i, \mathbf{r} + \frac{1}{2}\sigma_{ij}\mathbf{k}, \mathbf{c}_j; t)d\mathbf{k}d\mathbf{c}_i d\mathbf{c}_j, \end{aligned} \tag{2.80}$$

and $\mathbf{\Theta}_{ij}$ is the collisional flux,

$$\begin{aligned}\mathbf{\Theta}_{ij}(\Psi_i) &= -\frac{\sigma_{ij}^3}{2}\int_{\mathbf{c}_{ij}\cdot\mathbf{k}>0}(\Psi_i' - \Psi_i)(\mathbf{c}_{ij}\cdot\mathbf{k})\mathbf{k} \\ &\times f_{ij}^{(2)}(\mathbf{r} - \frac{1}{2}\sigma_{ij}\mathbf{k}, \mathbf{c}_i, \mathbf{r} + \frac{1}{2}\sigma_{ij}\mathbf{k}, \mathbf{c}_j; t)d\mathbf{k}d\mathbf{c}_i d\mathbf{c}_j, \end{aligned} \tag{2.81}$$

where $'$ denotes the properties after the collision.

Substituting $\Psi_i = m_i$ into Equation (2.79), the diffusion equation for species i is obtained:

$$\frac{\partial \rho_i}{\partial t} + \nabla\cdot(\rho_i \mathbf{u}_i) = 0. \tag{2.82}$$

By summing the diffusion equations for different species and using the mass average velocity $\mathbf{u} = (\rho_\alpha \mathbf{u}_\alpha + \rho_\beta \mathbf{u}_\beta)/\rho$, then the conservation equation of mass is derived:

$$\frac{d\rho}{dt} = -\rho\nabla\cdot\mathbf{u}, \tag{2.83}$$

where ρ is the (total) bulk flow density, $\rho = \rho_\alpha + \rho_\beta$. Using a similar procedure as above but taking $\Psi_i = m_i\mathbf{c}_i$ and $m_i c_i^2/2$, the conservation equations of momentum and fluctuating energy are determined:

$$\rho\frac{d\mathbf{u}}{dt} = -\nabla\cdot\mathbf{P} + \rho_\alpha\mathbf{F}_\alpha + \rho_\beta\mathbf{F}_\beta \tag{2.84}$$

and

$$\frac{3}{2}m_0 n\frac{d\Upsilon}{dt} - \frac{3}{2}m_0\Upsilon\nabla\cdot(n_\alpha\mathbf{v}_\alpha + n_\beta\mathbf{v}_\beta) = -\nabla\cdot\mathbf{\Gamma} - \mathbf{P}:\nabla\mathbf{u} + \rho_\alpha\mathbf{v}_\alpha\cdot\mathbf{F}_\alpha + \rho_\beta\mathbf{v}_\beta\cdot\mathbf{F}_\beta - \gamma, \quad (2.85)$$

where $\mathbf{v}_i$ is the diffusion velocity of species i,

$$\mathbf{v}_i = < \mathbf{C}_i > . \quad (2.86)$$

The pressure tensor has contributions from the kinetic mode $\mathbf{P}_k$ and the collisional mode $\mathbf{P}_c$:

$$\mathbf{P} = \mathbf{P}_k + \mathbf{P}_c, \quad (2.87)$$

where

$$\mathbf{P}_k = \sum_{i=\alpha,\beta}\mathbf{P}_{k,ii} = \sum_{i=\alpha,\beta}\rho_i < \mathbf{C}_i\mathbf{C}_i >, \quad (2.88)$$

and

$$\mathbf{P}_c = \sum_{i=\alpha,\beta}\sum_{j=\alpha,\beta}\mathbf{P}_{c,ij} = \sum_{i=\alpha,\beta}\sum_{j=\alpha,\beta}\mathbf{\Theta}_{ij}(m_i\mathbf{C}_i). \quad (2.89)$$

The fluctuating energy flux $\mathbf{\Gamma}$ is also composed of the kinetic mode $\mathbf{\Gamma}_k$ and the collisional mode $\mathbf{\Gamma}_c$:

$$\mathbf{\Gamma} = \mathbf{\Gamma}_k + \mathbf{\Gamma}_c, \quad (2.90)$$

where

$$\mathbf{\Gamma}_k = \sum_{i=\alpha,\beta}\mathbf{\Gamma}_{ki} = \sum_{i=\alpha,\beta}\frac{1}{2}\rho_i < C_i^2\mathbf{C}_i >, \quad (2.91)$$

and

$$\mathbf{\Gamma}_c = \sum_{i=\alpha,\beta}\sum_{j=\alpha,\beta}\mathbf{\Gamma}_{c,ij} = \sum_{i=\alpha,\beta}\sum_{j=\alpha,\beta}\mathbf{\Theta}_{ij}(\frac{1}{2}m_i C_i^2). \quad (2.92)$$

The energy dissipation due to the inelastic collisions per unit volume is denoted by γ and is evaluated as:

$$\gamma = -\sum_{i=\alpha,\beta}\sum_{j=\alpha,\beta}\chi_{ij}(\frac{1}{2}m_i C_i^2). \tag{2.93}$$

2.4.3 Expressions for the Constitutive Relations

Similar to the method by Chapman and Cowling (1970), Jenkins and Mancini (1989) expressed the perturbation term of the singlet velocity distribution function Φ_i as

$$\Phi_i = -\mathbf{A}_i \cdot \nabla \ln \Upsilon - \mathbf{B}_i : \nabla \mathbf{u} + H_i \nabla \cdot \mathbf{u} - \mathbf{D}_i \cdot \mathbf{d}_i + \sum_{j=\alpha,\beta} L_{ij}(1 - e_{p,ij}), \tag{2.94}$$

where $e_{p,ij}$ is the restitution coefficient between particles i and j, and $\mathbf{d}_i$ is the diffusion force:

$$\begin{aligned}\mathbf{d}_i &= \frac{-\rho_i}{m_0 n \rho \Upsilon}\Big[\nabla P + \sum_{j=\alpha,\beta}\rho_j(\mathbf{F}_i - \mathbf{F}_j)\Big] + \sum_{j=\alpha,\beta}\frac{n_i}{n}(\delta_{ij} + \frac{4}{3}\pi n_j \sigma_{ij}^3 M_{ij} g_{cij})\nabla \ln \Upsilon \\ &+ \sum_{j=\alpha,\beta}\frac{n_i}{m_0 n \Upsilon}\Big(\frac{\partial \mu_i}{\partial n_j}\nabla n_j\Big),\end{aligned} \tag{2.95}$$

where P is the "granular pressure" (normal stress), δ_{ij} is the Kronecker delta and $M_{ij} \equiv m_i/m_{ij} = m_i/(m_i + m_j)$. The diffusion force is the main difference that results from using RET instead of SET. In Equation (2.95), g_{cij} is the equilibrium value of the radial distribution function for particles i and j at contact which is found by substituting the local density as the equilibrium density and is expressed as (Kincaid et al 1983; Jenkins and Mancini 1989)

$$g_{cij} = \Big[Z^2 + \frac{3\sigma_i\sigma_j}{\sigma_i + \sigma_j} Z Z_2 + 2\Big(\frac{\sigma_i\sigma_j}{\sigma_i + \sigma_j}\Big)^2 Z_2^2\Big]\Big/ Z^3, \tag{2.96}$$

where

$$Z_l = \frac{\pi}{6}\sum_{j=\alpha,\beta} n_j \sigma_j^l, \qquad l = 1,2,3; \qquad Z = 1 - Z_3. \tag{2.97}$$

Note that Z_3 is equal to the total solid fraction, $Z_3 = \nu = \nu_\alpha + \nu_\beta$. This equilibrium radial distribution function is originally derived by Mansoori et al. (1971) and is known as Carnahan-Starling approximation. In Equation (2.95), μ_i denotes the "granular chemical potential" of species i which depends on the radial distribution function used. Corresponding to the form of equilibrium distribution function derived by Mansoori et al., the granular chemical potential μ_i is expressed as (Reed and Gubbins 1973)

$$\begin{aligned}\frac{\mu_i}{m_0\Upsilon} &= \ln n_i - \ln(1-Z_3) + \frac{\pi\sigma_i^3 P}{6m_0\Upsilon} + \frac{3Z_2\sigma_i + 3Z_1\sigma_i^2}{Z} \\ &+ \frac{9Z_2^2\sigma_i^2}{2Z^2} + 3\left(\frac{Z_2\sigma_i}{Z_3}\right)^2\left[\ln Z + \frac{Z_3}{Z} - \frac{Z_3^2}{2Z^2}\right] \\ &- \left(\frac{Z_2\sigma_i}{Z_3}\right)^3\left[2\ln Z + \frac{Z_3(2-Z_3)}{Z}\right]. \end{aligned} \tag{2.98}$$

In Equation (2.94), $\mathbf{A}_i$, $\mathbf{B}_i$, H_i, $\mathbf{D}_i$ and L_{ij} are functions of $\mathbf{C}_i$. By expanding $\mathbf{A}_i$, $\mathbf{B}_i$, H_i, $\mathbf{D}_i$ and L_{ij} as Sonine polynomials, Jenkins and Mancini (1989) solved Equation (2.78) in the first-order approximation and found that the velocity distribution functions were independent of the inelasticity of the collisions for this order of approximation. It should be noted that the particles treated here are slightly inelastic; otherwise, the inelasticity would enter the first-order solution. By substituting the first-order of the velocity distribution function into Equations (2.87)–(2.93), the stresses, the fluctuating energy flux and the energy dissipation can be determined.

The normal stress or the granular pressure in the mixture P is

$$P = m_0\Upsilon(n + \sum_{i=\alpha,\beta}\sum_{j=\alpha,\beta}\frac{2}{3}\pi n_i n_j \sigma_{ij}^3 g_{cij}). \tag{2.99}$$

When there is no diffusion, the shear stress is given by

$$P_{nl} = -\mu \frac{\partial \mu_n}{\partial r_l}, \qquad n, l, r_l = x, y, z, \quad k \neq l, \tag{2.100}$$

where μ is the mixture viscosity:

$$\begin{aligned} \mu &= \frac{1}{2} \sum_{i=\alpha,\beta} b_{i0} m_0 \Upsilon \Big(n_i + \frac{8}{15} \sum_{j=\alpha,\beta} M_{ji} \pi n_i n_j \sigma_{ij}^3 g_{cij} \Big) \\ &+ \frac{4}{15} \sum_{i=\alpha,\beta} \sum_{j=\alpha,\beta} \Big(\frac{2\pi m_0 m_i m_j \Upsilon}{m_{ij}} \Big)^{\frac{1}{2}} n_i n_j \sigma_{ij}^4 g_{cij}. \end{aligned} \tag{2.101}$$

In Equation (2.101), b_{i0} is the coefficient of the first-order term in the Sonine polynomial expansion of $\mathbf{B}_i$ and expressed as

$$\begin{aligned} b_{i0} &= 5 \Big[b_i \sum_{j=\alpha,\beta} n_i (\delta_{ij} + \frac{8}{15} \pi n_j \sigma_{ij}^3 g_{cij} M_{ji}) \\ &+ \frac{32}{3} \sigma_{\alpha\beta}^2 (\frac{\pi m_\alpha m_\beta}{2m_0^3})^{\frac{1}{2}} \sum_{j=\alpha,\beta} (1 - \delta_{ij}) (n_j + \sum_{k=\alpha,\beta} \frac{8}{15} \pi n_j n_k \sigma_{jk}^3 g_{cjk} M_{kj}) \Big] \\ &\div \Big\{ g_{c\alpha\beta} n_\alpha n_\beta (m_0 \Upsilon)^{\frac{1}{2}} \Big[b_\alpha b_\beta - \frac{512}{9} \sigma_{\alpha\beta}^4 \pi m_\alpha m_\beta / m_0^3 \Big] \Big\}, \end{aligned} \tag{2.102}$$

where

$$b_i = 40 \sigma_{\alpha\beta}^2 \Big(\frac{\pi m_\alpha m_\beta}{2m_0^3} \Big)^{\frac{1}{2}} \Big(\frac{2}{3} + \frac{2}{5} \frac{m_i}{m_k} \Big) + \frac{n_k g_{ckk}}{n_i g_{cik}} 8 \sigma_k^2 \Big(\frac{\pi}{m_k} \Big)^{\frac{1}{2}}, \quad k \neq i. \tag{2.103}$$

When there is no diffusion, the fluctuating energy flux is expressed as

$$\Gamma_l = -\lambda \frac{\partial \Upsilon}{\partial r_l}, \qquad l, r_l = x, y, z, \tag{2.104}$$

where λ is

$$\begin{aligned} \lambda = &- \frac{5}{4} m_0 \sum_{i=\alpha,\beta} a_{i1} \Big(\frac{2m_0 \Upsilon}{m_i} \Big)^{\frac{1}{2}} (n_i + \frac{8}{5} \sum_{j=\alpha,\beta} M_{ij} M_{ji} \pi n_i n_j \sigma_{ij}^3 g_{cij}) \\ &+ \frac{4}{3} m_0 \sum_{i=\alpha,\beta} \sum_{j=\alpha,\beta} \Big(\frac{2\pi m_0 m_i m_j \Upsilon}{m_{ij}^3} \Big)^{\frac{1}{2}} n_i n_j \sigma_{ij}^4 g_{cij}. \end{aligned} \tag{2.105}$$

In Equation (2.105), a_{i1} is the coefficient of the first-order term in the Sonine polynomial expansion of $\mathbf{A}_i$ and expressed as

$$\begin{aligned} a_{i1} &= 15\Big[a_i \sum_{j=\alpha,\beta} n_i(\delta_{ij} + \frac{8}{5}\pi n_j \sigma_{ij}^3 g_{cij} M_{ij} M_{ji}) \\ &+ 54 m_i \Big(\frac{\pi m_\alpha m_\beta}{2m_0^5}\Big)^{\frac{1}{2}} \sigma_{\alpha\beta}^2 \sum_{j=\alpha,\beta} (1-\delta_{ij})(n_j + \sum_{k=\alpha,\beta} \frac{8}{5}\pi n_j n_k \sigma_{jk}^3 g_{cjk} M_{kj} M_{jk})\Big] \\ &\div \Big\{2 g_{c\alpha\beta} n_\alpha n_\beta (2m_i)^{\frac{1}{2}} (1458 \sigma_{\alpha\beta}^4 \pi M_{\alpha\beta}^2 M_{\beta\alpha}^2 / m_0 - a_\alpha a_\beta)\Big\}, \end{aligned} \tag{2.106}$$

where

$$\begin{aligned} a_i &= 40\sigma_{\alpha\beta}^2 \Big(\frac{\pi m_i}{m_k m_0}\Big)^{\frac{1}{2}} \Big(\frac{3}{2} M_{ki}^2 + \frac{13}{20} M_{ik}^2 + \frac{4}{5} M_{ik} M_{ki}\Big) \\ &+ \frac{n_k g_{ckk}}{n_i g_{cik}} 8\sigma_k^2 \Big(\frac{\pi}{m_k}\Big)^{\frac{1}{2}}, \qquad k \neq i. \end{aligned} \tag{2.107}$$

The energy dissipation due to the inelastic collisions per unit volume is derived as

$$\gamma = \sum_{i=\alpha,\beta} \sum_{j=\alpha,\beta} 4 g_{cij} \sigma_{ij}^2 n_i n_j M_{ji} \frac{1 - e_{p,ij}^2}{2} \Big(\frac{2\pi m_{ij} m_0^3 \Upsilon^3}{m_i m_j}\Big)^{\frac{1}{2}}. \tag{2.108}$$

From Equation (2.86), the difference between the diffusion velocities of the two species is determined from

$$\mathbf{v}_\alpha - \mathbf{v}_\beta = -\frac{n^2}{n_\alpha n_\beta} D_{\alpha\beta} \Big(\mathbf{d}_\alpha + k_\Upsilon \frac{1}{\Upsilon} \nabla \Upsilon\Big), \tag{2.109}$$

where $D_{\alpha\beta}$ is the diffusion coefficient given by

$$D_{\alpha\beta} = \frac{3}{2n} \Big(\frac{2\Upsilon}{\pi M_{\alpha\beta} M_{\beta\alpha}}\Big)^{\frac{1}{2}} \frac{1}{8\sigma_{\alpha\beta}^2 g_{c\alpha\beta}} \tag{2.110}$$

and k_Υ is granular-thermal-diffusion ratio expressed as

$$k_\Upsilon = \frac{4}{3} \pi^{\frac{1}{2}} \sigma_{\alpha\beta}^2 \frac{n_\alpha n_\beta}{n} \Big[M_{\beta\alpha}^{\frac{3}{2}} a_{\alpha 1} - M_{\alpha\beta}^{\frac{3}{2}} a_{\beta 1}\Big]. \tag{2.111}$$

Since there is no mass transfer during collisions, the mutual diffusion only depends on the kinetic mode.

The self-diffusion process in a single species granular flow has been studied in the earlier section. For the binary-mixture, there is a new diffusion mechanism, granular thermal diffusion, that results from the granular temperature gradient as indicated in Equation (2.109). The granular-thermal-diffusion ratio k_Υ is the ratio of the granular thermal diffusion coefficient D_Υ to the mutual-diffusion coefficient $D_{\alpha\beta}$. From Equation (2.111), k_Υ is 0 if the two species are identical meaning there is no granular thermal diffusion process for a single-species granular flow. The granular-thermal-diffusion ratio in Equation (2.109) is positive if species α is more massive, or if α is of larger size than species β. The effect of the granular thermal diffusion is that the lighter or the smaller particles move to the position with higher granular temperature, and the heavier or the larger particles move in the opposite direction. This phenomena has been indicated by the theoretical development and some experiments for gases and liquids (Chapman and Cowling 1970). The details of granular thermal diffusion process are presented in Chapter 5.

The diffusion coefficient given by Equation (2.110) has the same form as derived by Throne for the perfectly-elastic dense gases. Since the present theory neglects the higher order terms, the inelasticity does not enter the equation. If the two species are identical, then Equation (2.110) is the same as the diffusion coefficient shown in Equation (2.47) by substituting $e_p = 1$. Although the diffusion coefficient derived by RET is the same as that derived by SET, the diffusion force is different which causes a different diffusion flux.

Chapter 3

Experimental Study of Granular Flows in a Vertical Channel

3.1 Experimental Apparatus and Procedures

3.1.1 Facility

The present experiment was designed to study diffusion in granular material flows. Two differently-colored but otherwise-identical particle streams were mixed in a vertical channel. The bulk ensemble-average velocities, the fluctuating velocities and the mixing layer thicknesses were measured.

Figure 3.1 shows the schematic drawing of the granular-flow mixing layer facility. The particles entered the test section from an upper feed hopper. A thin metal splitter plate was placed in the center of the hopper and extended about 2 cm into the test section to separate the two different colored streams. On one side of the

splitter plate the particles were dyed black, and on the other side the particles were fluorescent yellow; aside from the difference in color, the particles were identical glass spheres. The test section was 1 m in height, 2.18 cm in depth, and had adjustable side walls. The material flow rate was controlled by the size of the opening of the lower hopper and was determined by collecting the material exiting the test section over a designated period of time and weighing the sample.

Two tempered-glass plates were used as the front and back surfaces. Since there were dirt and static charge left on the surface after the particles slipped past, the plates were removed to be cleaned and polished after every two to three experimental runs in order to create a two-dimensional flow. As shown by the experimental results, the surface conditions of the side walls influenced the velocity profiles and the diffusion experiments. The present experiments were composed of three side-wall conditions: polished glass walls, walls roughened by adhering a layer of 3-mm diameter glass spheres to the surface, and aluminum walls with 120° saw-tooth V-grooves of 3-mm depth.

Glass beads with particle density, $\rho_p = 2490$ kg/m^3, were used as the granular materials. The sizes of particles and the channel width, $2H$, also influenced the experimental results. The average particle diameters, σ, of 3-mm, 2-mm and 1-mm were used. Most of the experiments used the 3-mm glass beads and two different channel widths: the narrow channel of 3.81 cm ($2H/\sigma = 12.7$), and the wide channel of 5.08 cm ($2H/\sigma = 17.0$). For the roughened and saw-tooth side walls, the channel width was measured between the outer edges of the attached particles or between the tips of the peaks. The experiments were performed for low and high flow rates

which corresponded to average velocities of about 5 cm/sec and 10 cm/sec. Since the roughened and saw-tooth walls offered a slightly larger flow cross-section than the smooth walls, the mass flow rates were larger for these wall conditions. Some additional experiments were performed at higher flow rates; however, based on visual observations the flow appeared to surge especially for the smooth and the roughened side walls.

For the roughened and saw-tooth walls, a total of eight experiments were conducted using 3-mm diameter beads for the two flow rates, and the two channel sizes. As shown in Section 3.2.2, the largest mixing-layer thickness was approximately 4σ at a downstream distance of $x/\sigma = 300$. To increase the mixing layer thickness relative to the particle size, additional experiments were conducted using smaller beads of 1-mm and 2-mm diameters. For the 2-mm beads, the channel width using the saw-tooth sides was 2.54 cm, which corresponded to $2H/\sigma = 12.7$ — the same ratio of width to particle diameter as in the narrow channel with the 3-mm beads. For 1-mm beads, the smallest channel size possible was 1.59 cm ($2H/\sigma = 15.9$). With the smaller particle diameters, it was possible to use higher average velocities without an apparent surging problem. As a result, the average velocities using the 1-mm and 2-mm beads were approximately 18 cm/sec.

The average solid fraction, ν, was determined from the equation $\nu = \dot{m}/\rho_p u_{xa} A_c$ where $\dot{m}$ was the mass flow rate, u_{xa} was the average velocity across the channel which was determined from the velocity profiles, and A_c was the channel cross-sectional area. Because of the additional flow area caused by the surfaces of the roughened and saw-tooth channels, the effective channel width was estimated as the distance

$2H + \sigma$. For all experiments, the solid fraction ranged from approximately 0.59 to 0.64. The maximum shearable solid fraction, ν^* was about 0.65. The distribution of the local solid fraction was not measured, because of the observations of the flow that indicated the variation appeared to be small and within the uncertainty of the measurement technique.

3.1.2 Velocity Measurements

Savage (1979) first introduced the use of fibre optic probes to measure velocities in granular flows. Later Ahn et al. (1991) developed a similar system and successfully measured the velocities, the velocity-fluctuations and the one-dimensional solid fractions of the granular flows at the base, the free surface and the side walls of the chute. This technique was modified to apply to the measurements of the present experiments.

Two MTI 062H fibre-optic displacement probes were placed in a holder that was mounted flush to the front tempered glass plate as shown in Figure 3.2. The holder could be moved upwards or downwards, and to the left or to the right so that measurements in different positions were possible. The probes were hemispherical-type, i.e., all the filaments in a semi-circle of the probe face emitted light and those in the other semi-circle received light. The diameter of the probe was 1.6-mm. The two probes were arranged as shown in Figure 3.3. They were spaced center-to-center 4.5-mm apart for the 3-mm beads, and 2.5-mm apart for the 2-mm beads. The velocity profiles were not measured for the 1-mm beads, because the uncertainty in the measurement technique increased significantly when the fibre optic probe was

larger than the size of the beads.

The signals from the receiving parts of the two fibre optic displacement probes were transferred to the voltage outputs through two MTI KD-300 fotonic sensors. The Data Translation DT2811-PGH consisting of 16 channels of analog-digital converter was used to digitize the voltage outputs and then to store the digitized data. The DT2811-PGH was connected to an 8253 Intel Programmable Timer which was used to measure the time. The timer was installed inside a Zenith 386 personal computer. A software program written in C controlled the whole process including the sampling rate and the gains of the signals. There were 32,000 samples recorded in 24 seconds for each run of the experiment and between 200–300 particles were detected. The flow chart of the process is shown in Figure 3.2.

The output from the displacement probe depends on the gap between the object and the face of the probe, so a sine-like signal appears when a spherical particle passes the probe. Figure 3.4 shows a sequence of outputs when particles pass by the two probes. As shown in the figure, there is a time delay between the two signals that depends on the travel time of the particle. The upper curve was the output from the probe placed in the upstream, and the lower curve was for the downstream probe.

A BASIC program, which was originally written by Ahn (1989), was modified to analyze the samples. The first step in determining the velocities of individual particles was to calculate an average time delay between the two signal records. The average time delay was calculated by cross-correlating the entire two records from outputs of the displacement probes. Figure 3.5 shows a typical cross-correlation

curve. The average velocity, $u_{x,ave}$ was then calculated from the time delay and the spacing between the centers of the two probes.

The second part of the computer algorithm identified the passage of individual particles in each of the data records. The average signal output was computed to determine the initial threshold voltage as shown in Figure 3.4. A peak in the voltage output data was identified as a possible passage if the value of the peak was higher than the threshold voltage. In addition, the width of the peak had to be within a certain range. For the particles with diameter of σ, the peak width had to be between $0.1\sigma/u_{x,ave}$ and $\sigma/u_{x,ave}$. If the peak fell outside this range, the data corresponding to that peak was not included in the further calculations. The total number of particles that passed by this probe based on the initial threshold voltage could be counted after the above examination. Then this procedure was repeated based on an increased threshold voltage until the maximum total number of particle passages was obtained. A similar procedure was performed for the second data record.

The third part of the algorithm calculated the velocity of individual particles. For each identified peak in the upstream record, the expected time for the corresponding peak to be found in the downstream record was determined from the average time delay. At this expected time, the downstream record was examined to see if a peak occurred at that time or within a time window between 0.71 to 1.67 of the time delay. This time window corresponded to a velocity variation of $\pm$ 40% of the previously calculated average value, $u_{x,ave}$. If the peak in the second record did not occur within this range, the velocity was not calculated for the particle that was observed in the upstream record. After a particular particle was confirmed to have passed by the

two probes, the velocity of this particle could be calculated. In Ahn's program the passage time of the particular particle was calculated from the time delay between the peaks in the data records. To calculate a more accurate time delay, two-thirds of the two signals corresponding to a particle passage were cross-correlated. The reason for using two-thirds instead of the entire peaks in the cross-correlation was that the peaks might not be in the center of the signals and the widths of the two signals might not be the same. An individual particle velocity was obtained by dividing the center-to-center probe distance by the time delay. A more accurate mean velocity than that obtained from cross-correlating the two entire records was determined by averaging these individual velocities. The similar procedure was repeated twice by using the new time windows based on the newly calculated mean velocity. Finally, the ensemble-average velocity $< c_x >$ was obtained. The ensemble-average of the square of the fluctuating velocities in the flow direction, $< C_x^2 >$ was then calculated.

This method of velocity measurements was calibrated using a rotating wheel that revolved at a fix speed with a layer of particles attached to the outer periphery. The calibration error was found to be dependent on the sampling rate as shown in Figure 3.6. With a higher sampling rate, the result was more accurate but there were fewer particles detected by both probes. The sampling rate of $1/0.000785$ sec^{-1} was found to be the most suitable for the present experiment. The calibration indicated approximately a 3% error in the average velocity measurements for this sampling rate and between 200–300 particles were detected.

3.1.3 Mixing Layer Thickness Measurements

As mentioned is Section 3.1.1, two batches of differently-colored but otherwise-identical particles were placed on either side of the splitter plate in the upper hopper. After the bottom hopper was opened, the particles started to move downwards and to mix in the test section. The mixing layer increased from the end of the splitter plate. The diffusion experiments involved the visual observation of the colored particles through the front glass plate. The flow was filmed using a commercial video recorder, and the images were digitized in real time using a frame-grabber board that was operated by a personal computer. To increase the number of pixels per particle (approximately 3–4 pixels were used for a distance of one 3-mm particle diameter), the upper and lower halves of the channel were filmed separately. A digitized image was recorded at a rate of 3 images per second for a total of 50 to 90 images. The buffer size of the frame-grabber board limited the total number of images that could be stored. After recording the digitized images, the contrast between the light and dark particles was enhanced so that the dark particles appeared black and the light particles appeared white. The local ensemble-average color concentration was calculated from the enhanced images. From the averaged image, the thickness of the mixing layer, δ, was determined from the physical distance in which the color varied from 0.01 to 0.99 where 0.0 indicates black and 1.0 indicates white. The image-processing method was tested on a known distribution of particles. These tests indicated that the results were affected by the lighting and by non-uniform coloring of the particles; in the actual experiments, care was taken to minimize these effects. After each experiment, the colored beads were washed and dyed for the next experiment.

3.2 Presentation of Experimental Data

3.2.1 Velocity and Longitudinal Fluctuating Velocity Profiles

In preliminary experiments, the velocity of the flow was measured at several locations along the channel to determine the distance over which the profile developed. The velocity profile appeared to develop within the first 3 to 4 particles downstream of the splitter plate. After this initial entrance region, no significant variation was detected with the downstream position except in the region within 10 cm of the exit hopper. All of the following velocity measurements were obtained at a position approximately halfway down the length of the channel (x = 50 cm, x = 0 at the position of the end of the splitter plate) and were presented in terms of non-dimensional distance y/H measured from the channel centerline. The data closest to the channel wall were located 0.8 mm from the edge of the surface. This location was the closest to the wall that the 1.6-mm diameter fibre-optic probe could be placed. The velocity measured at this position is referred to as the slip velocity.

Figures 3.7–3.12 indicate the distributions in the ensemble-average local velocity u_x and in the root-mean-square of the fluctuating velocity in the flow direction, $u'_x = < C_x^2 >^{1/2}$ across the half channel. The local velocity profiles are normalized by the average velocity across the channel based on the experimental results. The r.m.s. fluctuating velocity profiles are normalized by the local velocity. Figure 3.7 is for the 3-mm diameter particles in the channel with polished-glass side walls for both the high and the low flow rates; the channel width is 5.08 cm. The velocity profiles are relatively flat indicating there is no shearing of the materials. Figures 3.8 and 3.9

are for the 3-mm diameter particles in the rough-walled channel with channel widths of 5.08 cm and 3.81 cm. The velocity profiles are flat in the central region, but show a significant variation near the side walls over a distance of roughly 3 to 4 particle diameters. The central plug-flow region appears to be proportionally smaller in the narrow channel. Similar profiles have been previously observed in vertical channel flows by Savage (1979).

Figures 3.10 and 3.11 are for the conditions similar to those for Figures 3.8 and 3.9 except the walls have saw-tooth grooves. The velocity profiles also appear similar; however, the dimensionless velocities are higher than in the rough-walled channel in the central region and relatively lower in the region close to the walls indicating a higher shear rate for the saw-tooth walled channel. The slip velocities in the rough-walled channel are approximately 45–60% of average velocity, and are 25–40% for the saw-tooth walled channel. Figure 3.12 is for the 2-mm diameter particles in the saw-tooth walled channel of width 2.54 cm ($2H/\sigma = 12.7$). The non-dimensional profiles appear to be similar to that shown in Figure 3.11 for the 3-mm beads in the narrow channel ($2H/\sigma = 12.7$).

Figures 3.7(b)–3.12(b) show the corresponding distributions in the r.m.s. of the fluctuating velocity in the flow direction normalized by the local velocity. The fluctuating components in the central region of the channel are approximately 14–16% of the local velocity for the high flow rates, and between 10–14% for the low flow rates. The magnitude of the fluctuating velocity as a percentage of the local velocity does not vary significantly across the channel, although for the roughened and saw-tooth channels there appears to be a slight decrease near the walls. It is important to note

that the measuring technique is designed for uni-directional flows. If the particle velocity has a tangential component, as visual observations suggest for the particles closest to the walls, the downstream fibre optic probes do not detect the particle trajectory. As a result of the transverse motion, the measurement of the streamwise component of the fluctuating velocity may decrease. The r.m.s. fluctuating velocity component for the 2-mm diameter beads is similar to that measured using the larger beads as shown by comparing Figures 3.11 and 3.12. The scatter in the velocity measurements may result from variations in the surface conditions of the front and back plates, and in the conditions of the particles from experiment to experiment.

3.2.2 Mixing Layer Thickness Profiles

Particle diffusion experiments were made using the 3-mm diameter beads for both the low and the high flow rates, and for the three different side-wall conditions; in addition, two experiments were also performed using 1-mm and 2-mm beads. The photographs in Figure 3.13 show typical particle distributions at 44 cm $< x <$ 89 cm for four different experimental cases. Figure 3.13(a) is from a flow with polished-glass side walls and shows no net diffusion of the particles. Visual observations indicate that the black particles remain on one side of the channel and the yellow particles on the other. The picture also suggests that the splitter plate does not have an observable effect on the mixing process. When the flow is sheared, however, as occurs in the three other flows shown in Figures 3.13(b), (c) and (d), some particles move across the centerline. In Figure 3.13(b), the particles are 3-mm diameter and the channel has the saw-tooth walls with the narrower width. The interface between

the dark and light particles is uneven, but few of the light particles appear to be surrounded by dark particles. Using the smaller beads, the diffusion process has increased because of the length of the channel as compared to the particle size is proportionally larger as shown in Figures 3.13(c) and (d) for the 2-mm and 1-mm diameter beads. These pictures indicate that more of the light particles have migrated into the region of the darker particles.

The mixing-layer thickness results are shown in Figures 3.14–3.20 for the glass walled channel, for the rough-walled channels, for the saw-toothed channels, and for the 2-mm and 1-mm diameter beads, respectively. The figures indicate the thickness of the non-dimensional mixing layer, δ/σ, as a function of non-dimensional downstream distance, x/σ. For glass side walls as shown in Figure 3.14, the mixing layer thickness remains constant, close to one particle in size. This result is anticipated as shown from the photograph of Figure 3.13(a) that indicates either a black or yellow particle lying at the center of the channel. For the roughened and saw-toothed surfaces, the shearing of the flow results in some transverse movement of the particles. As indicated by Figures 3.15–3.20, the thickness of the mixing layers are greater than one particle diameter and increase with downstream position. The particle diffusion is more pronounced in the narrower channels; this result may be due to the proximity of the walls to the dark-particle/light-particle interface, which then increases the transverse particle motion within the center of the channel. However, as indicated by the velocity measurements, the particle diffusion occurs in a region of the flow where there is no discernable longitudinal velocity gradient. In comparing the results in the roughened and saw-toothed channels, the diffusion in the saw-toothed channels

appears to be slightly larger; the velocity profiles show that the velocity gradient at the walls is greater with the saw-tooth sides and the larger shear rate may increase the transverse motion of the particles. By increasing the flow rate, the diffusion rates appear to increase slightly for all of the flows except for the wide rough-walled channel in which the mixing-layer thicknesses are comparable. With the larger non-dimensional channel length, the non-dimensional mixing-layer thickness at $x = 90$ cm is greater for the 2-mm and 1-mm beads as shown in Figures 3.19 and 3.20.

The curves in Figures 3.15–3.20 are for flows of constant Peclet number, $Pe = u_{xm}\sigma/D_{11,m}$ where u_{xm} and $D_{11,m}$ are the velocity and the self-diffusion coefficient within the mixing layer, and the m subscript is used to denote the average value within the mixing layer. These curves are determined from a simple analysis of the flow based on the diffusion equation. Assuming that the flow is steady with no transverse velocity and neglecting diffusion in the flow direction, the diffusion equation for the mixing layer is written as

$$u_x \frac{\partial \omega}{\partial x} = \frac{\partial}{\partial y}\left(D_{11}\frac{\partial \omega}{\partial y}\right), \tag{3.1}$$

where u_x is the local velocity, ω indicates the color concentration, and D_{11} is the local self-diffusion coefficient. If within the mixing layer the velocity and diffusion coefficient are assumed to be constant, the diffusion equation may be rewritten as

$$u_{xm}\frac{\partial \omega}{\partial x} = D_{11,m}\frac{\partial^2 \omega}{\partial y^2}. \tag{3.2}$$

Assuming that the diffusion process is not restricted by the channel boundaries, appropriate boundary conditions are that as $y \to \infty$, $\omega \to 1$, and as $y \to -\infty$, $\omega \to 0$; the initial conditions are that at $x = 0$ and $y > 0$, $\omega = 1$, and at $x = 0$ and

$y < 0$, $\omega = 0$. Using these conditions, the governing equation is integrated, yielding the following concentration distribution,

$$\omega(x,y) = \frac{1}{2} \pm \frac{1}{2}\ \mathrm{erf}\left(\frac{\pm y}{2\sqrt{x\sigma}} Pe^{\frac{1}{2}}\right), \tag{3.3}$$

where the + is for $y > 0$ and the − for $y < 0$, and erf( ) indicates the error function. From this expression the mixing layer thickness, δ/σ, is determined as

$$\frac{\delta}{\sigma} = 6.60\left(\frac{x}{\sigma}\frac{1}{Pe}\right)^{\frac{1}{2}}. \tag{3.4}$$

The analysis used to develop Equation (3.4) assumes that the thickness of the mixing layer is zero at $x = 0$. However, because of the thickness of the splitter plate in the experiments the experimental value of the initial mixing-layer thickness is probably closer to one particle diameter. As a result, the curves calculated using Equation (3.4) are shifted by one particle diameter so that $\delta/\sigma = 1$ at $x/\sigma = 0$ as shown in Figures 3.15–3.20.

The lines of constant Pe are included for reference purposes, and are drawn to bound the data. The comparison of the curves with the experimental measurements shows that δ/σ does appear to increase with $(x/\sigma)^{1/2}$. In addition, as mentioned in Section 2.3.2, the kinetic theory studies demonstrate that the self-diffusion coefficient is proportional to the square-root of the granular temperature and the particle diameter. Since the granular temperature is not measured in the present experiment, it is impossible to apply directly this result. However, by assuming $u'_x = < C_x^2 >^{1/2}$ is proportional to the square-root of the granular temperature, the self-diffusion coefficient within the mixing layer, $D_{11,m}$, would depend on the product $\sigma u'_{xm}$, and the

Peclet number follows as

$$Pe = \frac{u_{xm}\sigma}{D_{11,m}} \propto \frac{u_{xm}}{u'_{xm}}, \tag{3.5}$$

where u'_{xm} is the r.m.s. fluctuating velocity in the flow direction within the mixing layer thickness.

This proportionality given by Equation (3.5) suggests that as the ratio of the fluctuating velocity to the average velocity increases, the Peclet number decreases because of the increase in the diffusion coefficient; as a result, δ/σ should increase. The rough-walled and saw-toothed-walled experiments indicate that for the higher flow rates, the velocity fluctuations increase as a percent of the local velocity, and the corresponding mixing-layer thicknesses are slightly larger. However, the dependence of the mixing-layer thickness on the longitudinal velocity fluctuations does not explain why δ/σ is larger for the saw-tooth walls than for the roughened walls when the magnitude of the velocity fluctuations are similar for approximately equal flow rates and channel sizes. As stated previously, the curves are based on the assumption of a constant velocity and diffusion coefficient within the mixing layer. Although the measurements indicate that the local longitudinal velocity and the velocity fluctuations are relatively constant within the central region of the channel, visual observations show that the transverse particle motions vary within the flow. As a result, it is anticipated that the rate of particle diffusion does vary within the mixing layer.

Although the simple diffusion analysis does not incorporate all of the effects exhibited by the experiments, the lines suggest an appropriate scaling of the diffusion process with particle diameter. As indicated by Equation (3.5), the Peclet number is independent of the particle diameter for the same magnitude of velocity fluctuation.

By comparing the saw-tooth-wall results in the channel of $2H/\sigma = 12.7$ for the 2-mm with that for the 3-mm beads at the high flow rate (Figures 3.18 and 3.19), the growth of the mixing layer for each flow roughly follows the curves corresponding to Pe between 1500 and 3000. For the 1-mm beads, the velocity profiles were not measured and the ratio of the channel width to the particle diameter does not correspond exactly with that for the larger beads; however, the growth of the mixing-layer thickness appears to follow the same Peclet number curves as used for the larger beads.

Chapter 4

Comparisons of Experiments and Theories

4.1 Velocity and Fluctuating Velocity Profiles for the Flows in a Vertical Channel

The development of kinetic theory for granular flows is presented in Chapter 2. These equations are used to determine the fully developed velocity profiles and the mixing-layer thickness profiles in a vertical channel. These theoretical results are compared with the experiments described in the last chapter.

For the two-dimensional steady flow as shown in Figure 4.1, assuming that the velocity and granular temperature profiles are fully developed, the governing equations

can be derived from Equations (2.11) and (2.12) and be written as:

$$-\left(\frac{\partial P_{xx}}{\partial x}+\frac{\partial P_{xy}}{\partial y}\right)+\rho g=0, \tag{4.1}$$

$$\left(\frac{\partial P_{yy}}{\partial y}\right)=0, \tag{4.2}$$

and

$$-P_{xy}\frac{\partial u_x}{\partial y}-\frac{\partial \Gamma_y}{\partial y}-\gamma=0. \tag{4.3}$$

From Equations (2.24) and (2.25), for a fully developed flow, the normal stresses are

$$P_{xx}=P_{yy}=\rho_p g_1(\nu,e_p)\Upsilon; \tag{4.4}$$

the shear stresses are

$$P_{xy}=P_{yx}=-\rho_p\sigma g_2(\nu,e_p)\Upsilon^{\frac{1}{2}}\frac{du_x}{dy}, \tag{4.5}$$

and the flux of fluctuating energy in the transverse direction is

$$\Gamma_y=-\rho_p\sigma\left[g_3(\nu,e_p)\Upsilon^{\frac{1}{2}}\frac{d\Upsilon}{dy}+g_4(\nu,e_p)\Upsilon^{\frac{3}{2}}\frac{d\nu}{dy}\right]. \tag{4.6}$$

By substituting Equations (4.4)–(4.6) and (2.26) into Equations (4.1)–(4.3), the dimensionless momentum equations in the flow direction and transverse direction are

$$\frac{d}{dY}\left[g_2(\nu,e_p)\Upsilon^{*\frac{1}{2}}\frac{du_x^*}{dY}\right]+A^{\frac{3}{2}}\left(\nu-\frac{dP_{xx}^*}{dX}\right)=0 \tag{4.7}$$

and

$$\frac{d}{dY}\left[g_1(\nu,e_p)\Upsilon^*\right]=0. \tag{4.8}$$

The fluctuating energy equation is

$$\begin{aligned}&\frac{d}{dY}\left[g_3(\nu,e_p)\Upsilon^{*\frac{1}{2}}\frac{d\Upsilon^*}{dY}+g_4(\nu,e_p)\Upsilon^{*\frac{3}{2}}\frac{d\nu}{dY}\right]\\ +\;&Ag_2(\nu,e_p)\Upsilon^{*\frac{1}{2}}\left(\frac{du_x^*}{dY}\right)^2-A^2g_5(\nu,e_p)\Upsilon^{*\frac{3}{2}}=0.\end{aligned} \tag{4.9}$$

The dimensionless variables, X, Y, u_x^*, P_{xx}^* and Υ^* are defined by : $X = x/\sigma$, $Y = y/H$, $u_x^* = u_x/\sqrt{gH}$, $P_{xx}^* = P_{xx}/\rho_p g\sigma$, and $\Upsilon^* = \Upsilon/g\sigma$, and $A = H/\sigma$, where, H is the half-channel width.

For a fully-developed flow in the vertical channel, the term dP_{xx}^*/dX may still remain in the equation since the average solid fraction may vary with downstream position; in addition the function $g_1(\nu, e_p)$ is very sensitive to the variation of the solid fraction when the solid fraction is close to the maximum shearable solid fraction. The normal pressure P_{xx} may also vary due to frictional effects. By the classical analysis of Janssen (1895), the vertical pressure P_{xx} could be estimated (Savage 1984; Shamlou 1988) as follows. Let P_v represent the average vertical pressure across the channel section, and S_w is the average shear stress at the walls across the circumference of the cross section. The shear stress is due to the friction between the walls and the particles and can be written as $S_w = P_w \tan\phi_w$, where P_w is the normal (horizontal) stress and ϕ_w is the friction angle for the particles. The ratio of the horizontal to the vertical pressure is often assumed to be a constant K independent of the vertical position, i.e., $P_w/P_v = K$. Then the force balance equation for a horizontal element with thickness of dx is

$$\frac{dP_v}{dx} = \rho_p \overline{\nu} g - \frac{KC_c \tan\phi_w}{A_c} P_v, \tag{4.10}$$

where $\overline{\nu}$ is the average solid fraction across the channel section, A_c and C_c are the area and the periphery of the cross section. Integrating Equation (4.10) with the boundary condition $P_v = 0$ at $x = 0$, then the average pressure is found:

$$P_v = \frac{\rho_p g \overline{\nu} A_c}{KC_c \tan\phi_w}\left[1 - \exp\left(-\frac{KC_c \tan\phi_w}{A_c} x\right)\right]. \tag{4.11}$$

The first derivative of P_v in the flow direction is then derived:

$$\frac{dP_v^*}{dX} = \overline{\nu} \exp\left(-\frac{KC_c \tan\phi_w}{A_c} x\right), \tag{4.12}$$

where $P_v^* = P_v/\rho_p g\sigma$. For the rectangular cross section in the present experiment, the ratio of the periphery to the area is approximated as $C_c/A_c \approx 2(2H)/w(2H) = 2/w$, where w is the depth of the channel, $w \ll 2H$. Both K and $\tan\phi_w$ are of the order of 1. Then Equation (4.12) can be approximated as

$$\frac{dP_v^*}{dX} = \overline{\nu} \exp\left(-\frac{2x}{w}\right). \tag{4.13}$$

Equation (4.13) is a reasonable estimate of dP_{xx}^*/dX in Equation (4.7). When the vertical distance x is greater than a distance of twice the channel depth $2w$, the granular pressure gradient in the flow direction dP_{xx}^*/dX in Equation (4.7) can be neglected. Then Equation (4.7) becomes

$$\frac{d}{dY}\left[g_2(\nu, e_p)\Upsilon^{*\frac{1}{2}} \frac{du_x^*}{dY}\right] + A^{\frac{3}{2}}\nu = 0. \tag{4.14}$$

Note that the distance of $2w$ is close to the top of the channel because after subtracting the length that the splitter plate extends in the test section (2 cm), the ratio of the total channel length to $(2w - 2\text{cm})$ is 42.

Richman and Marciniec (1990) presented boundary conditions for gravity-driven flows of smooth, inelastic particles down bumpy inclines, and the same theory can be applied to flows in vertical bumpy channels. The equations for the momentum and the fluctuating energy at the boundary are:

$$\boldsymbol{\Xi} = \mathbf{P} \cdot \mathbf{n} \tag{4.15}$$

and

$$\boldsymbol{\Xi} \cdot \mathbf{u} - \gamma_w = \boldsymbol{\Gamma} \cdot \mathbf{n}, \tag{4.16}$$

where $\boldsymbol{\Xi}$ is the momentum transfer rate from the boundary to the flow and $\mathbf{n}$ is a unit normal vector as shown in Figure 4.1. The fluctuating energy dissipated into the boundary is denoted by γ_w in Equation (4.16) and is proportional to $(1 - e_w)$, where e_w is the restitution coefficient for collisions between walls and the particles in the flow. Both $\boldsymbol{\Xi}$ and γ_w have been derived by Richman (1988).

Substituting for $\boldsymbol{\Xi}$ and γ_w from Richman and using Equations (4.4)–(4.6), the boundary conditions, Equations (4.15) and (4.16), at the vertical bumpy walls (Y=1) become:

$$\frac{1}{u_x^*}\frac{du_x^*}{dY} + \frac{Ag_1}{fg_2} = 0, \tag{4.17}$$

and

$$\frac{1}{\Upsilon^*}\frac{1}{g_1 A}\left[g_3 - \frac{g_1 g_4}{(dg_1/d\nu)}\right]\frac{d\Upsilon^*}{dY} - \left\{\frac{fg_2^2}{g_1^2 A\Upsilon^*}\frac{d^2u_x^*}{dY^2} - 2\left(\frac{2}{\pi}\right)^{\frac{1}{2}}(1 - e_w)(1 - \cos\phi)\csc^2\phi\right\} = 0. \tag{4.18}$$

The coefficient f in Equation (4.18) is defined by:

$$f = \frac{(\pi/2)^{\frac{1}{2}} - (g_1\overline{\sigma}/g_2\sigma)(1 + g_6\sigma/\overline{\sigma})(\sin^2\phi/2)}{\frac{2}{3}[2\csc^2\phi(1 - \cos\phi) - \cos\phi]} + \frac{g_1\overline{\sigma}}{g_2\sigma}, \tag{4.19}$$

where $\overline{\sigma} = (\sigma + \sigma_w)/2$, σ_w is the diameter of wall spheres that generate the bumpy surface condition as shown in Figure 4.1, ϕ is the angle between the vector normal to the surface and the line connecting the centers of a particle attached to the wall and a particle within the flow in the closest packed position. When the particles attached to the wall are touching and are of the same diameter as those in the flow,

the angle is 30°. The coefficient g_6 in Equation (4.19) is a function of ν and defined by

$$g_6(\nu) = \frac{\pi\left[1 + 5/(8\nu g_0)\right]}{12\sqrt{2}}. \tag{4.20}$$

As shown in Equation (4.8) for a constant coefficient of restitution at every position Y, ν is only a function of Υ^*; hence Equations (4.14) and (4.9) can be rewritten as two ordinary-differential equations for $d^2u_x^*/dY^2$ and $d^2\Upsilon^*/dY^2$ as functions of u_x^*, Υ^*, du_x^*/dY and $d\Upsilon^*/dY$. These equations are solved by a fourth-order Runge-Kutta method.

To solve these simultaneous equations, four boundary conditions are needed. Because of channel symmetry, du_x^*/dY and $d\Upsilon^*/dY$ (of course, also $d\nu/dY$) are zero at $Y = 0$. For the rough-walled channel, the boundary conditions as derived by Richman (1988), Equations (4.17) and (4.18) are employed. A "four-point shooting method" is developed to solve this boundary value problem. That is, four guessed sets of u_x^* and Υ^* at $Y = 0$ are chosen to get $(+,+)$, $(-,+)$, $(-,-)$, $(+,-)$ values of the left-hand sides of Equations (4.17) and (4.18). From the four initial sets of u_x^* and Υ^*, new sets of u_x^* and Υ^* are determined by averaging two of the sets, such as the $(+,+)$ and the $(-,+)$ sets. The averaged values of u_x^* and Υ^* are then used as the boundary conditions at $Y = 0$ for the simultaneous equations. If the integration of the simultaneous equations results in both positive values for the left-hand sides of Equations (4.17) and (4.18), then the averaged set replaces the original $(+,+)$ set, and otherwise it replaces the $(-,+)$ set. Next the $(-,+)$ and the $(-,-)$ sets are averaged and the averaged values replace either the original $(-,+)$ or $(-,-)$ set depending on the signs of the left-hand sides of Equations (4.17) and (4.18). The

process is repeated until the four sets of u_x^* and Υ^* converge to values of u_x^* and Υ^* that result in the left-hand sides of Equations (4.17) and (4.18) being less than 1×10^{-6}. Besides u_x^* and Υ^*, a guessed ν at $Y = 0$ is required to solve the equations. However, this input value of ν at $Y = 0$ is checked by comparing the calculated and experimental mass flow rates. If they are not the same, a new value ν at $Y = 0$ is input and the process is repeated.

In the present calculation, the values of the restitution coefficients $e_p = e_w = 0.95$ are used for the glass beads (Lun and Savage 1986); and the maximum shearable solid fraction ν^* is assumed to be 0.65 (Johnson and Jackson 1987). As described above, the numerical results for the roughened walls are based on the theoretical boundary conditions, and hence the profiles are determined without any additional experimental values except the mass flow rate. For the saw-tooth side walls, the boundary conditions, Equations (4.17) and (4.18) cannot be used. Instead the calculations are found by using the experimental results for u_x^* at $Y = 0$ and $Y = 1$ as inputs. By a one-point shooting method the differential equations can be solved. The value of ν at $Y = 0$ is input, and is checked by comparing the experimental and calculated value of the mass flow rates.

The calculated velocity profiles are compared with the experimental results in Figures 4.2–4.5. The experimental measurements of the velocities shown in these figures are the same as Figures 3.8(a)–3.11(a) except the profiles are not normalized by the average velocity across the channel, but plotted in the real scale, u_x^*, $u_x^* = u_x/\sqrt{gH}$.

The comparison between the calculated and the experimental results shows that

the transport relations and boundary conditions based on dense-gas kinetic theory analysis predict the velocity profiles moderately well. The calculations slightly over-predict the slip velocity along the walls and under-predict the centerline velocities. This difference may result from neglecting the frictional forces, or may be due to the underlying kinetic theory assumptions.

Figure 4.6 shows the calculated distribution in nondimensional granular temperature for the four different roughened-channel flow conditions. The figures indicate that granular temperature is conducted from the walls of the channel into the flow over a distance corresponding to approximately 50 percent of H. Richman and Marciniec (1991) employed the similar equations and boundary conditions to calculate the fully developed flow in a vertical channel. They found similar profiles of velocity and granular temperature.

From Figure 4.6, the magnitude of the granular temperature increased with the flow rate, and with a decrease in channel size. As indicated by the figure and by Equation (4.18), the gradient of the granular temperature at the wall increases as the magnitude of the granular temperature increases. The calculated variations in the granular temperature were not compared with the experimental measurements since the measurements were only for the fluctuating velocity component in the flow condition. It is interesting to note that the calculations indicate the granular temperature should be greatest at the walls. However, the measurements indicate a decrease in the fluctuating stream-wise velocity from the centerline to the channel side walls. This discrepancy can be explained as follows.

The particles in the layer closest to the wall follow the wall contour as they

flow. This movement near the wall causes a local transverse velocity although the average transverse velocity is zero. Hence the transverse velocity is equal to the local fluctuating velocity in the direction normal to the flow. As a result, the granular temperature is the greatest along the wall. For example, the particles along the saw-tooth wall move at an inclination of 60° and result in an r.m.s. transverse fluctuating velocity that is $1/\sqrt{3}$ times the average velocity. If the r.m.s. fluctuating velocity in the flow direction is 10% of the average velocity, then by the assumption of isotropic distribution of the granular temperature, the granular temperature is 0.01 times the square of the average velocity. However, if the anisotropic granular temperature distribution is considered as above, the granular temperature is about 0.2 times the square of the average velocity. This factor certainly increases the magnitude of granular temperature along the walls.

4.2 Mixing Layer Thickness

In Section 2.3.2, the self-diffusion coefficient is derived as (Equation (2.47)):

$$D_{11} = \frac{\sigma\sqrt{\pi\Upsilon}}{8(1+e_p)\nu g_0(\nu)}. \tag{4.21}$$

This expression is used to predict the mixing-layer thickness in the particle diffusion experiment described in Chapter 3. Assuming that the flow is fully developed, steady state, with no transverse bulk velocity, and neglecting diffusion in the flow direction, the diffusion equation for the mixing layer is expressed in Equation (3.1) and rewritten here:

$$u_x\frac{\partial\omega}{\partial x} = \frac{\partial}{\partial y}\left(D_{11}\frac{\partial\omega}{\partial y}\right), \tag{4.22}$$

where ω is the color concentration. Using the calculated velocity and granular temperature profiles which are numerically calculated in the last section and the theoretical self-diffusion coefficient from (4.21), Equation (4.22) is integrated by a Crank-Nicholson scheme. The boundary conditions for the flow are $\omega = 1$ when $y = H$ and $\omega = 0$ when $y = -H$; the initial conditions are at $x = 0$ and $y > 0$, $\omega = 1$, and at $x = 0$ and $y < 0$, $\omega = 0$. From the concentration profiles, the mixing-layer thickness δ is determined from the distance in which the color concentration ω varied from 0.01 to 0.99. Due to the uncertainty in the initial mixing-layer thickness, the theoretical profiles are started at $\delta/\sigma = 1$ at $x/\sigma = 0$ to compare with the experimental results as shown in Figures 4.7 and 4.8. Since only the flows in the rough-walled channel are numerically solved without any experimental measurement information (except the mass flow rate), the mixing-layer thickness profiles are only compared for these cases. The experimental curves in Figures 4.7 and 4.8 are found by curve fitting the experimental data shown in Figures 3.15 and 3.16 for the wide and the narrow channel widths. The error bars shown in the curves indicate $\pm$ one standard deviation.

The theoretical mixing-layer thickness curves indicate the right trend, but the theory under predicts the experimental results. This expression suggests that the theoretical diffusivity is lower than that of the experiments.

Although the diffusion process is not well predicted by the kinetic theory analysis for this high solid fraction, it is interesting to note that as shown in Figures 3.8 and 3.9, the dense-gas kinetic theory predicts the velocity profiles fairly well. For the momentum transport both kinetic and collisional modes contribute to the transport

relations; however, the latter is dominant when the solid fraction is large. For diffusion processes, only the kinetic mode contributes, since there is no mass exchange during a particle collision. Hence for high-solid fractions, the dense-gas kinetic theory seems to predict the collisional mode well, but not the kinetic mode. There are a number of factors that may contribute to the discrepancy. One reason for the difference is that when the solid fraction is close to that of a packed bed, the binary collision assumption used in the kinetic theory model may not be appropriate. Instead the particles slide or roll past each other, and the rotation of particles may increase the diffusion process. Another possible reason for the deviation may result from preferred collision angles between particles. The anisotropic distribution in collision may cause a non-uniform distribution in granular temperature.

Because of many underlying kinetic-theory assumptions, it seems that the theory does not predict the diffusion process well, especially when the solid fraction is so close to the maximum shearable solid fraction. The solid fractions calculated from the kinetic theory are close to 0.64. In the experiment, the solid fraction was not measured directly. From the measured mass flow rates, the average velocities across the channel, and the cross section area, the average solid fractions are found to vary from 0.59 to 0.64 in different conditions. It is interesting to predict the mixing-layer thickness qualitatively by using these approximated solid fractions without solving the momentum and the energy equations.

From the experimental measurements, the velocity and the r.m.s. fluctuating velocity distributions are relatively flat within the central half channel in which the mixing layer develops. Therefore, it is reasonable to assume the velocity and the

diffusion coefficient are constant within the mixing layer. This assumption is used in Section 3.2.2 to solve the diffusion equation and the mixing-layer thickness is found to be

$$\frac{\delta}{\sigma} = 6.60\left(\frac{x}{\sigma}\frac{1}{Pe}\right)^{\frac{1}{2}}, \tag{4.23}$$

where Pe is the Peclet number, $Pe = u_{xm}\sigma/D_{11,m}$.

The granular temperature can be estimated by assuming an isotropic distribution in fluctuating velocities. Then the granular temperature is equal to the ensemble-average of the square of the fluctuating velocities in the flow direction, $\Upsilon = {u'_x}^2 =< C_x^2 >$. From Equation (4.21), Pe is

$$Pe = \frac{u_{xm}\sigma}{D_{11,m}} = \frac{8(1+e_p)}{\sqrt{\pi}}\left(\frac{u_m}{u'_m}\right)\nu g_0(\nu). \tag{4.24}$$

From the experimental results, u'_m/u_m is close to 0.15 for all of the experiments in the rough walled channels. Two extreme values of Pe are evaluated by using $\nu = 0.59$ and $\nu = 0.64$, and $u'_m/u_m = 0.15$ in Equation (4.24). By substituting the two values of Peclet number into Equation (4.23), two mixing layer thickness are determined as shown in Figure 4.9. The experimental curves are the same as that shown in Figures 4.7 and 4.8 for both flow rates and both channel widths for the rough-walled channels. The predictive curves are started at $\delta/\sigma = 1$ to compare with the experimental results.

These curves indicate better agreement between theory and experiment. Since for the wall conditions used, the flows are anisotropic near the walls as explained in the last section which results in the discrepancy of granular temperature from the theory. The discrepancy results in the under prediction of mixing-layer thickness.

For the later prediction by using the experimental information inside the mixing layer, the discrepancy is decreased. Note that the prediction is still lower than the experimental results. The reasons have been explained earlier.

The recent study by Savage (1992) compared the kinetic-theory diffusivity with the results from a computer simulation based on molecular dynamics. Equation (2.53) was used to calculate the self-diffusion coefficients. He used Equation (2.5) as the form of the radial distribution function in the calculations of the kinetic theory. Savage found the self-diffusion coefficients determined from the simulation results were from 50% to 200% higher than those predicted by the theory. The deviation was especially large for high solid fractions. He noted that the deviation may result from the use of the isotropic radial distribution function.

4.3 Effective Thermal Conductivity

In Section 2.3.3, the effective thermal conductivity is derived by using dense-gas kinetic theory. The expression in Equation (2.70) for the effective thermal conductivity k_{eff} is rewritten:

$$k_{eff} = \frac{\rho c_p}{9\sqrt{\pi}} \frac{\sigma}{\nu g_0(\nu)} \Upsilon^{1/2}. \tag{4.25}$$

This expression is used to compare with the recent experiments by Wang and Campbell (1992) who experimentally measured the effective thermal conductivity of a granular flow. Their experiment involved an annular Couette shear cell in which the rotating surface was heated, and the stationary surface was cooled. Wang and Campbell operated their experiment for solid fractions ranging from 0.1 to 0.5,

and for four different types of particles: steel shot (σ=2.2 mm) and three sizes of glass beads (σ=1.9, 3.0 and 3.75 mm). The temperatures of the plates, and the input heat flux were measured. The effective thermal conductivity of the flow was determined by balancing the heat conducted by the flows and the heat dissipated due to the shearing process with the appropriate heat input boundary condition. In addition, force transducers were used to determine the shear force on the materials. The apparent viscosity coefficient, μ_{eff}, was calculated from the shear stress and shear rate, and then used to define the apparent Prandtl number. As shown in Figure 4.10, the apparent Prandtl number increases with solid fraction, and appears to be independent of particle type and size.

To compare with the experimental results of Wang and Campbell, the granular temperature must be known, but neither the velocities nor the granular temperature were measured in the experiment. However, the Prandtl number does not depend on granular temperature and can be more easily compared by defining an apparent viscosity based on kinetic theory results. As described in Chapter 2, the shear stress depends on both the kinetic and the collisional contributions. From Equation (2.24) or Equation (4.5), the shear stress is expressed as

$$P_{xy} = -\rho_p \sigma g_2(\nu, e_p) \Upsilon^{\frac{1}{2}} \frac{du_x}{dy}. \tag{4.26}$$

Using $-\mu_{eff}$ to denote the term preceding du_x/dy in Equation (4.26), the apparent Prandtl number is defined by

$$Pr = \frac{\mu_{eff} c_p}{k_{eff}} = 9\sqrt{\pi} g_0(\nu) g_2(\nu, e_p). \tag{4.27}$$

The curves in Figure 4.10 are plotted from Equation (4.27) using $e_p = 1$ and 0.6.

The theoretical curves over predict the results and the discrepancy increases with the solid fraction. This comparison suggests that the theoretical thermal conductivity is lower than that of the experiments for the same apparent viscosity.

The differences between the experimental results and the kinetic theory estimates may be attributed to some of the same reasons stated in the diffusion analysis. In addition, it should be noted that the height of the annulus in the experiment by Wang and Campbell was at most 5.4 cm which was from 14 to 28 particle diameters. For this finite-sized annulus, the shearing of the flow and the heat transfer near the wall may vary significantly from that in the bulk region. Near-wall variations may alter the determination of the apparent viscosity and the effective thermal conductivity. The analysis also assumes that the Biot-Fourier number for the particles is small. An estimate can be made using a heat transfer coefficient between a stationary particle and a flowing fluid. Using the collisional interval for the time (Equation (2.65)), and assuming that the square root of the r.m.s. fluctuating velocity is 15% of the bulk average velocity, the Biot-Fourier number is of the order of 0.001. Hence the small Biot-Fourier number assumption seems to be justified for the Wang and Campbell's experiments.

Chapter 5

Granular Thermal Diffusion in Granular Flows of Binary Mixtures

In Section 2.4, the governing equations and the constitutive relations for a binary mixture of granular materials are derived. Different from a single-species material, not only the pressure gradient and the number density gradient, but also the granular temperature gradient influence the diffusion process. The former effects are referred to in this work as particle diffusion (mass diffusion). The later effect is called granular thermal diffusion in this work, and is the main topic in this chapter.

The rigorous theory about the "thermal diffusion" in gases was first analyzed by Enskog and Chapman (see Chapman and Cowling 1970). The modified theory for the binary granular materials is presented in Section 2.4. Frankel (1940) and Furry (1948) elementarily explained the physical meaning of thermal diffusion. A similar explanation can be applied to the granular materials. The basic idea is that

the partial pressure gradient should be balanced by the average momentum transfer resulting from the collisions between two groups of particles as shown in Equation (2.52). In a usual case, the different-species collisions and the greatest relative velocity determine the direction of the momentum transfer. This case happens when the lighter particles coming from the region with higher granular temperature collide with the heavier particles coming from the lower granular temperature region. This kind of collision results in a net momentum transfer from the lighter particles to the heavier particles, in the opposite direction of the granular temperature gradient. From Equation (2.52), the lighter-species partial pressure increases in the opposite direction of that of the momentum transfer which is in the direction of granular temperature gradient. Since the partial pressure is increased with partial number density, this effect causes the lighter particles concentrating in the place with higher granular temperature.

This chapter considers two-dimensional (in xy-plane) flows of binary granular materials in a steady state. The gradients only exist in y-direction, since the flow is assumed to be fully developed in x-direction. From Equations (2.84) and (2.85), the governing equations can be simplified as:

$$-\frac{\partial P_{yy}}{\partial y} + \rho_\alpha F_{\alpha,y} + \rho_\beta F_{\beta,y} = 0, \tag{5.1}$$

$$-\frac{\partial P_{xy}}{\partial y} + \rho_\alpha F_{\alpha,x} + \rho_\beta F_{\beta,x} = 0, \tag{5.2}$$

and

$$-\frac{\partial \Gamma_y}{\partial y} - P_{xy}\Big(\frac{\partial u_x}{\partial y}\Big) - \gamma = 0, \tag{5.3}$$

where $F_{i,x}$ and $F_{i,y}$ are the specific external forces acting on particle i in the x and y directions. For zero bulk diffusion of particles, the diffusion velocities $\mathbf{v}_i$ are zero, and Equation (2.109) simplifies to

$$d_{\alpha,y} + k_\Upsilon \frac{\partial \ln \Upsilon}{\partial y} = 0, \tag{5.4}$$

where $d_{\alpha,y}$ is the y component of the diffusion force $\mathbf{d}_\alpha$.

As mentioned before, granular thermal diffusion is caused by a granular temperature gradient. From Equation (5.3), the conduction of granular temperature is influenced by the shear work and the energy dissipation. In order to clearly investigate the influence of the granular temperature on the diffusion process, an oscillatory system without any bulk motion of perfectly-elastic materials is first examined in Section 5.1. The more complicated systems of a sheared flow and a flow in a vertical channel are studied in the subsequent sections.

5.1 Oscillatory No-Flow System

Consider a steady system without mean motion between two parallel boundaries as shown in Figure 5.1. The body forces are neglected. The momentum equation in the x direction disappears since there is no shearing of the flow. From Equation (5.1), the only momentum equation is written as:

$$\frac{\partial P}{\partial y} = 0, \tag{5.5}$$

and using Equation (2.99), the momentum equation changes to

$$\frac{\partial}{\partial y}\left[\Upsilon\left(n + \sum_{i=\alpha,\beta}\sum_{j=\alpha,\beta}\frac{2}{3}\pi n_i n_j \sigma_{ij}^3 g_{cij}\right)\right] = 0. \tag{5.6}$$

From Equations (5.3) and (2.104), the balance equation for the fluctuating energy is

$$\frac{\partial}{\partial y}\left(\lambda\frac{\partial \Upsilon}{\partial y}\right) = 0. \tag{5.7}$$

Note that since the particles are assumed perfectly-elastic, i.e., $e_{p,ij} = 1$, the energy dissipation γ is zero.

Using Equations (2.95) and (5.5), Equation (5.4) becomes

$$\left[k_\Upsilon + \sum_{j=\alpha,\beta}\frac{n_\alpha}{n}\left(\delta_{\alpha j} + \frac{4}{3}\pi n_j \sigma_{\alpha j}^3 M_{\alpha j} g_{c\alpha j}\right)\right]\frac{\partial \ln \Upsilon}{\partial y} + \frac{n_\alpha}{m_0 n \Upsilon}\sum_{j=\alpha,\beta}\frac{\partial \mu_\alpha}{\partial n_j}\frac{\partial n_j}{\partial y} = 0. \tag{5.8}$$

The granular temperature Υ and the channel location y can be normalized by the granular temperature at $y = 0$, Υ_0, and by the channel width L, $\Upsilon^* = \Upsilon/\Upsilon_0$ and $Y = y/L$. Equations (5.6)–(5.8) can then be rewritten as four first-order ordinary differential equations for $d\nu_\alpha/dY$, $d\nu_\beta/dY$, $d\Upsilon^*/dY$ and $d^2\Upsilon^*/dY^2$. Four boundary conditions are needed to solve the equations:

$$\Upsilon^*(Y = 0) = 1, \tag{5.9}$$

$$\Upsilon^*(Y = 1) = \Upsilon_L^*, \tag{5.10}$$

$$\int_0^1 \nu_\alpha(Y)dY = \overline{\nu_\alpha}, \tag{5.11}$$

$$\int_0^1 \nu_\beta(Y)dY = \overline{\nu_\beta}. \tag{5.12}$$

As mentioned in Chapter 1, the boundary conditions in a granular flow are different from that in a fluid. Since the no-slip condition is applied in conventional fluid mechanics, the velocity and the thermodynamic temperature of the fluid at a solid boundary can be imposed. However, the boundary conditions in a granular

flow are dependent on the whole flow field, so the velocity and the granular temperature cannot be specified independently. By considering the interaction between the boundary and the flow field, Richman (1988) derived the boundary conditions for granular flows of single-species spheres moving at bumpy boundaries which was roughened by a layer of hemispherical particles. However, the boundary conditions for other kinds of surfaces are still not available in a theoretical form. For flows of binary mixtures, the boundary conditions are even more complicated. Because of this difficulty, the imposed boundary conditions as given above are employed here.

By a Runge-Kutta method, this system of equations can be solved. For the current calculations, the average solid fractions of species α and β of 0.1 and 0.25 are used, $\overline{\nu_\alpha} = 0.1$ and $\overline{\nu_\beta} = 0.25$. The dimensionless granular temperature at $Y = 1$ is chosen to be 2 for the calculations, $\Upsilon_L^* = 2$. The calculations are performed for four different sizes of α: (a) σ_α = 1-mm, (b) σ_α = 1.2-mm, (c) σ_α = 1.5-mm, (c) σ_α = 2-mm; and the particle diameters of species β are 1-mm in the four cases and the particle densities of both species are 2490 kg/m^3.

Figure 5.2 shows the solid fraction distributions for case (a) where species α and β are identical. Since the two species are identical, there is no granular thermal diffusion and then the solid fractions of both species decrease in the positive y direction in a similar ratio. To balance the momentum equation, the granular pressure is constant in the channel, so the solid fractions decrease with the increase of granular temperature; this is also indicated by the form of normal pressure for the single-species material shown in Equation (4.4). To check the numerical integration, this case is calculated by the theory of Lun et al. (1984) for the single-species material

as described in Chapter 2. The granular temperature profiles are nearly the same in the two theories. The solid fraction profiles are compared in Figure 5.2 and the difference is less than 2%. The difference is because the RET is employed in the present theory.

Figure 5.3 shows the solid fraction distributions for case (d). The figure indicates that the smaller particles (β) tend to move to the plate with higher granular temperate and that the larger particles (α) tend to move in the opposite direction. For the smaller (lighter) particles, the granular thermal diffusion causes a diffusive flux in the direction of the granular temperature gradient and results in the increase of the partial number density n_β. Due to the partial number density gradient, particle diffusion causes the smaller particles to diffuse to the opposite direction of the gradient of the partial number density, i.e., the direction in which the granular temperature decreases. Hence there is a balance between particle diffusion and granular thermal diffusion so that there is no net bulk diffusive flux. A similar diffusive balance occurs for the larger particles.

In Figure 5.4, the four curves are the granular temperature distributions for the four cases. The differences in the granular temperature profiles result from the variations in the solid fractions which are due to granular thermal diffusion.

Figure 5.5 shows the ratios of the solid fractions ν_β/ν_α in the channel for four cases in log scale. Due to the granular thermal diffusion, the ratio increases with the granular temperature. The ratio of ν_β/ν_α increases faster for higher ratio of $\sigma_\alpha/\sigma_\beta$, which indicates the larger size difference causes an increase in the granular thermal diffusion. For case (a), since there is no granular thermal diffusion, the distribution

of ν_β/ν_α is flat.

Figure 5.6 shows the ratio of ν_β/ν_α, in log scale, for the same particle diameters for both species but different particle densities. The particle density of species α is 2490 kg/m^3 but the ratios of particle densities vary for the four cases: $\rho_{p\alpha}/\rho_{p\beta} = 1$, 2, 3, 4. The case of $\rho_{p\alpha}/\rho_{p\beta} = 1$ means identical species and has been discussed above. The higher ratio of $\rho_{p\alpha}/\rho_{p\beta}$ indicates a larger mass difference, which results in more granular thermal diffusion; hence the ratio of ν_β/ν_α increases faster.

When the difference in size or mass of the two species is increased or the granular temperature gradient is increased, transport due to granular thermal diffusion becomes more significant. If any factor is large enough, the two species can be completely segregated. One example is shown in Figure 5.7 plotted for the solid fraction distributions for the case of $\Upsilon_L^* = 3$, $\sigma_\alpha/\sigma_\beta = 2$, and $\rho_{p\alpha}/\rho_{p\beta} = 4$.

5.2 Sheared Granular Flows

In this section, a steady and fully developed sheared flow of a binary mixture between two parallel boundaries is studied. The configuration of this system is shown in Figure 5.8. The external forces are neglected. The momentum equation in y direction and the equation for zero diffusion velocity remain the same as Equations (5.5) or (5.6) and (5.8) for the oscillatory no-flow system. From Equations (5.2) and (2.100), the momentum equation in x-direction is written as:

$$\frac{\partial}{\partial y}\left(\mu \frac{\partial u_x}{\partial y}\right) = 0. \tag{5.13}$$

From Equations (5.3), (2.104) and (2.100), the conservation equation for the energy is

$$\frac{\partial}{\partial y}\Big(\lambda\frac{\partial \Upsilon}{\partial y}\Big) + \mu\Big(\frac{\partial u_x}{\partial y}\Big)^2 = \gamma. \tag{5.14}$$

The first term in Equation (5.14) is the fluctuating energy added to the system by the conduction of the granular temperature and the second term is the shear work done to the system. The sum of these two terms is equal to the energy dissipation due to the inelastic collisions. Equation (5.14) can be nondimensionalized to

$$\frac{\partial}{\partial Y}\Big(\lambda^*\frac{\partial \Upsilon^*}{\partial Y}\Big) + R_1^2 R_2^2 \mu^*\Big(\frac{\partial u_x^*}{\partial Y}\Big)^2 = R_2^2\gamma^*. \tag{5.15}$$

The dimensionless variables Υ^*, u_x^*, λ^*, μ^* and γ^* are defined as $\Upsilon^* = \Upsilon/\Upsilon_0$, $u_x^* = (u_x - u_{x0})/(u_{xL} - u_{x0}) = (u_x - u_{x0})/\Delta u_x$, $\lambda^* = \lambda/(\Upsilon_0^{1/2}\rho_{p\beta}\sigma_\beta)$, $\mu^* = \mu/(\Upsilon_0^{1/2}\rho_{p\beta}\sigma_\beta)$, $\gamma^* = \gamma\sigma_\beta/(\Upsilon_0^{3/2}\rho_{p\beta})$ and $Y = y/L$, where Υ_0 and u_{x0} is the granular temperature and the velocity at $y = 0$, u_{xL} is the velocity at $y = L$, and L is the channel width. The dimensionless parameter R_1 is defined by

$$R_1 = \frac{\sigma_\beta(\Delta u_x/L)}{\Upsilon_0^{\frac{1}{2}}}, \tag{5.16}$$

and R_2 is the ratio of the channel width to the smaller particle diameter, $R_2 = L/\sigma_\beta$.

Equations (5.6), (5.13), (5.15) and (5.8) can then be rewritten as six first-order ordinary differential equations for $d\nu_\alpha/dY$, $d\nu_\beta/dY$, $d\Upsilon^*/dY$, $d^2\Upsilon^*/dY^2$, du_x^*/dY and $d^2u_x^*/dY^2$. Six boundary conditions are used to solve the equations. The first four boundary conditions are the same as that used in the oscillatory no-flow system and the other two are

$$u_x^*(Y = 0) = 0, \tag{5.17}$$

and

$$u_x^*(Y = 1) = 1. \tag{5.18}$$

As discussed in the last section, the boundary conditions for the sheared granular flows should be determined by the whole flow field. However, due to the lack of information regarding boundary conditions for binary-mixture flows, the imposed boundary conditions are used.

The Runge-Kutta method is employed to solve these equations. Due to the effect of granular thermal diffusion, the solid fraction of the smaller or the lighter particles (β) is found to increase with the positive gradient of granular temperature and to decrease when the granular temperature decreases. The only exception occurs when the solid fraction of the larger or the heavier species is close to 0; in order to maintain the constant mixture pressure, the solid fraction of the smaller (lighter) particles has to decrease with the increase of granular temperature.

In the current calculations, σ_α = 2-mm, σ_β = 1-mm, $\rho_{p\alpha} = \rho_{p\beta} = 2490$ kg/m^3, $e_{p,ij} = 0.95$ and $R_2 = 20$ are used. According to the computer simulation result for simple shear flows of a granular material by Campbell (1989), the parameter of $(\sigma_i du_x/dy)/\Upsilon_i^{1/2}$ ranges from 0 to 1. The present calculation uses R_1 from 2 to 3 so that $(\sigma_i du_x/dy)/\Upsilon_i^{1/2}$ for both species is within this range anywhere in the channel. The total solid fractions $\overline{\nu}$ are chosen between 0.3 and 0.45. Three different cases are studied that result in three very different profiles of the solid fraction distributions and the granular temperature distributions. The three typical cases are explained as follows.

Figure 5.9 is the granular temperature and solid fraction distribution for $\Upsilon_L^* = 10$,

$\overline{\nu_\alpha} = 0.03$, $\overline{\nu_\beta} = 0.28$, and $R_1 = 2.9$. The second derivative of granular temperature is always positive in the channel indicating that the fluctuating energy is added to the system everywhere, i.e., the energy dissipation is greater than the shear work done to the system. The ratio of ν_β/ν_α is increasing with the granular temperature resulting from the granular thermal diffusion similar to the oscillatory no-flow system. Note that the first derivative of granular temperature at $Y = 0$ is positive.

Figure 5.10 shows the distributions of granular temperature and solid fraction for $\Upsilon_L^* = 15$, $\overline{\nu_\alpha} = 0.08$, $\overline{\nu_\beta} = 0.25$, and $R_1 = 2.5$. The second derivative of granular temperature is positive similar to the last case. It indicates that the energy dissipation is larger than the shear work so that the fluctuating energy has to be conducted into the system. The first derivative at $Y = 0$ is negative causing the granular temperature to decrease until a certain position ($Y = 0.068$ in this case) where the first derivative of granular temperature starts to change sign. The corresponding solid fraction of the smaller particles shows the same trend as the granular temperature before $Y = 0.272$. Since the large particle solid fraction after this position is relatively small, the smaller particle solid fraction decreases with the increase of granular temperature to maintain the constant pressure.

Figure 5.11 is for the third case of $\Upsilon_L^* = 1.15$, $\overline{\nu_\alpha} = 0.07$, $\overline{\nu_\beta} = 0.35$, and $R_1 = 2.2$. The second derivative of granular temperature is negative in the channel indicating that the energy dissipation is smaller than the shear work done to the system. Hence the fluctuating energy is conducted from the system. The solid fractions and the granular temperature are relatively flat in the center of the channel.

Note that in the first two cases, the granular thermal diffusion causes segregation

of the two species of particles. By contrast, in the last case, there is not a complete segregation of the particles.

Figure 5.12 shows the velocity distributions for these three cases of shear flow. The shear rate in the beginning of the channel for the third case is the largest and the granular temperature in this case is relatively small ($\Upsilon_L^* = 1.15$). Hence the shear work is higher than the energy dissipation resulting in the negative second derivative of the granular temperature.

In the literature, a shear flow with constant granular temperature, constant solid fractions and constant shear rate is called a simple shear flow. Since no granular temperature gradient exists in these flows, there is no granular thermal diffusion effect. Most studies about binary mixtures only discuss simple shear flows. Jenkins and Mancini (1989) assumed a simple shear flow to predict shear stress for a binary particle mixture. They compared with the numerical results from Farrell et al. (1986) and the computer simulation results from Walton (1989). The current numerical integration is checked with Jenkins and Mancini's result using the same assumptions; no difference is found between the two calculations.

5.3 Flow in a Vertical Channel

A granular flow of a binary mixture in a vertical channel is discussed in this section. As shown in Figure 5.13, the flow is two-dimensional, steady state and fully developed. The momentum equation in y-direction and the zero diffusion velocity equation are the same as Equations (5.6) and (5.8) for the last two systems. Then

from Equations (5.2) and (2.100), the momentum equation in the flow direction is

$$\frac{\partial}{\partial y}\left(\mu\frac{\partial u_x}{\partial y}\right) + \rho g = 0. \tag{5.19}$$

The conservation equation of the energy remains the same as Equation (5.14) for the sheared flow. By using the dimensionless variables similar to that defined in Section 4.1, $u_x^* = u_x/\sqrt{gH}$, $\Upsilon^* = \Upsilon/g\sigma_\beta$, $\mu^* = \mu/(\rho_{p\beta}g^{1/2}\sigma_\beta^{3/2})$, $\lambda^* = \lambda/(\rho_{p\beta}g^{1/2}\sigma_\beta^{3/2})$, $\gamma^* = \gamma/(\rho_{p\beta}g^{3/2}\sigma_\beta^{1/2})$ and $Y = y/H$, where H is the half-channel width, the x-momentum equation and the fluctuating energy equation change to

$$\frac{\partial}{\partial Y}\left(\mu^*\frac{\partial u_x^*}{\partial Y}\right) + A^{\frac{3}{2}}\left(\frac{\rho_{p\alpha}}{\rho_{p\beta}}\nu_\alpha + \nu_\beta\right) = 0, \tag{5.20}$$

and

$$\frac{\partial}{\partial Y}\left(\lambda^*\frac{\partial \Upsilon^*}{\partial Y}\right) + A\mu^*\left(\frac{\partial u_x^*}{\partial Y}\right)^2 = A^2\gamma^*, \tag{5.21}$$

where $A = H/\sigma_\beta$.

The four equations can be written as six first-order ordinary differential equations for $d\nu_\alpha/dY$, $d\nu_\beta/dY$, $d\Upsilon^*/dY$, $d^2\Upsilon^*/dY^2$, du_x^*/dY and $d^2u_x^*/dY^2$. Six boundary conditions are needed to solve the equations. Because of the symmetry of the channel, the first two boundary conditions are:

$$\frac{du_x^*}{dY}(Y=0) = 0, \tag{5.22}$$

$$\frac{d\Upsilon^*}{dY}(Y=0) = 0. \tag{5.23}$$

The third and the fourth boundary conditions are for the mass flow rates:

$$2\rho_{p\alpha}w\int_0^H \nu_\alpha u_x(y)dy = \dot{m}_\alpha, \tag{5.24}$$

$$2\rho_{p\beta}w\int_0^H \nu_\beta u_x(y)dy = \dot{m}_\beta, \tag{5.25}$$

where w is the channel depth. These two conditions can be changed to the form of matching the total mass flow rate, $\dot{m}_0 = \dot{m}_\alpha + \dot{m}_\beta$, and the mass flow rate ratio, $\dot{m}_\alpha/\dot{m}_\beta$. Suppose that the flow is completely segregated along the walls and only smaller particles (β) exist close to the walls. If the wall surface is made by attaching a layer of touching particles of species β, the boundary conditions proposed by Richman and Marciniec (1990) for gravity-driven flows of identical particles can be used. The equations are shown in Equations (4.17) and (4.18). Note that all the parameters and variables in Equations (4.17) and (4.18) are for the smaller particles including the granular temperature ($\Upsilon_\beta = m_0\Upsilon/m_\beta$). The Runge-Kutta method can be employed to solve the equations.

There are two difficulties in employing the above analysis. First, when a well-mixed flow enters the channel, the diffusion process continues in the channel and changes the solid fractions of the two species. The flow may take a long distance to develop. If the solid fraction profiles are not fully developed, the above analysis cannot be applied.

The second problem is about the equilibrium radial distribution function. Reed and Gubbins (1973) compared the Carnahan-Starling approximation (see Equation (2.96)) with the molecular-dynamics results for solid fractions smaller than 0.5 and showed an exact agreement. Only a 2% error is found when solid fraction is 0.55. For solid fraction higher than this value, the deviation becomes significant and the Carnahan-Starling approximation fails.

The experiment discussed in Chapter 3 suggests that the solid fraction of a steady flow in a vertical channel ranges from 0.59 to 0.64. So the radial distribution function given by Carnahan and Starling for the single-species (Equation (2.5)) which is not valid for high solid fraction is not used in the calculations in Chapter 4. However, the form is used by Richman and Marciniec (1991) to predict the single-species flows in a vertical channel. Although their calculated profiles of velocity, granular temperature, and solid fraction show the right trend, the overall solid fractions are too small (ranging from 0.1 to 0.4). Because of the gravity, the particles accelerate down the channel without colliding with each other when the solid fraction is low. In this condition, the kinetic theory breaks down.

Appendix A contains the calculations by assuming the flow is fully developed and using the equilibrium radial distribution function for a binary-mixture from the Carnahan-Starling approximation. Similar problems to those encountered by Richman and Marciniec (1991) occur. Therefore, a better form of the equilibrium radial distribution function for high solid fractions is needed to solve for flows in a vertical channel.

Chapter 6

Concluding Remarks

The current experiment is designed to investigate the diffusion of particles that occurs when a granular material flow is sheared in a vertical channel. Two differently-colored but otherwise-identical particle streams were mixed in the channel. In the experiments, a range of flow conditions were investigated by varying the side wall conditions, the flow rates, the wall spacing and the particle sizes.

Fibre optic probes were employed to measure the velocities and the longitudinal r.m.s. fluctuating velocities in different channel locations. The measured velocity profiles indicate a shear region near the wall of about 3–4 particle diameters in thickness, and a slip velocity that ranges from 25 to 60% of the average velocity depending on the wall conditions. The longitudinal velocity fluctuations range from 10 to 16% of the average value, and increase with the overall flow rate.

The frame grabber and image processing technique was used to measure the mixing layer thickness. The diffusion measurements show that the mixing layer thickness

increases as the square-root of the downstream distance, and appears to depend on the magnitude of the fluctuating velocity as compared to the average velocity. The particle diffusion occurs within the central region of the flow in which the velocity measurements do not indicate any shearing of the material, though visual observations suggest some transverse movement of the particles. The experiments do not include the fluctuating velocity in the direction transverse to the flow. These measurements are the subject of future work and important in determining the granular temperature.

The dense-gas kinetic theory is employed to analyze granular flows. Based on the constitutive theory developed by Lun et al. (1984) and the boundary conditions for the bumpy walls derived by Richman and Marciniec (1990), the fully developed velocity profiles and granular temperature profiles in a vertical channel are determined. The calculated velocity profiles are compared with the experimental results. The correspondences between the experiments and the calculations is surprisingly good considering the transport equations do not include frictional forces, and are based on the kinetic theory idealizations such as an isotropic granular-temperature distribution.

Using the dense-gas kinetic theory, the constitutive relations for the flow-induced particle diffusion coefficient and the effective thermal conductivity are developed. These transport coefficients are shown to depend on the square-root of the granular temperature, the particle sizes, the solid fraction, and the radial distribution

function. The coefficients are used to estimate transport rates in the current diffusion experiment and the heat transfer experiment performed by Wang and Campbell (1992). The comparisons demonstrate that the dense-gas kinetic theory analysis is valuable for developing a functional dependence for the various flow properties; however, both coefficients derived from kinetic theory are lower than those found from the experimental measurements. Several reasons are suggested for the discrepancy: the binary collision model, the uniform distribution of particle collisions, and the isotropic distribution of granular temperature as assumed in the kinetic theory model.

Jenkins and Mancini (1989) extended the revised Enskog theory to binary mixtures of smooth, nearly elastic granular material. Their results are used to study the granular thermal diffusion phenomena in an oscillatory no-flow system, in a sheared flow and in a flow in a vertical channel. Due to the granular thermal diffusion, the lighter (smaller) particles tend to move to the place with higher granular temperature, and the heavier (larger) particles tend to move in the opposite direction. The granular thermal diffusion is more significant when the difference in sizes or masses of the two species is increased or the granular temperature gradient is increased. The species may be segregated due to this effect. Future work should focus in the experimental study of the granular thermal diffusion and segregation. The boundary conditions for this subject are not clear, so the imposed conditions are used for the oscillatory no-flow system and the sheared flow. A better understanding of the boundary conditions is necessary and should be focused on in the future.

Bibliography

[1] Ahn, H. 1989 Experimental and analytical investigations of granular materials: shear flow and convective heat transfer. Ph.D. Thesis, California Institute of Technology.

[2] Ahn, H., Brennen, C.E. and Sabersky, R.H. 1991 Measurements of velocity, velocity fluctuation, density, and stresses in chute flows of granular materials. *J. Appl. Mech.* **58**, 792–803.

[3] Ahn, H., Brennen, C.E. and Sabersky, R.H. 1992 Analysis of fully developed chute flow of granular materials. *J. Appl. Mech.* **59**, 109–119.

[4] Augenstein, D.A. and Hogg. R. 1974 Friction factors for powder flow. *Powder Technology* **10**, 43–49.

[5] Augenstein, D.A. and Hogg. R. 1978 An experimental study of the flow of dry powders over inclined surfaces. *Powder Technology* **19**, 205–215.

[6] Bagnold, R.A. 1954 Experiments on a gravity-free dispersion of large solid particles in a Newtonian fluid under shear. *Proc. R. Soc. Lond. A* **225**, 49–63.

[7] Bailard, J. 1978 An experimental study of granular-fluid flow. Ph.D Thesis, University of California, San Diego.

[8] Barajas, L., García-Colín and Piña, E. 1973 On the Enskog-Throne theory for a binary mixture of dissimilar rigid spheres. *J. Stat. Phys.* **7**, 161–183.

[9] van Beijeren, H. and Ernst, M.H. 1973 The modified Enskog equation. *Physica* **68**, 437–456.

[10] Bridgwater, J., Foo, W.S. and Stephens, D.J. 1985 Particle mixing and segregation in failure zones — theory and experiment. *Powder Technology* **41**, 147–158.

[11] Campbell, C.S. 1988 Boundary interactions for two-dimensional granular flows: asymmetric stresses and couple stresses. In *Micromechanics of Granular Materials*, ed. M. Satake and J.T. Jenkins, Elsevier Science Publisher, Amsterdam, 163–174.

[12] Campbell, C.S. 1989 The stress tensor for simple shear flows of a granular material. *J. Fluid Mech.* **203**, 449–473.

[13] Campbell, C.S. 1990 Rapid granular flows. *Annu. Rev. Fluid Mech.* **22**, 57–92.

[14] Campbell, C.S. and Brennen, C.E. 1985a Computer simulation of granular shear flows. *J. Fluid Mech.* **151**, 167–188.

[15] Campbell, C.S. and Brennen, C.E. 1985b Chute flows of granular material: some computer simulations. *J. Appl. Mech.* **52**, 172–178.

[16] Campbell, C.S. and Gong, A. 1986 The stress tensor in a two-dimensional granular shear flow. *J. Fluid Mech.* **164**, 107–125.

[17] Campbell, C.S. and Gong, A. 1987 Boundary conditions for two-dimensional granular flow. *Proceedings of the International Symposium on Multiphase Flows, Hangzhou China,* **1**, 278–283.

[18] Carnahan, N.F. and Starling, K.E. 1969 Equations of state for non-attracting rigid spheres. *J. Chem. Phys.* **51**, 635–636.

[19] Chapman, S. and Cowling, T.G. 1970 *The Mathematical Theory of Non-Uniform Gases*, 3rd edn. Cambridge University Press, Cambridge.

[20] Clump, C.W. 1967 Mixing of solids. *Mixing 2*, Academic Press, New York and London, ch. 10, 263–286.

[21] Farrell, M., Lun, C.K.K. and Savage, S.B. 1986 A simple kinetic theory for granular flow of binary mixtures of smooth, inelastic, spherical particles. *Acta Mechanica* **63**, 45–60.

[22] Ferron, J.R. and Singh, D.K. 1991 Rotary kiln transport processes. *AIChE J.* **37**, 747–758.

[23] Frankel, S.P. 1940 Elementary derivation of thermal diffusion. *Phys. Rev.* **57**, 661.

[24] Furry, W.H. 1948 On the elementary explanation of diffusion phenomena in gases. *Amer. J. Phys.* **16**, 63–78.

[25] Hanes, D.M. and Inman, D.L. 1985 Observations of rapidly flowing granular-fluid flow. *J. Fluid Mech.* **150**, 357–380.

[26] Hopfinger, E.J. 1983 Snow avalanche motion and related phenomena. *Annu. Rev. Fluid Mech.* **15**, 47–76.

[27] Hsu, K.J. 1975 Catastrophic debris streams generated by rock falls. *Amer. Bull.* **86**, 129–140.

[28] Hunt, M.L. and Hsiau, S.S. 1990, Thermal conductivity of granular flows. *Heat Transfer 5*, ed. G. Hetsroni, Hemisphere Publishing Co., 177–182.

[29] Ishida, M. and Shirai, T. 1979 Velocity distributions in flow of solid particles in an inclined open channel. *J. Chem. Eng. Jpn.* **12**, 46–50.

[30] Jenkins J.T. and Mancini, F. 1987 Balance laws and constitutive relations for plane flows of a dense, binary mixture of smooth, nearly elastic, circular disks. *J. Appl. Mech.* **54**, 27–34.

[31] Jenkins J.T. and Mancini, F. 1989 Kinetic theory for binary mixtures of smooth, nearly elastic spheres. *Phys. Fluids A* **1**, 2050–2057.

[32] Jenkins, J.T. and Richman, M.W. 1985 Kinetic theory for plane flows of a dense gas of identical, rough, inelastic, circular disks. *Phys. Fluids* **28**, 3485–3494.

[33] Jenkins, J.T. and Richman, M.W. 1986 Boundary conditions for plane flows of smooth, nearly elastic, circular disks. *J. Fluid Mech.* **171**, 53–69.

[34] Jenkins, J.T. and Savage, S.B. 1983 A theory for the rapid flow of identical, smooth, nearly elastic spherical particles. *J. Fluid Mech.* **130**, 187–202.

[35] Johanson, J.R. 1978 Particle segregation ... and what to do about it. *Chemical Engineering May 8*, 183–188.

[36] Johnson, P.C. and Jackson, R. 1987 Frictional-collisional constitutive relations for granular materials, with application to plane shearing. *J. Fluid Mech.* **176**, 67–93.

[37] Johnson, P.C., Nott, P and Jackson, R. 1990 Frictional-collisional equations of motion for particulate flows and their application to chutes. *J. Fluid Mech.* **210**, 501–535.

[38] Kennard, E.H. 1938 *Kinetic Theory of Gases*, McGraw-Hill, New York.

[39] Kim, H. and Rosato, A.D. 1992 Particle simulations of the flow of smooth spheres between bumpy boundaries. In *Advances in Micromechanics of Granular Materials*, ed. H.H. Shen, et al., Elsevier Science Publishers, Amsterdam, 91–100.

[40] Kincaid, J.M., López de Haro, M. and Cohen, E.G.D. 1983 The Enskog theory for multicomponent mixtures. II. Mutual diffusion. *J. Chem. Phys.* **79**, 4509–4521.

[41] Kunii, D. 1980 Chemical reaction engineering and research and development of gas solid system. *Chemical Engineering Science* **35**, 1887–1911.

[42] Longwell, C.R., Knoph, A. and Flint, R.F. 1948 *Physical Geology*, Wiley, New York.

[43] López de Haro, M., Cohen, E.G.D. and Kincaid, J.M. 1983 The Enskog theory for multicomponent mixtures. I. Linear transport theory. *J. Chem. Phys.* **78**, 2746–2759.

[44] Louge, M.Y., Jenkins, J.T. and Hopkins, M.A. 1990 Computer simulations of rapid granular shear flows between parallel bumpy boundaries. *Phys. Fluids A* **2**, 1042–1044.

[45] Lun, C.K.K. 1991 Kinetic theory for granular flow of dense, slightly inelastic, slightly rough spheres. *J. Fluid Mech.* **233**, 539–559.

[46] Lun, C.K.K. and Savage, S.B. 1986 The effects of impact velocity dependent coefficient of restitution on stresses developed by sheared granular materials. *Acta Mechanica* **63**, 15–44.

[47] Lun, C.K.K. and Savage, S.B. 1987 A simple kinetic theory for granular flow of rough, inelastic, spherical particles. *J. Appl. Mech.* **54**, 47–53.

[48] Lun, C.K.K., Savage, S.B., Jeffrey, D.J. and Chepurniy, N. 1984 Kinetic theories for granular flow: inelastic particles in couette flow and slightly inelastic particles in a general flowfield. *J. Fluid Mech.* **140**, 223–256.

[49] Mansoori, G.A., Carnahan, N.F., Starling, K.E. and Leland, T.W., Jr. 1971 Equilibrium thermodynamic properties of the mixture of hard spheres. *J. Chem. Phys.* **54**, 1523–1525.

[50] McQuarrie, D.A. 1976 *Statistical Mechanics*, Harper and Row, New York.

[51] Middleton, G.V. and Hampton, M.A. 1976 Subaqueous sediment transport and deposition by sediment gravity flows. In *Marine Sediment Transport and Environmental Management*, ed. D.J. Stanley and D.J.P. Swift, Wiley, New York, 197–218.

[52] Nedderman, R.M. and Loahakul, C. 1980 The thickness of the shear zone of flowing granular materials. *Powder Technology* **25**, 91–100.

[53] Ogawa, S. 1978 Multi-temperature theory of granular materials. *Proc. U.S.-Japan. Seminar on Continuum-Mechanical and Statistical Approaches in the Mechanics of Granular Materials*, 208–217.

[54] Patton, J.S., Sabersky, R.H. and Brennen, C.E. 1986 Convective heat transfer to rapidly flowing, granular Materials. *Int. J. Heat Mass Transfer* **29**, 1263–1269.

[55] Patton, J.S., Sabersky, R.H. and Brennen, C.E. 1987 Shear flows of rapidly flowing granular materials. *J. Appl. Mech.* **54**, 801–805.

[56] Present, R.D. 1958 *Kinetic Theory of Gases*, McGraw-Hill, New York.

[57] Reed, T.M. and Gubbins, K.E. 1973 *Applied Statistical Mechanics*, McGraw-Hill, New York.

[58] Reif, F. 1965 *Fundamentals of Statistical and Thermal Physics*, McGraw-Hill, New York.

[59] Richard, P. and Raghavan, G.S.V. 1984 Drying and processing by immersion in a heated particulate medium. In *Advances in Drying* **3**, ed. A.S. Mujumdar, Hemisphere Publishing, 39–70.

[60] Richman, M.W. 1988 Boundary conditions based upon a modified Maxwellian velocity distribution for flows of identical, smooth, nearly elastic spheres. *Acta Mechanica* **75**, 227–240.

[61] Richman, M.W. and Marciniec, R.P. 1990 Gravity-driven granular flows of smooth, inelastic spheres down bumpy inclines. *J. Appl. Mech.* **112**, 1036–1043.

[62] Richman, M.W. and Marciniec, R.P. 1991 Granular chute flows. *Recent Advances in Mechanics of Structured Continua* **117**, 75–80.

[63] Ridgway, K. and Rupp, R. 1970 Flow of granular materials down chutes. *Chem. Process Eng.* **51**, 82–85.

[64] Roberts, A.W. 1969 An investigation of the gravity flow of noncohesive granular materials through discharge chutes. *ASME Trans., J. Eng. Ind.* **91**, 373–381.

[65] Savage, S.B. 1979 Gravity flow of cohesionless granular materials in chutes and channels. *J. Fluid Mech.* **92**, 53–96.

[66] Savage, S.B. 1984 Mechanics of rapid granular flows. *Adv. Appl. Mech.* **24**, 298–366.

[67] Savage, S.B. 1987 Interparticle percolation and segregation in granular materials : a review. In *Developments in Engineering Mechanics*, ed. A.P.S. Selvadurai, Elsevier Science Publisher, Amsterdam, 347–363.

[68] Savage, S.B. 1992 Disorder, diffusion and structure formation in granular flows. In *Disorder and Granular Media,* ed. D. Bideau, Elsevier Science Publishers, Amsterdam.

[69] Savage, S.B. and Jeffrey, D.J. 1981 The stress tensor in a granular flow at high shear rates. *J. Fluid Mech.* **110**, 255–272.

[70] Savage, S.B. and Lun, C.K.K. 1988 Particle size segregation in inclined chute flow of dry cohesionless granular solids. *J. Fluid Mech.* **189**, 311–335.

[71] Savage, S.B. and McKeown, S. 1983 Shear stress developed during rapid shear of dense concentrations of large spherical particles between concentric cylinders. *J. Fluid Mech.* **127**, 453–472.

[72] Savage, S.B. and Sayed, M. 1984 Stresses developed by dry cohesionless granular materials sheared in an annular shear cell. *J. Fluid Mech.* **142**, 391–430.

[73] Shamlou, P.A. 1988 *Handling of Bulk Solids*, Butterworth, London.

[74] Shen, H.H. 1984 Stresses in a rapid flow of spherical solids with two sizes. *Int. J. Part. Sci. and Tech.* **2**(1), 37–56.

[75] Stephens, D.J. and Bridgwater, J. 1978 The mixing and segregation of cohesionless particulate materials. Part I. Failure zone formation. *Powder Technology* **21**, 17–28.

[76] Sullivan, W.N. and Sabersky, R.H. 1975 Heat transfer to flowing granular media. *Int. J. Heat Mass Transfer* **18**, 97–107.

[77] Sun, J. and Chen, M.M. 1988 A theoretical analysis of heat transfer due to particle impact. *Int. J. Heat Mass Transfer* **31**, 969–975.

[78] Takahashi, H. and Yanai, H. 1973 Flow profiles and void fraction of granular solids in a moving bed. *Powder Technology* **7**, 205–214.

[79] Walton, O.R. 1984 Computer simulation of particulate flow. *Energy Technology Rev. 1984 (May)*, Lawrence Livemore Lab., 24–36.

[80] Walton, O.R. 1986 Discrete particle computer methods for modelling granular flow. In *Advancements in Aerodynamics, Fluid Mechanics and Hydraulics*, ed. R.E.A. Arndt, et al., New York: ASME, 264–273.

[81] Walton, O.R. 1989 Granular flow: numerical simulation of dry granular flows and calculation of hydrodynamic interactions in suspensions. In *Proceedings of the DOE/NSF Workshop on Fluid-Solids Transport,* Pleasanton, California, May 1989 (POE Energy Technology Center, Pittsburgh, 1989).

[82] Walton, O.R. 1992 Numerical simulation of inclined chute flows of monodisperse, inelastic, frictional spheres. In *Advances in Micromechanics of Granular Materials*, ed. H.H. Shen, et al., Elsevier Science Publishers, Amsterdam, 453–461.

[83] Walton, O.R. and Braun, R.L. 1986a Viscosity and temperature calculations for shearing assemblies of inelastic, frictional disks. *J. Rheology* **30**, 949–980.

[84] Walton, O.R. and Braun, R.L. 1986b Stress calculations for assemblies of inelastic spheres in uniform shear. *Acta Mechanica* **63**, 73–86.

[85] Walton, O.R., Braun, R.L., Mallon, R.G. and Cervelli, D.M. 1988 Particle-dynamics calculations of gravity flow of inelastic, frictional spheres. In *Micromechanics of Granular Materials*, ed. M. Satake and J.T. Jenkins, Elsevier Science Publishers, Amsterdam, 153–162.

[86] Wang, D.G. and Campbell, C.S. 1992 Reynolds' analogy for particle flows: the relationship between the apparent thermal conductivity and viscosity for a sheared granular material. Accepted for publication in *J. Fluid Mech.*

Appendix A

Numerical Calculations of Granular Flows in a Vertical Channel

The equations and the boundary conditions described in Section 5.3 are solved by a Runge-Kutta method. The vertical channel size is chosen to be the same as the experiment discussed in Chapter 3: $w = 2.18$ cm, $2H = 3.81$ cm. The particle diameters are 4-mm and 2-mm and the particle densities are 2490 kg/m^3. The restitution coefficients of the collisions between the particles and between the wall and the particles are 0.95, $e_{p,ij} = e_w = 0.95$.

Figures A.1–A.3 are the solid fraction distribution profiles for three different total flow rates: (a) $\dot{m}_0 = 2.20$ kg/sec, (b) $\dot{m}_0 = 2.00$ kg/sec and (c) $\dot{m}_0 = 1.68$ kg/sec; and the mass flow ratios $\dot{m}_\alpha/\dot{m}_\beta$ are 1 for the three cases. The solid fraction distributions are similar to that of the first typical case for the shear flow shown in Figure 5.9. The granular temperature distributions for the three flow rates are shown in Figure A.4.

The granular temperature continues to increase from the center of the channel to the wall, and the gradient causes the granular thermal diffusion and the segregation of the two species. The distributions of ν_β/ν_α are shown in Figure A.5 in log scale. For higher flow rate, the granular thermal diffusion effect seems more significant.

The velocity profiles for the three cases are shown in Figure A.6. In the central region, the profiles are relatively flat. It is interesting that for higher flow rate, the velocity becomes lower and the corresponding solid fractions are higher. It is different from the results shown in Chapter 4. Mathematically it is correct; however, physically it is impossible since the solid fractions are too low to maintain a steady flow without acceleration. Note that the velocities and the flow rates in the experiment discussed in Chapter 3 are of the order of 0.1 m/sec and 0.1 kg/sec; however, for the same size of channel, the velocities and the flow rates of the current calculations are of the order of 1 m/sec and 1 kg/sec which are the same order as Richman and Marciniec's (1991) calculations.

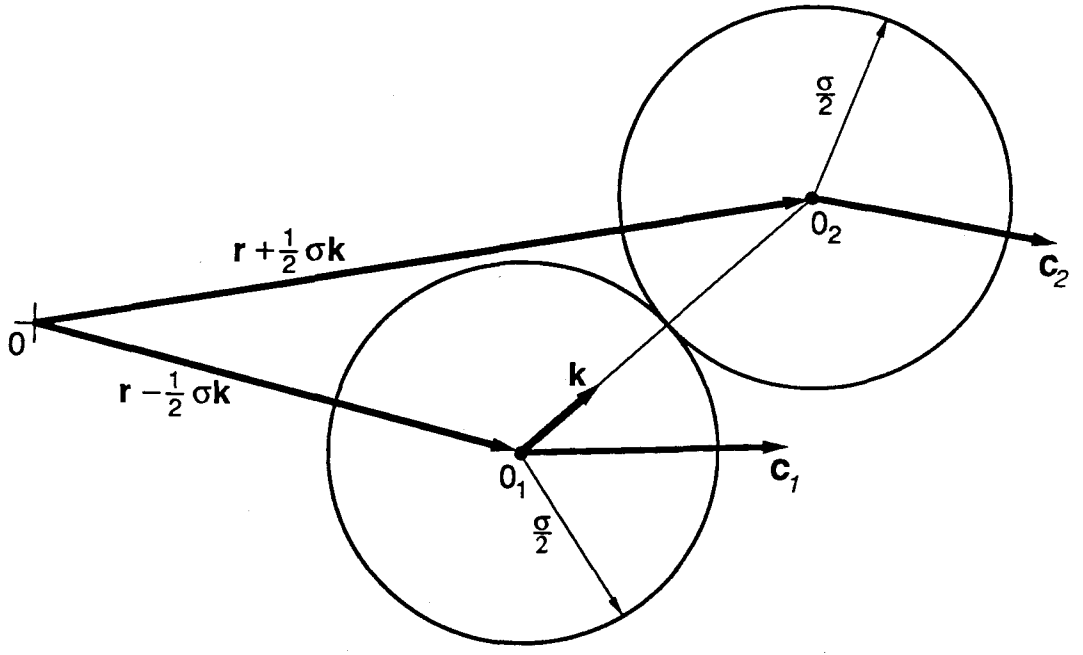

Figure 2.1: The collision of two identical particles.

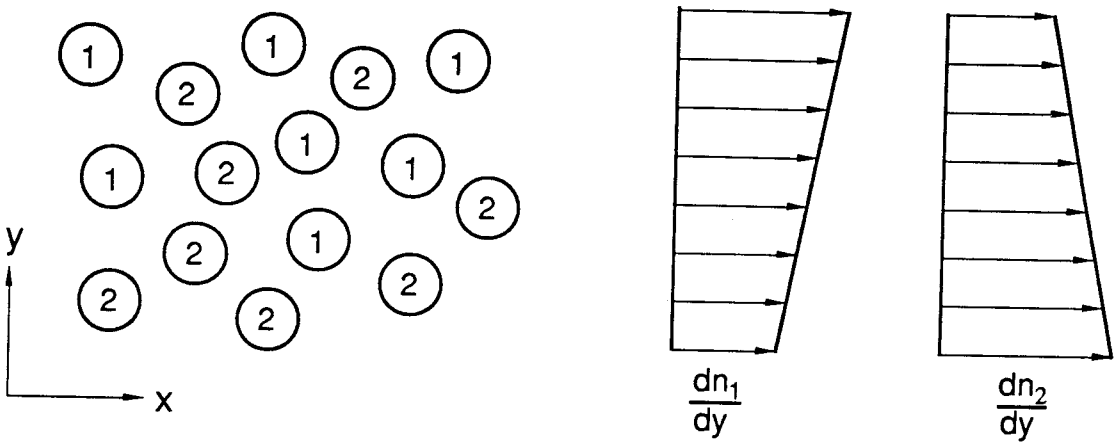

Figure 2.2: Configuration for the concentration gradient.

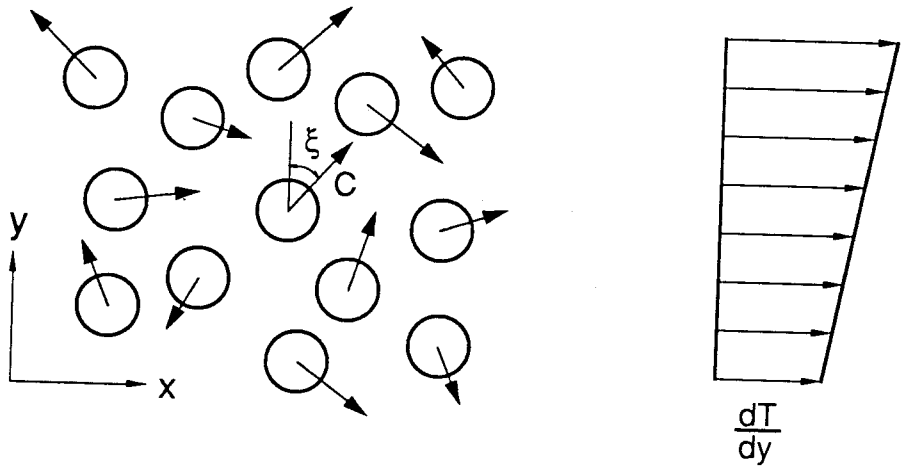

Figure 2.3: Configuration for the thermal energy flux.

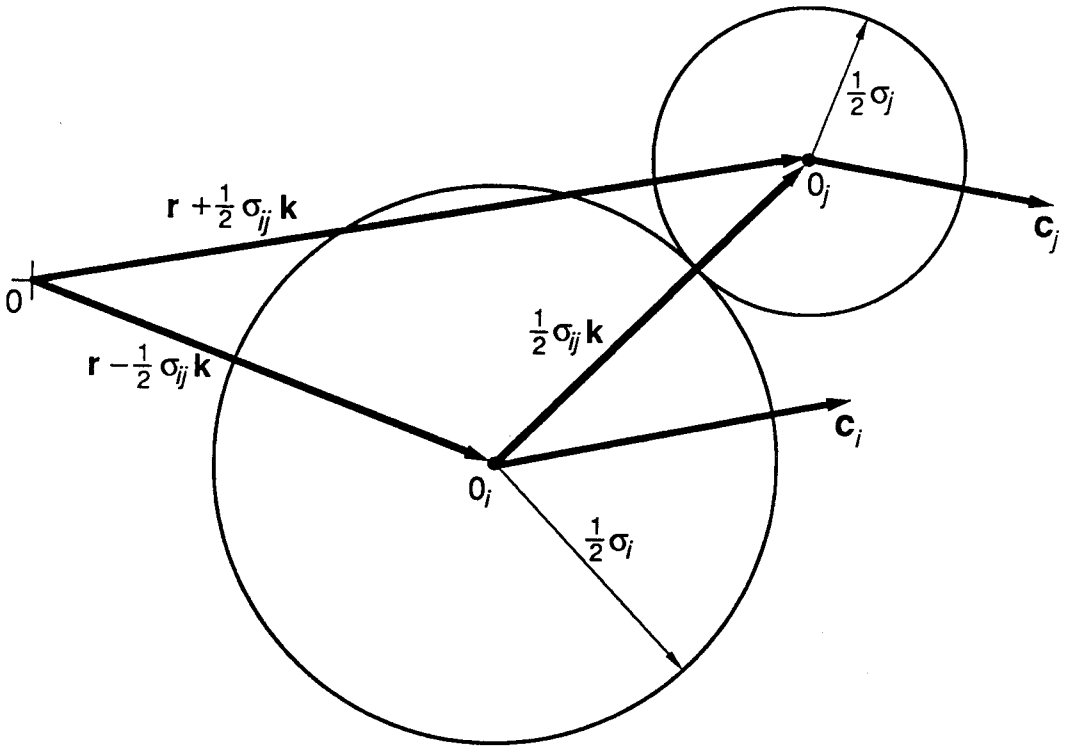

Figure 2.4: The collision of two particles of different species.

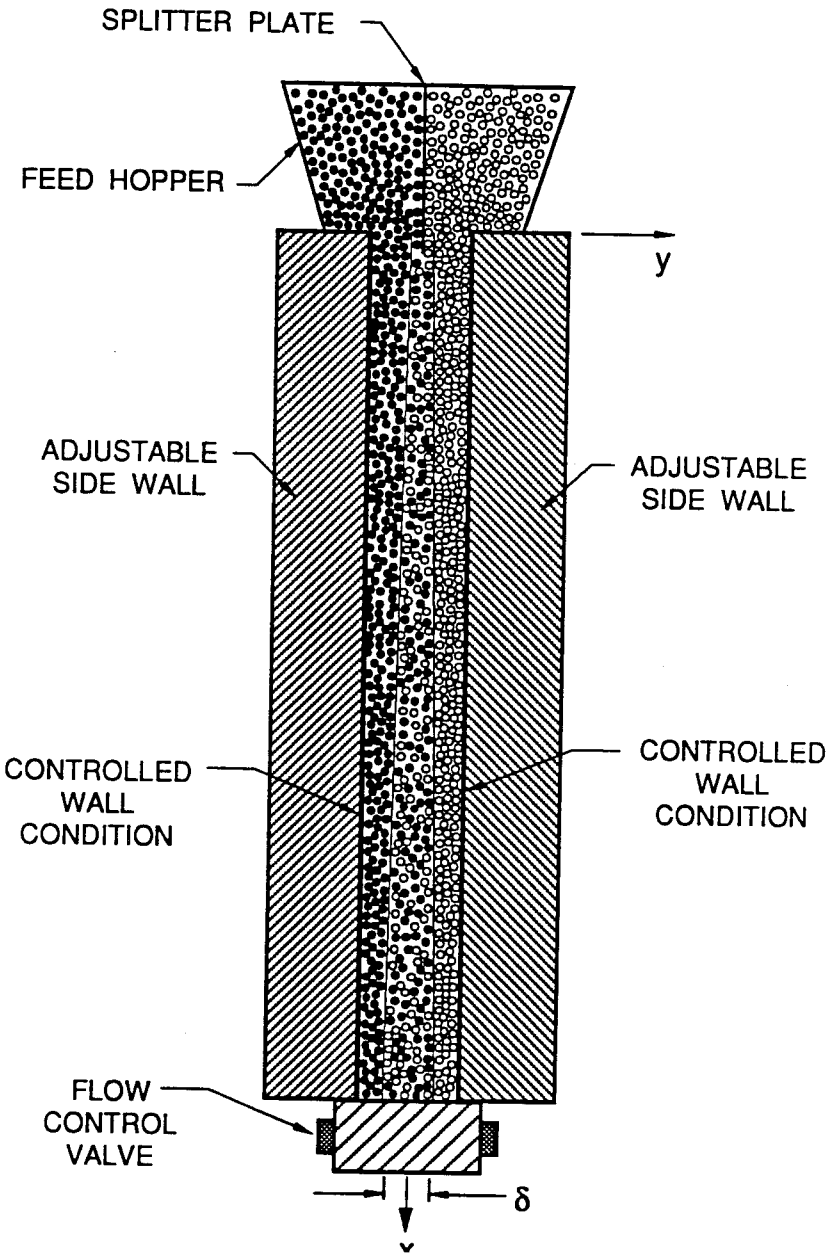

Figure 3.1: Schematic drawing of the experimental mixing-layer facility.

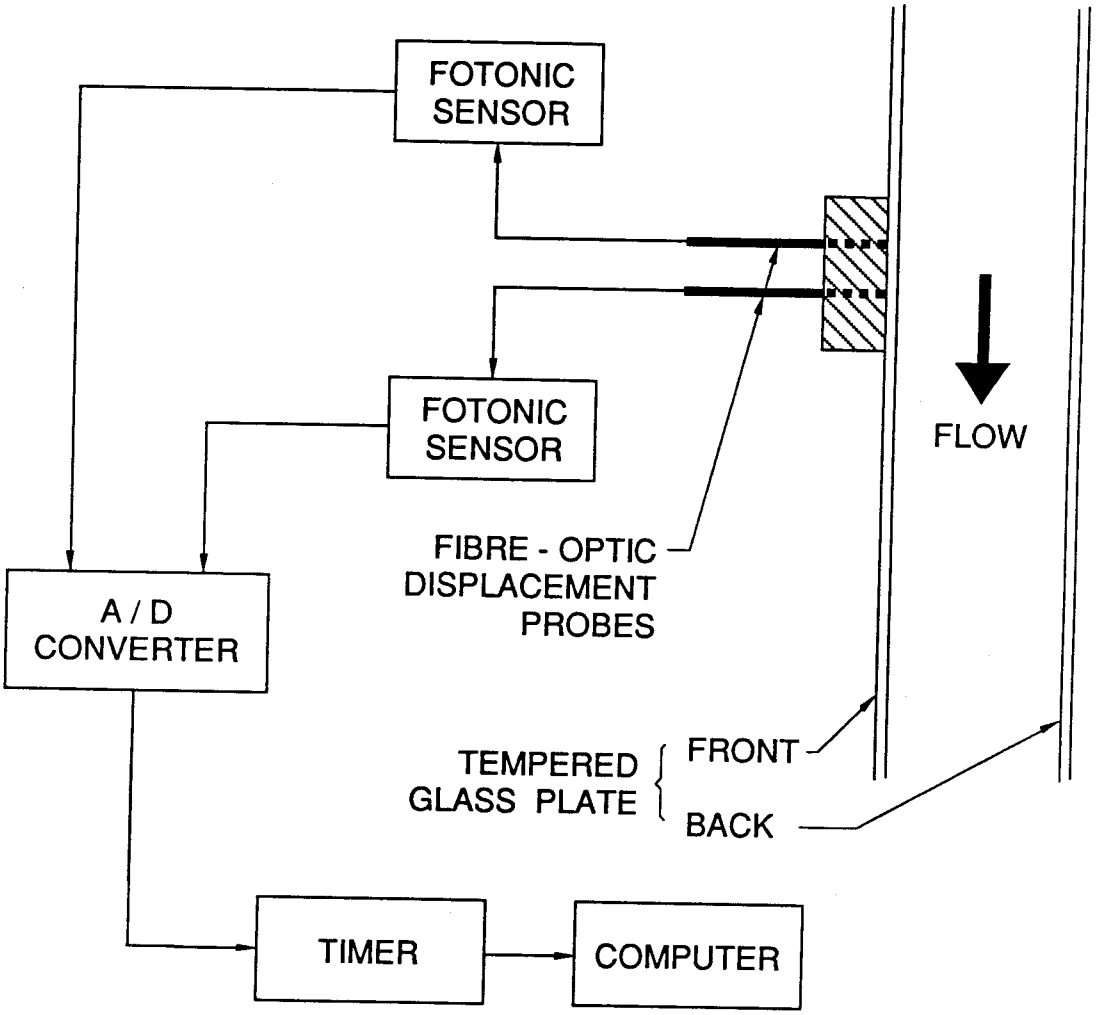

Figure 3.2: The flow chart for the velocity measurements.

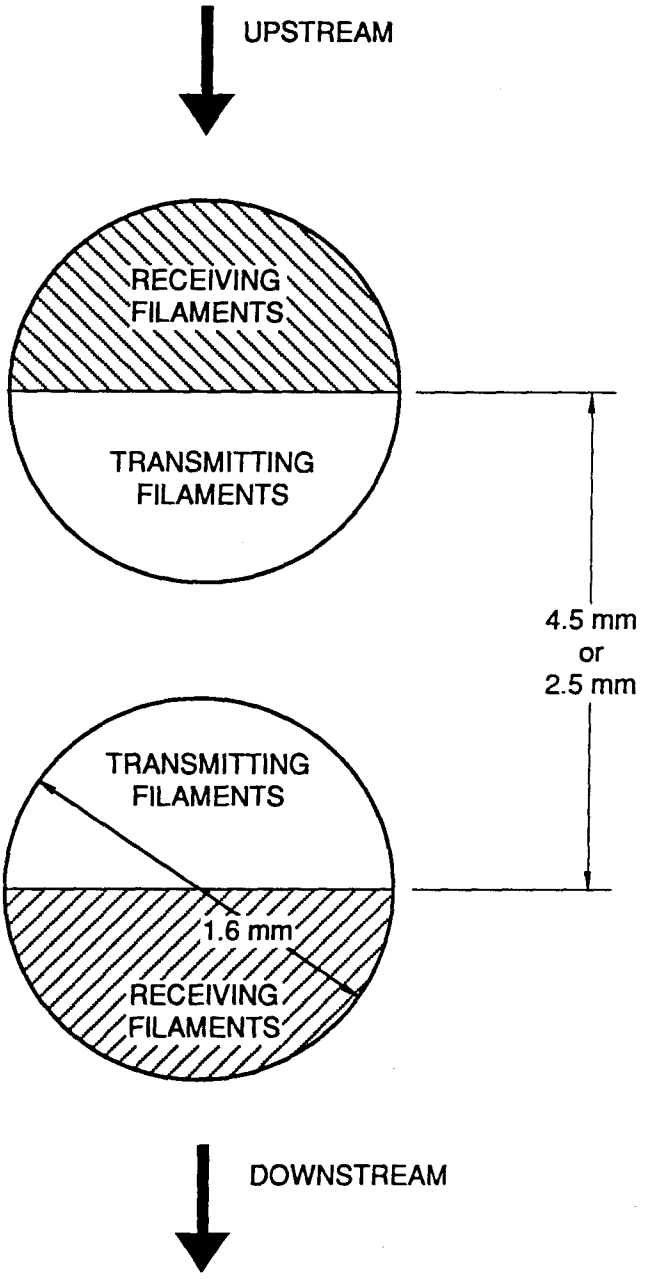

Figure 3.3: Geometry of the faces of the two displacement probes. The center-to-center distance is 4.5-mm apart for the 3-mm beads, and 2.5-mm apart for the 2-mm beads.

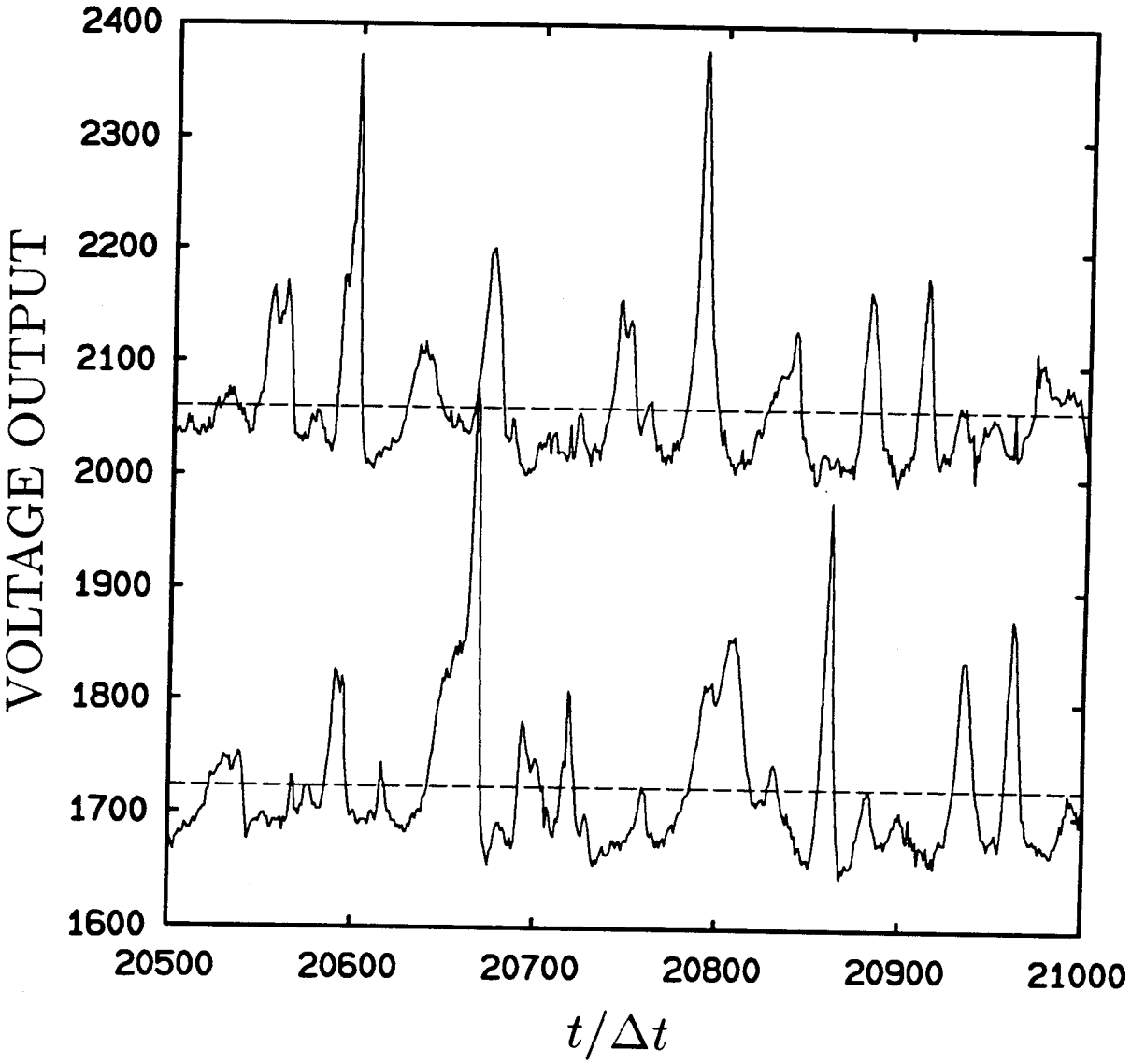

Figure 3.4: Typical voltage outputs (1 unit = 2.44 millivolts) from the two displacement probes, plotted against the dimensionless time, $t/\Delta t$, $\Delta t = 0.000785$ sec. The second voltage output is subtracted by 300 units to separate two curves. The dashed lines indicate the threshold voltages.

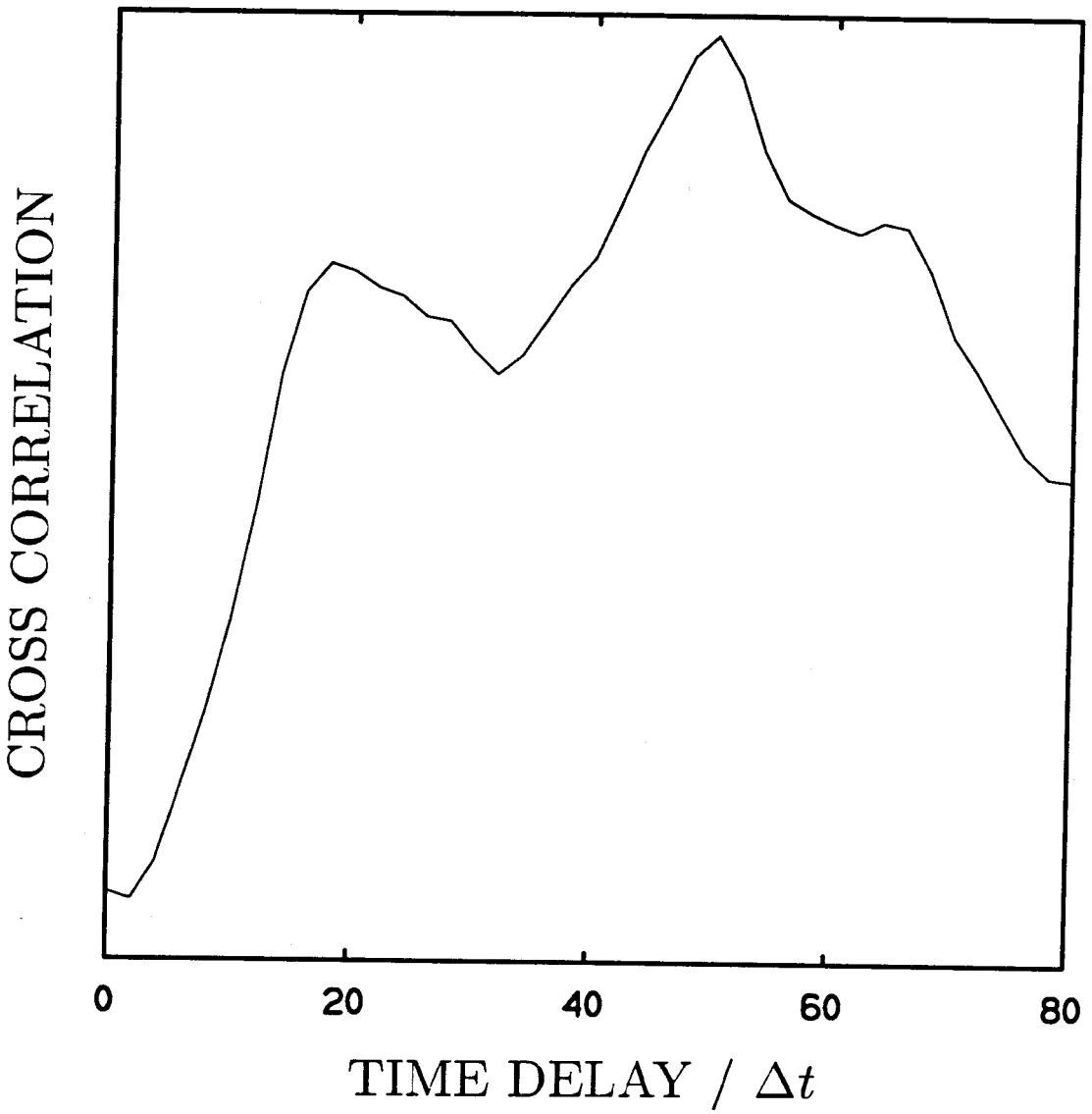

Figure 3.5: A typical cross-correlation curve calculated from the outputs of two displacement probes shown in Figure 3.4.

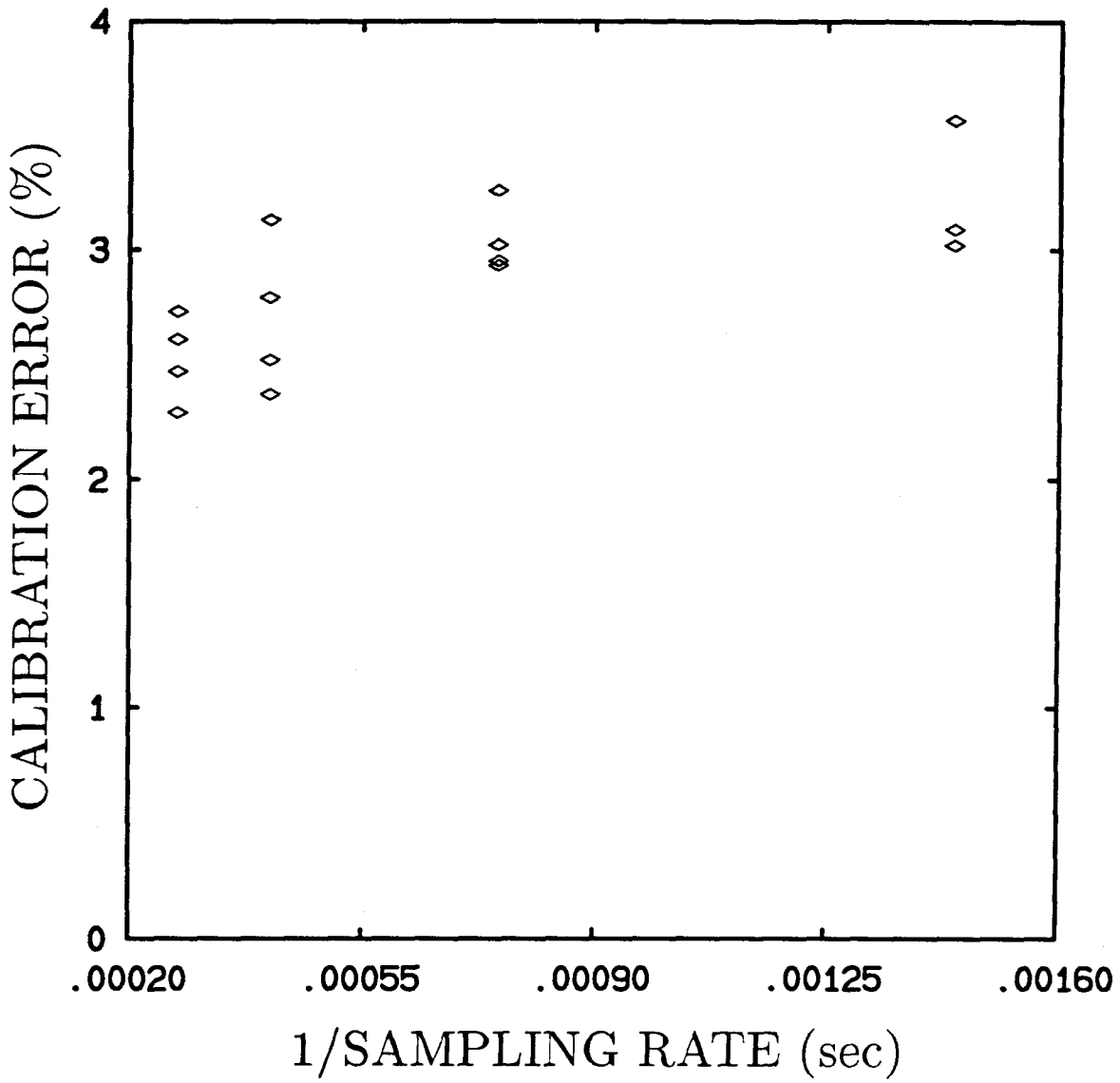

Figure 3.6: The calibration errors of the velocity measurements by using different sampling rates.

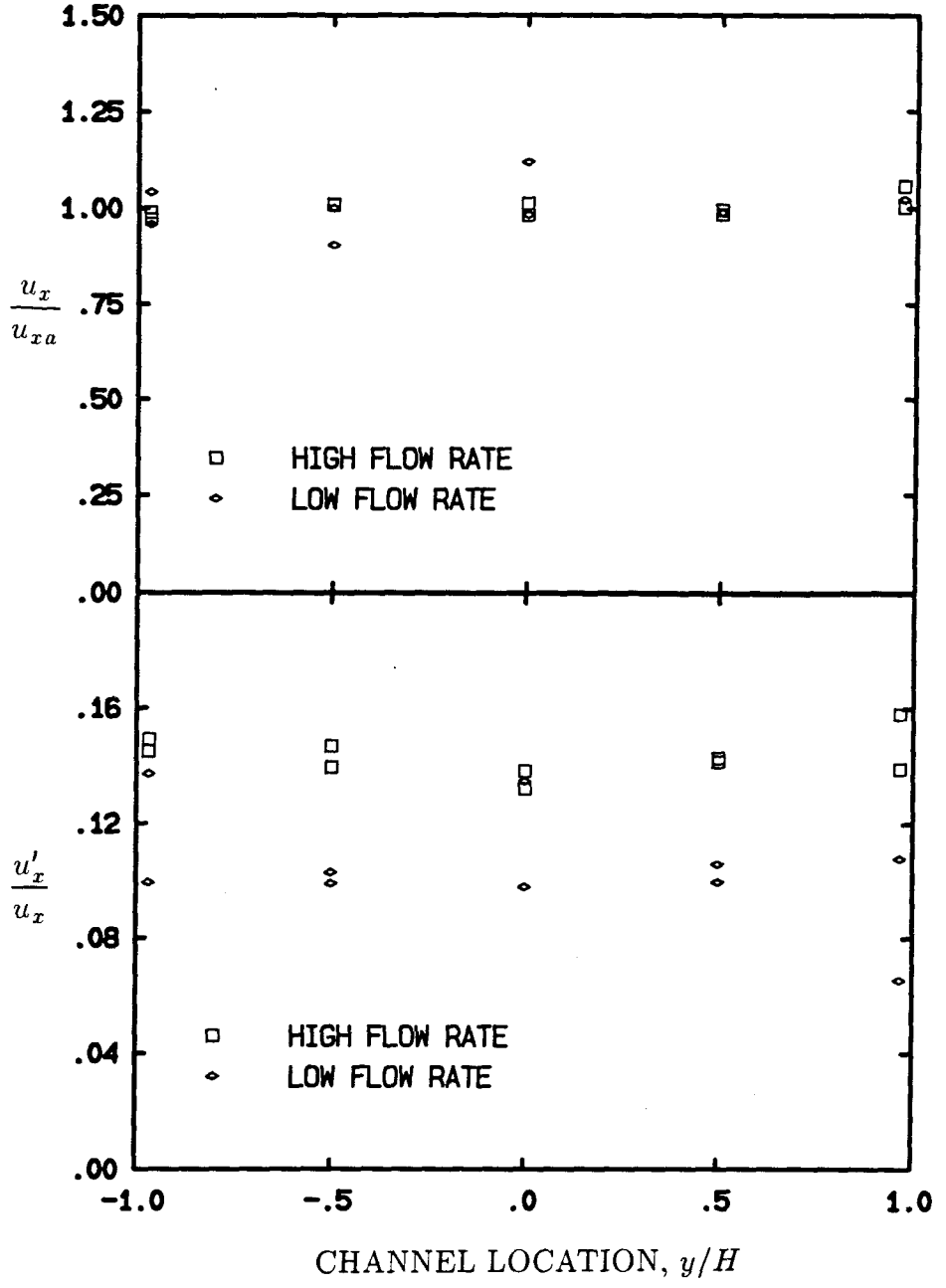

Figure 3.7: Local and fluctuating velocity distributions for the smooth-walled channel, $2H = 5.08$ cm, $u_{xa} = 4.5$ cm/sec for $\dot{m} = 0.08$ kg/sec, and $u_{xa} = 10.1$ cm/sec for $\dot{m} = 0.18$ kg/sec.

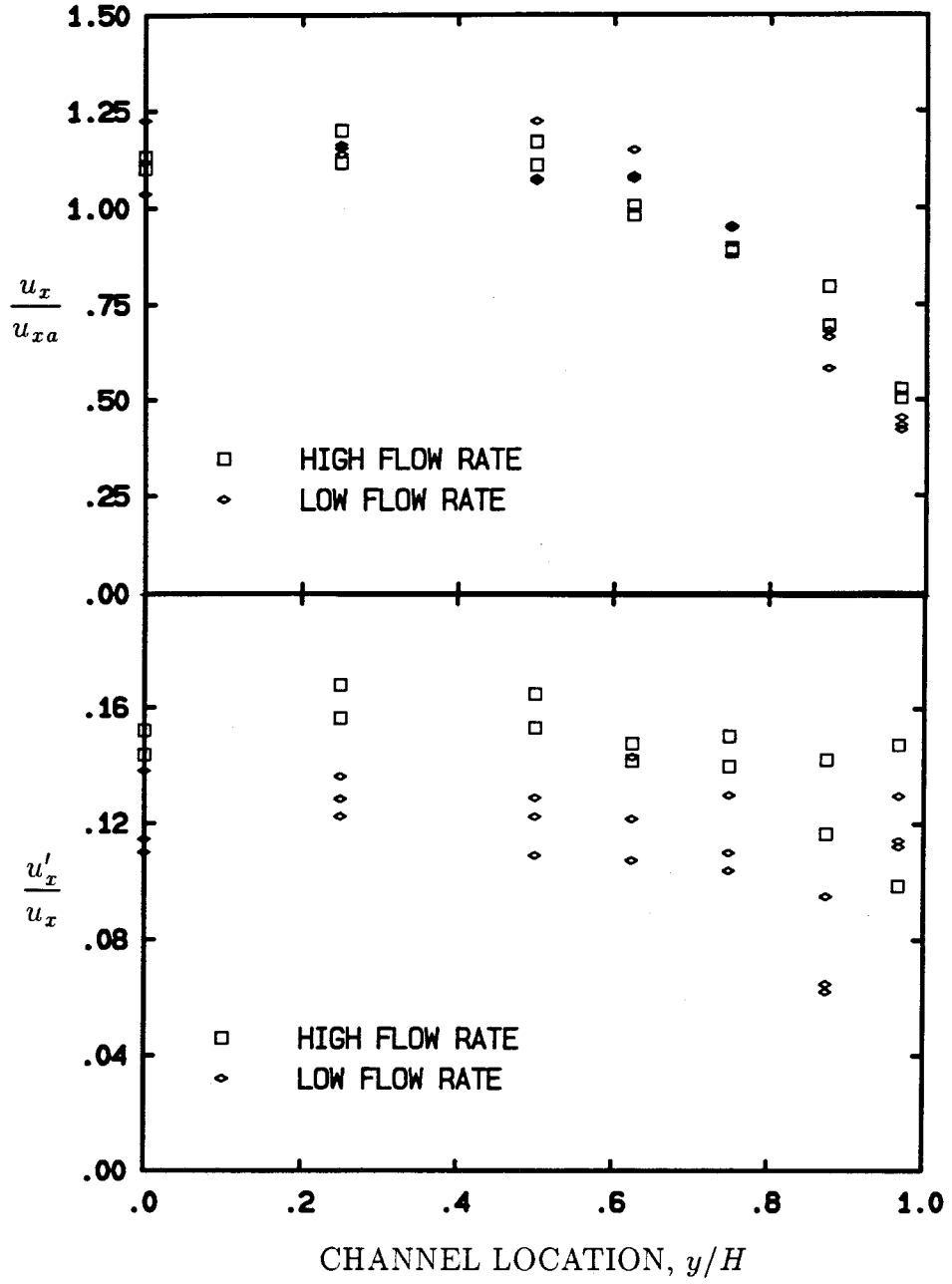

Figure 3.8: Local and fluctuating velocity distributions for the rough-walled wide channel, $2H = 5.08$ cm, $u_{xa} = 4.1$ cm/sec for $\dot{m} = 0.075$ kg/sec, and $u_{xa} = 10.3$ cm/sec for $\dot{m} = 0.19$ kg/sec.

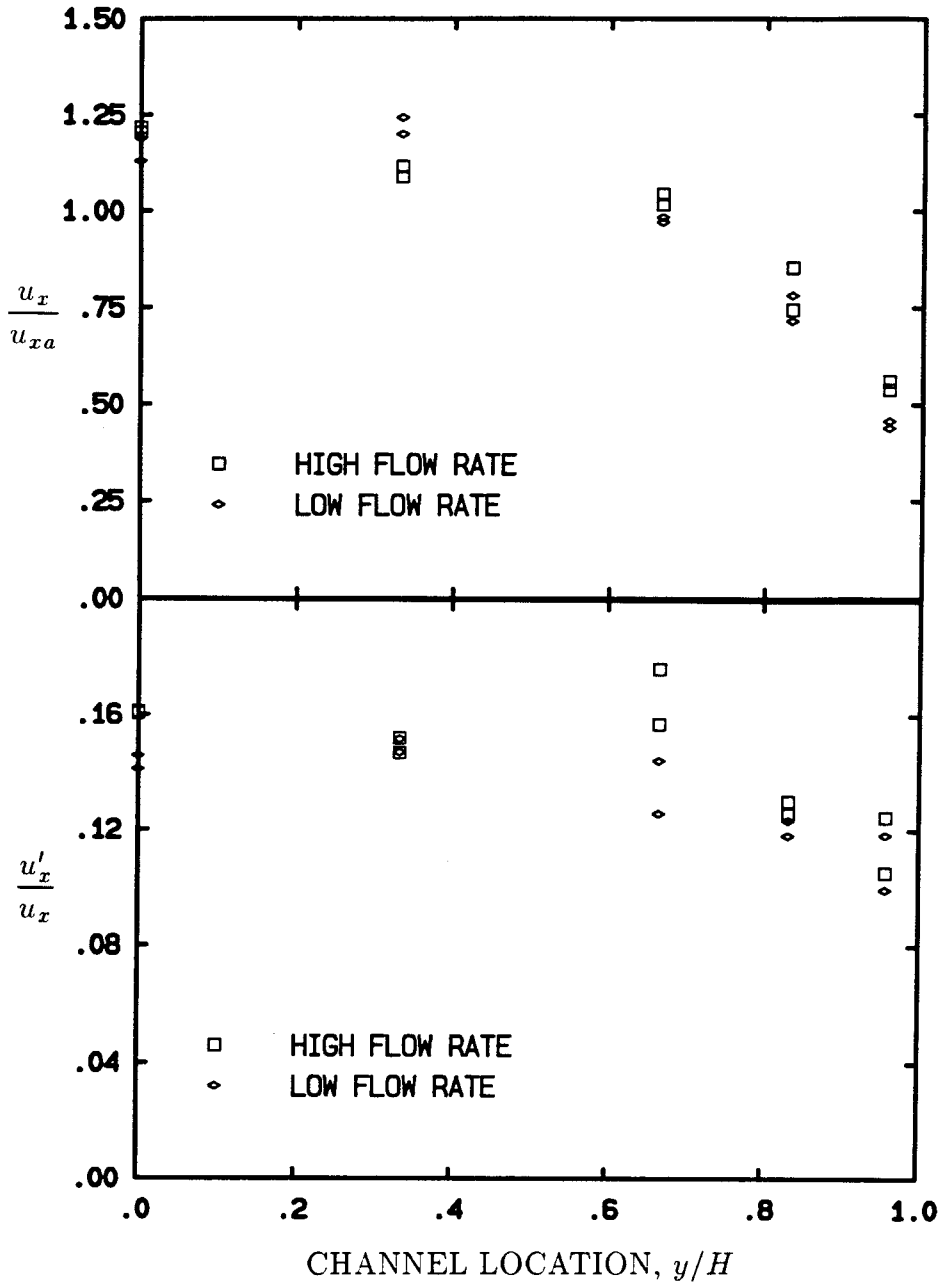

Figure 3.9: Local and fluctuating velocity distributions for the rough-walled narrow channel, $2H = 3.81$ cm, $u_{xa} = 5.4$ cm/sec for $\dot{m} = 0.070$ kg/sec, and $u_{xa} = 9.7$ cm/sec for $\dot{m} = 0.13$ kg/sec.

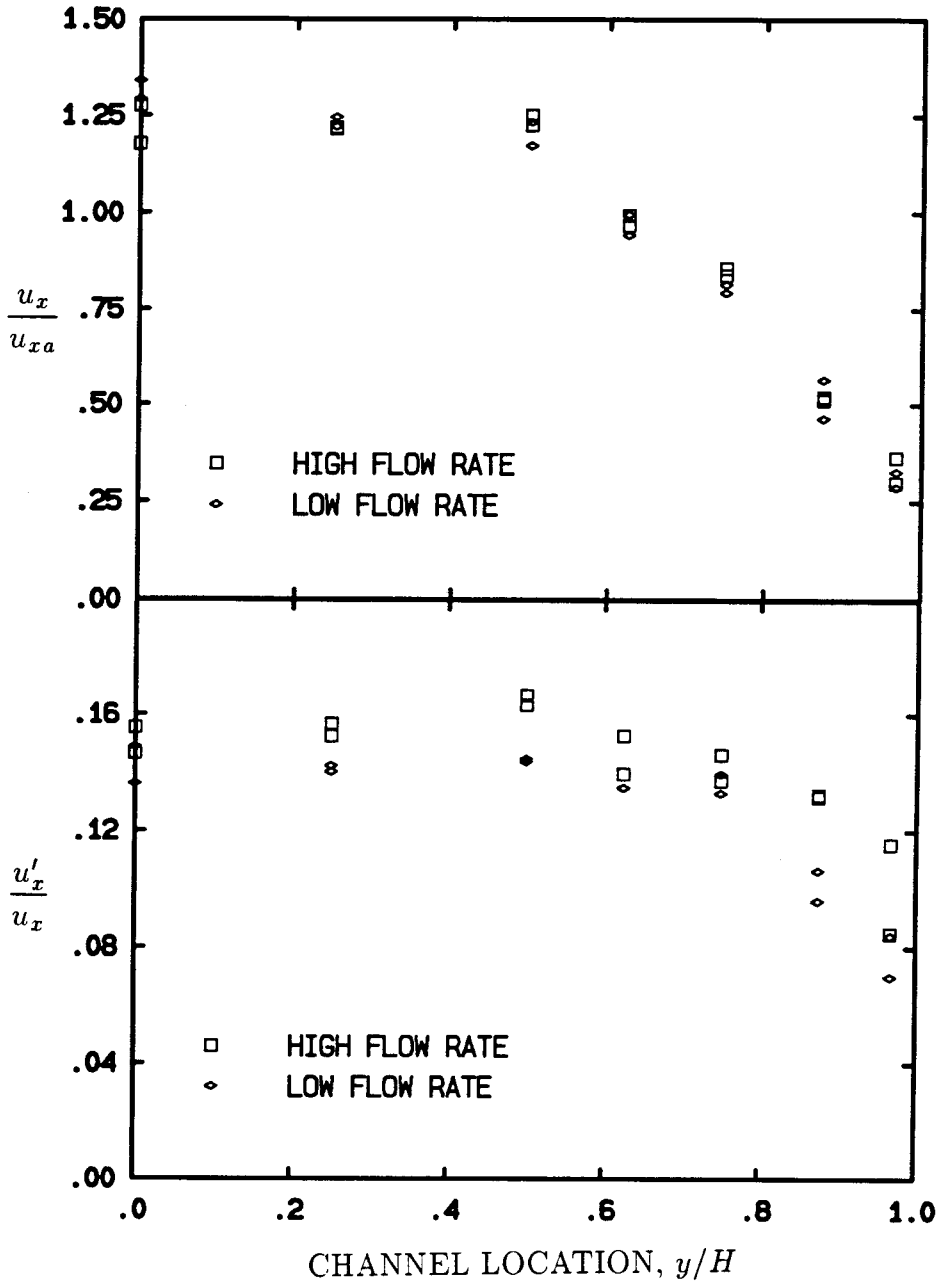

Figure 3.10: Local and fluctuating velocity distributions for the wide channel with saw-tooth walls, $2H = 5.08$ cm, $u_{xa} = 5.1$ cm/sec for $\dot{m} = 0.097$ kg/sec, and $u_{xa} = 10.9$ cm/sec for $\dot{m} = 0.20$ kg/sec.

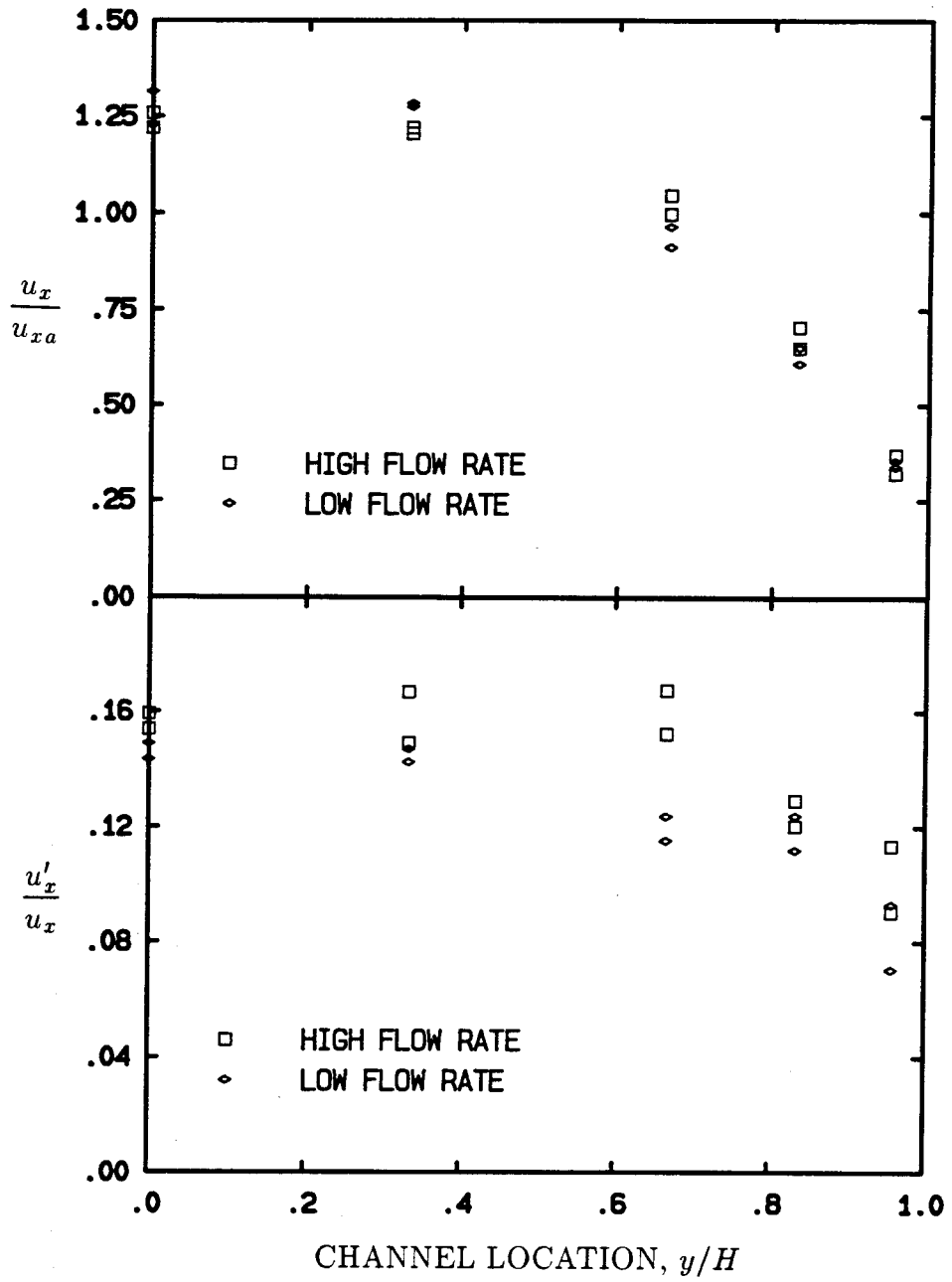

Figure 3.11: Local and fluctuating velocity distributions for the narrow channel with saw-tooth walls, $2H = 3.81$ cm, $u_{xa} = 4.9$ cm/sec for $\dot{m} = 0.071$ kg/sec, and $u_{xa} = 9.7$ cm/sec for $\dot{m} = 0.13$ kg/sec.

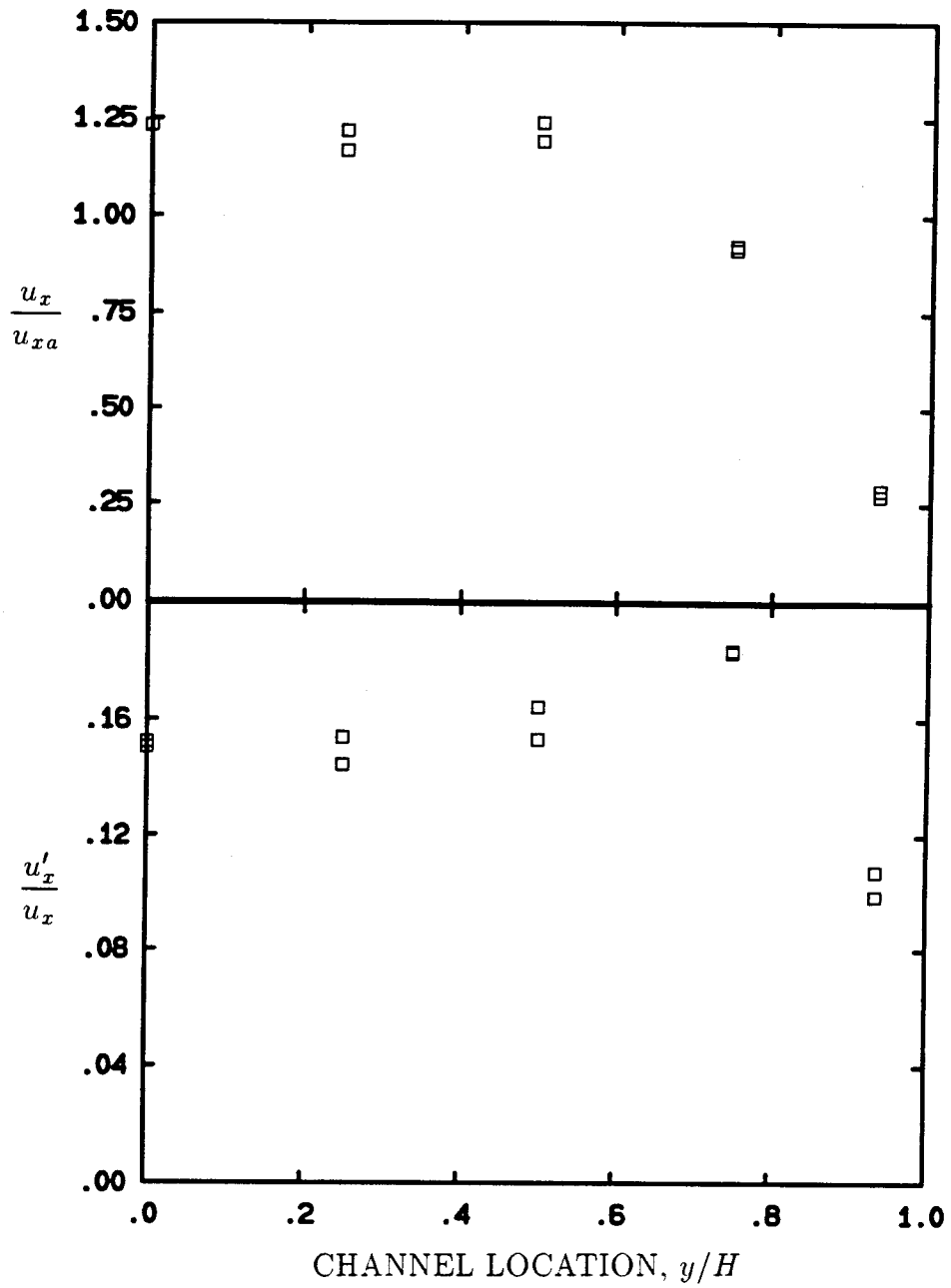

Figure 3.12: Local and fluctuating velocity distributions using 2-mm diameter beads with saw-tooth walls, $2H = 2.54$ cm, $u_{xa} = 18.5$ cm/sec and $\dot{m} = 0.15$ kg/sec.

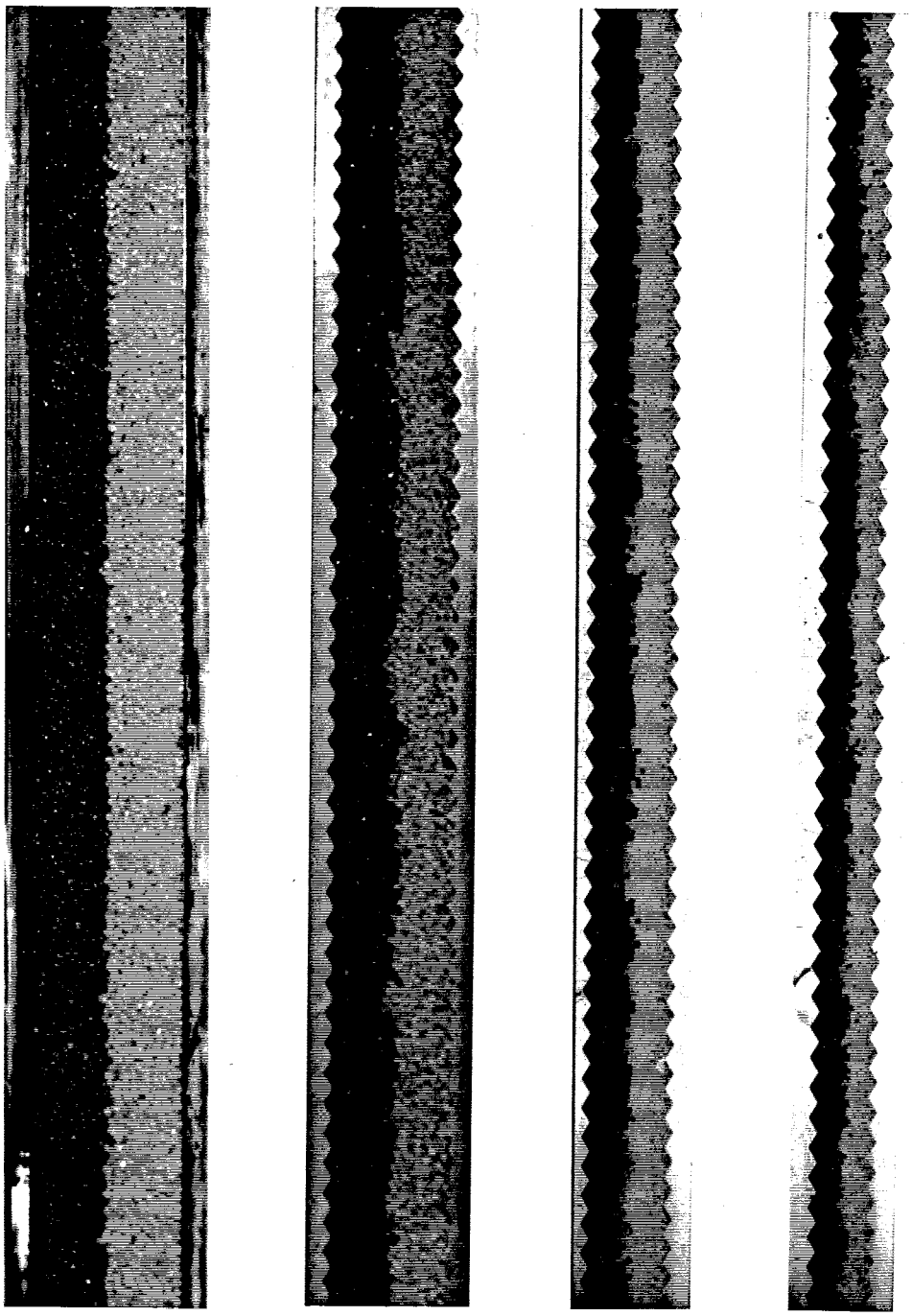

Figure 3.13: Typical particle distributions (45 cm $< x <$ 89 cm) for (a) the smooth-walled channel with 3-mm beads ($2H$ = 5.08 cm), (b) the saw-tooth narrow channel with 3-mm beads ($2H$ = 3.81 cm), (c) the saw-tooth channel with 2-mm beads ($2H$ = 2.54 cm), (d) the saw-tooth channel with 1-mm beads ($2H$ = 1.59 cm).

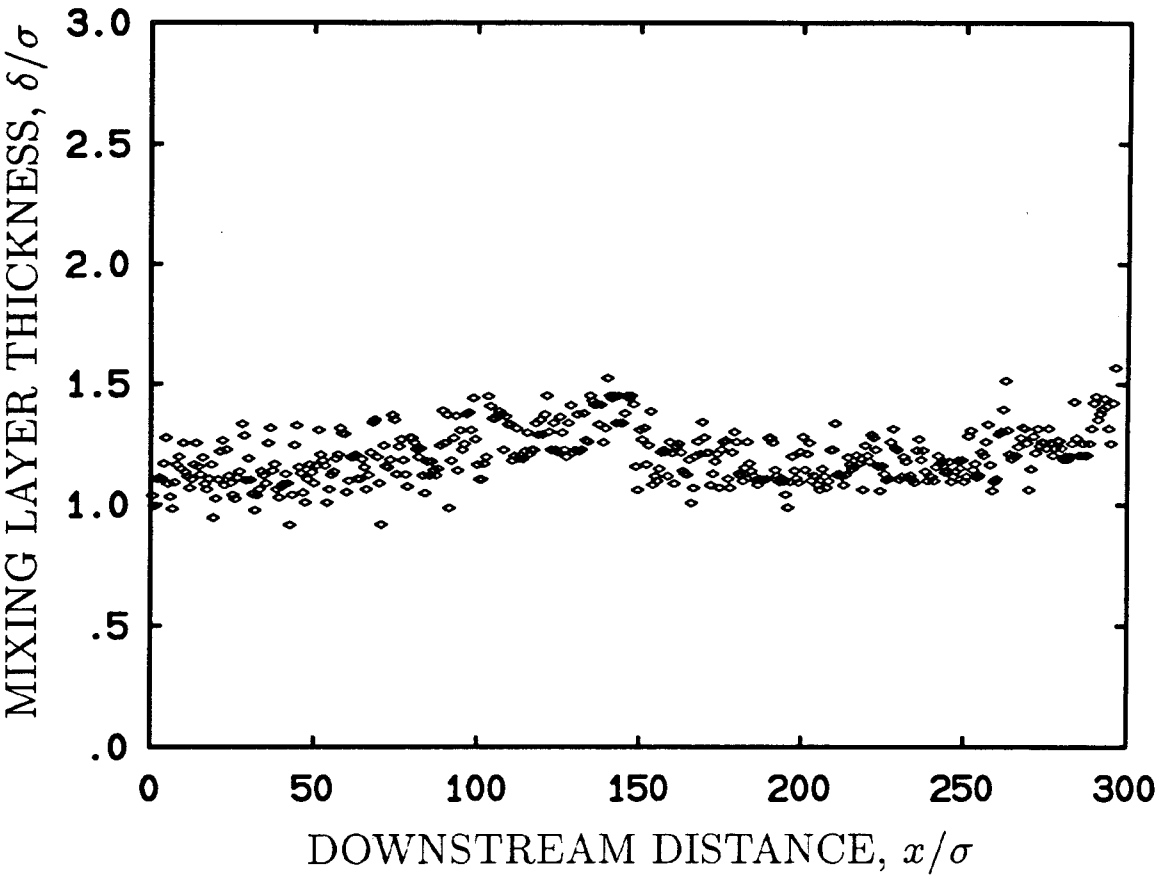

Figure 3.14: The growth of the mixing-layer thickness, δ/σ, as a function of downstream distance, x/σ, for the smooth-walled channel, $\dot{m} = 0.091$ kg/sec, and $2H = 5.08$ cm.

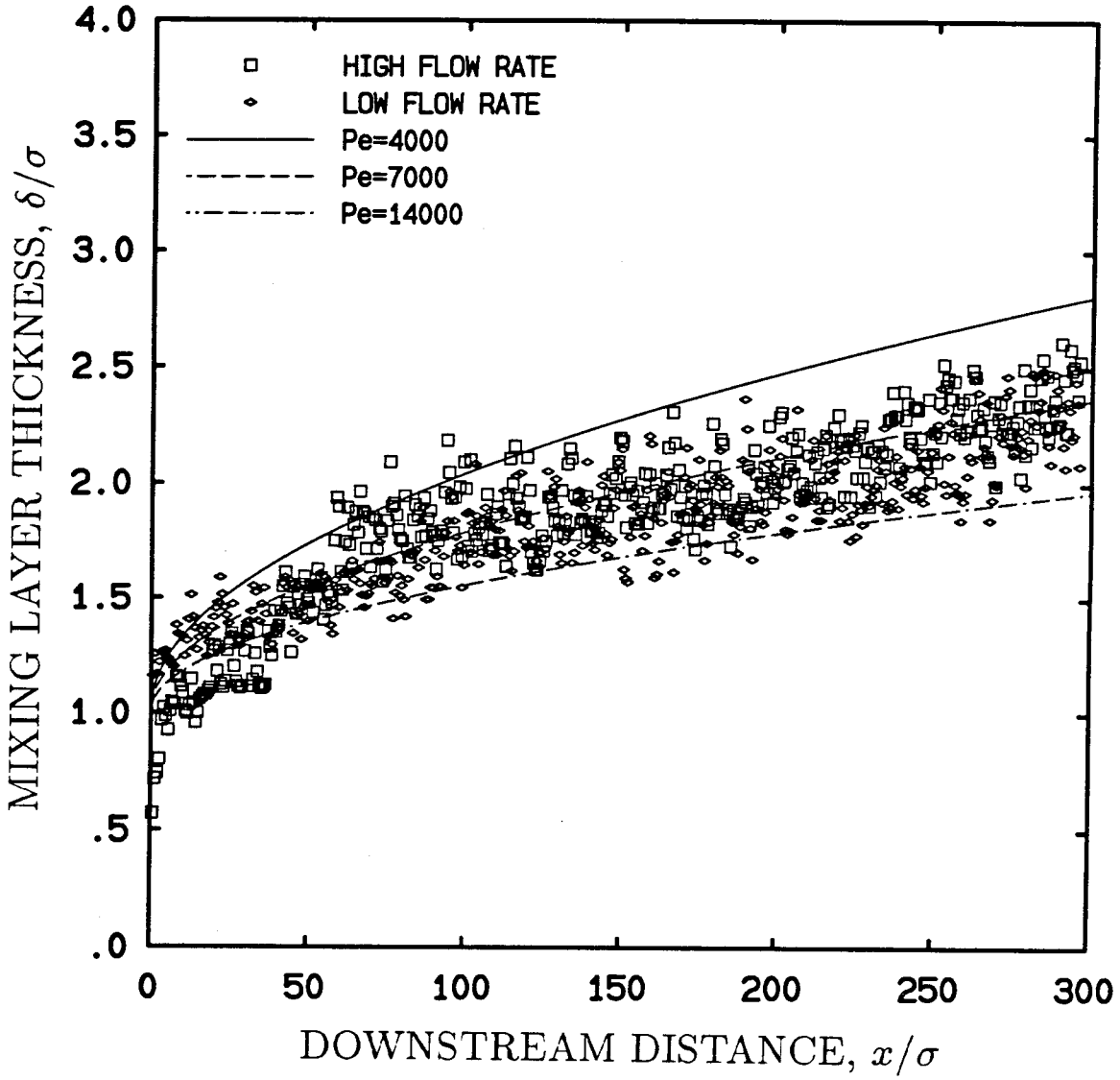

Figure 3.15: The growth of the mixing-layer thickness, δ/σ, as a function of downstream distance, x/σ, for the wide rough-walled channel, low flow rate $\dot{m} = 0.10$ kg/sec, and high flow rate $\dot{m} = 0.20$ kg/sec.

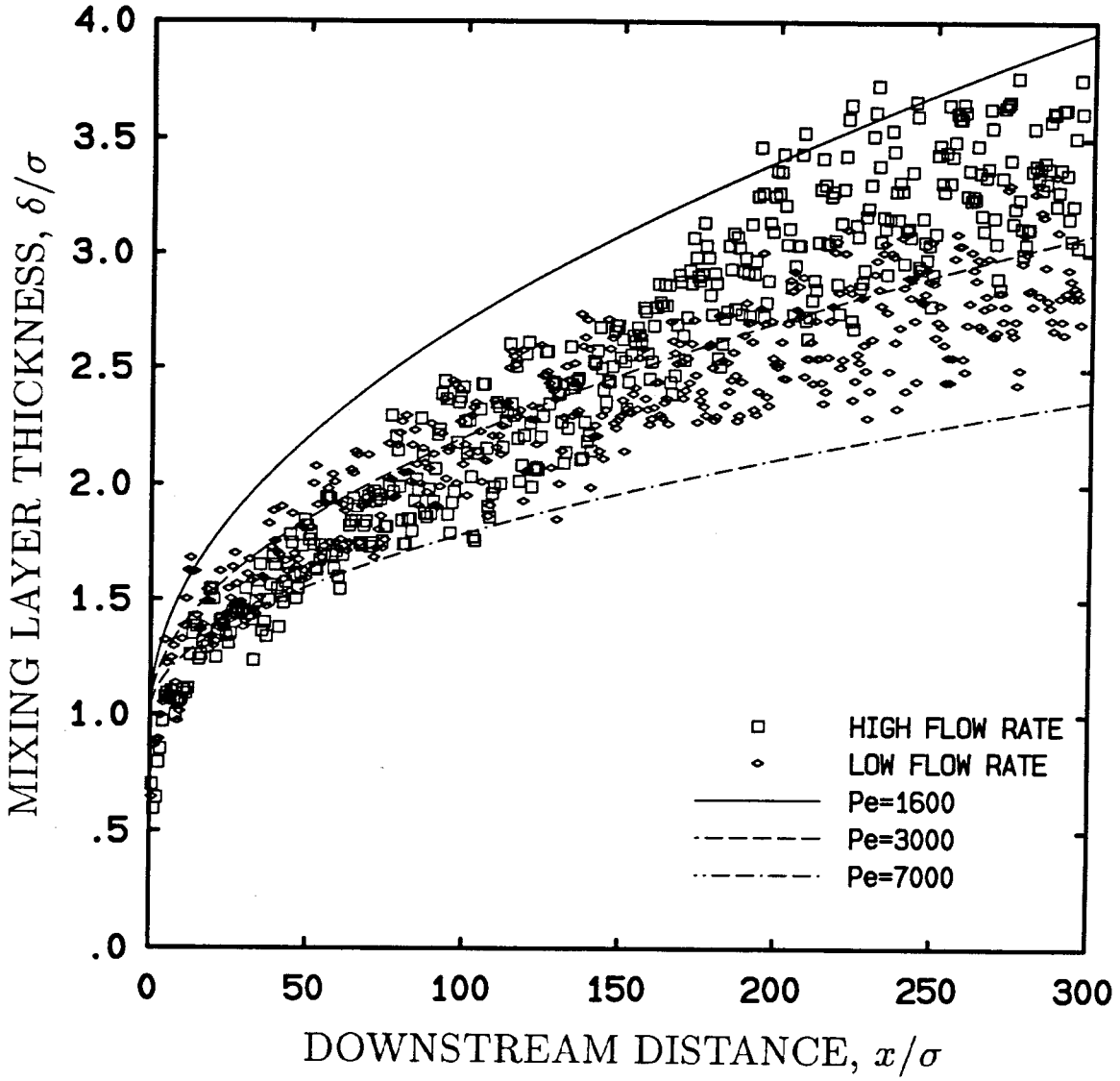

Figure 3.16: The growth of the mixing-layer thickness, δ/σ, as a function of downstream distance, x/σ, for the narrow rough-walled channel, low flow rate $\dot{m} = 0.070$ kg/sec, and high flow rate $\dot{m} = 0.13$ kg/sec.

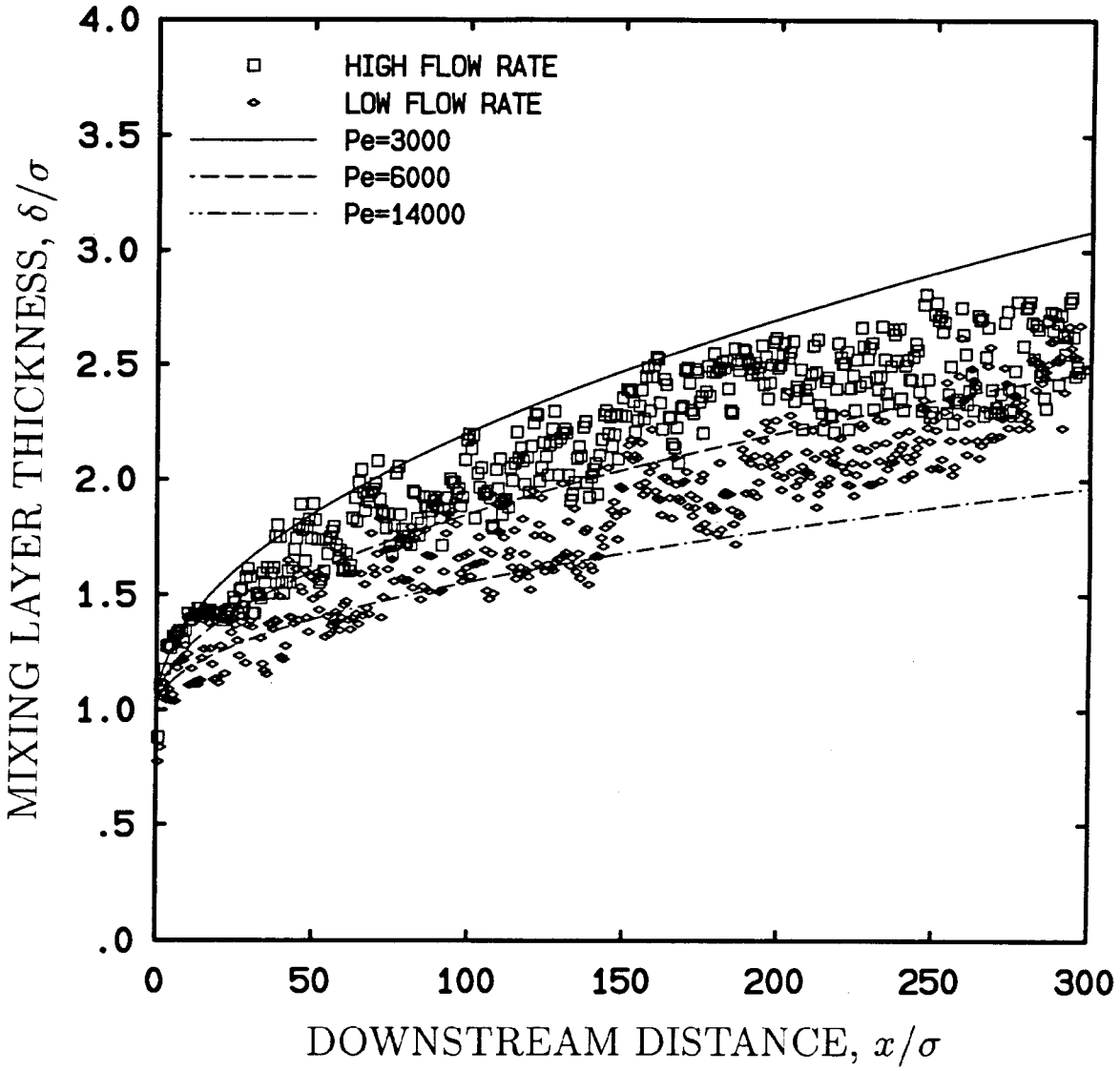

Figure 3.17: The growth of the mixing-layer thickness, δ/σ, as a function of downstream distance, x/σ, for the wide channel with saw-tooth walls, low flow rate $\dot{m} =$ 0.10 kg/sec, and high flow rate $\dot{m} = 0.20$ kg/sec.

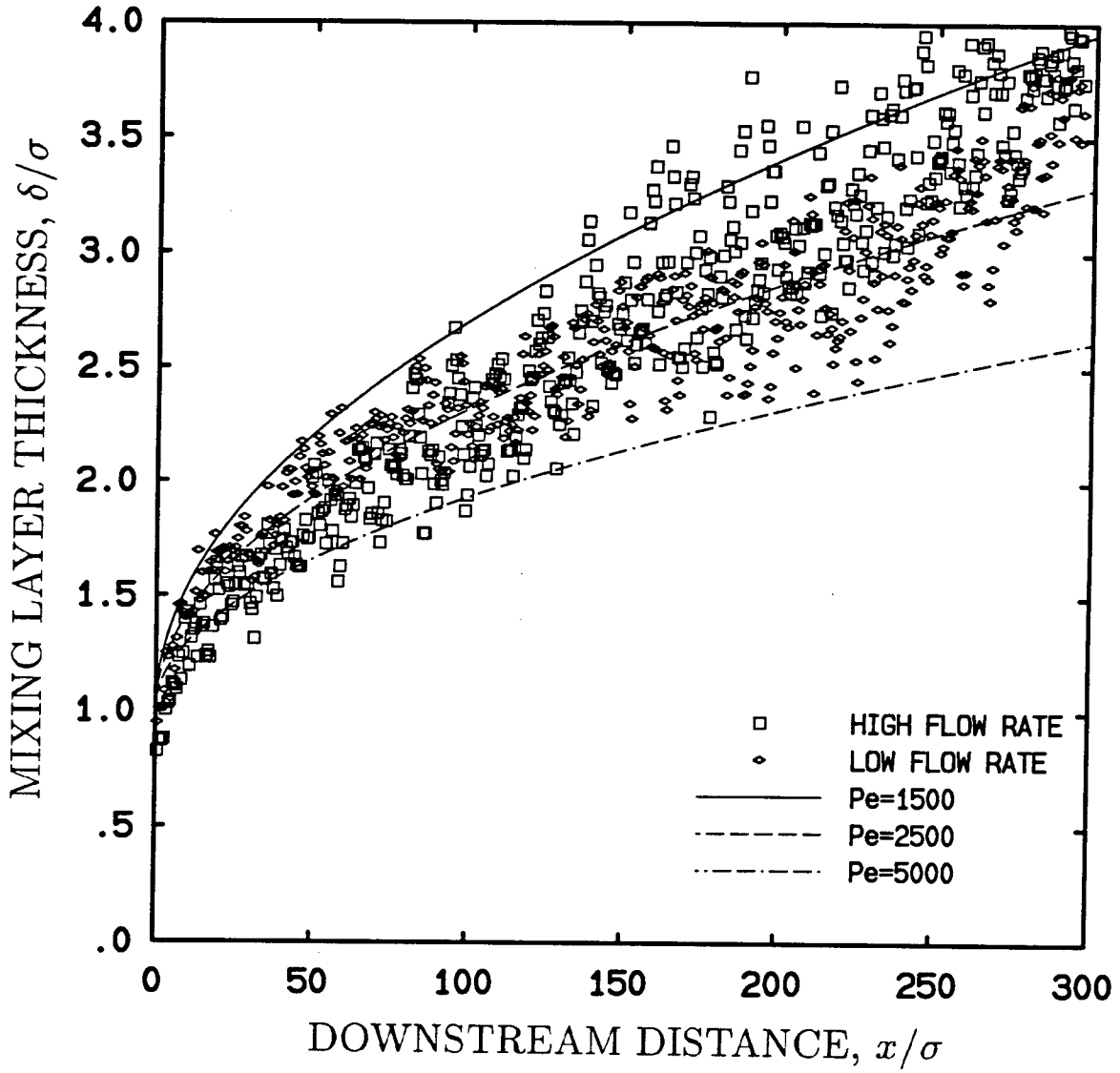

Figure 3.18: The growth of the mixing-layer thickness, δ/σ, as a function of downstream distance, x/σ, for the narrow channel with saw-tooth walls, low flow rate $\dot{m}$ = 0.074 kg/sec, and high flow rate $\dot{m}$ = 0.14 kg/sec.

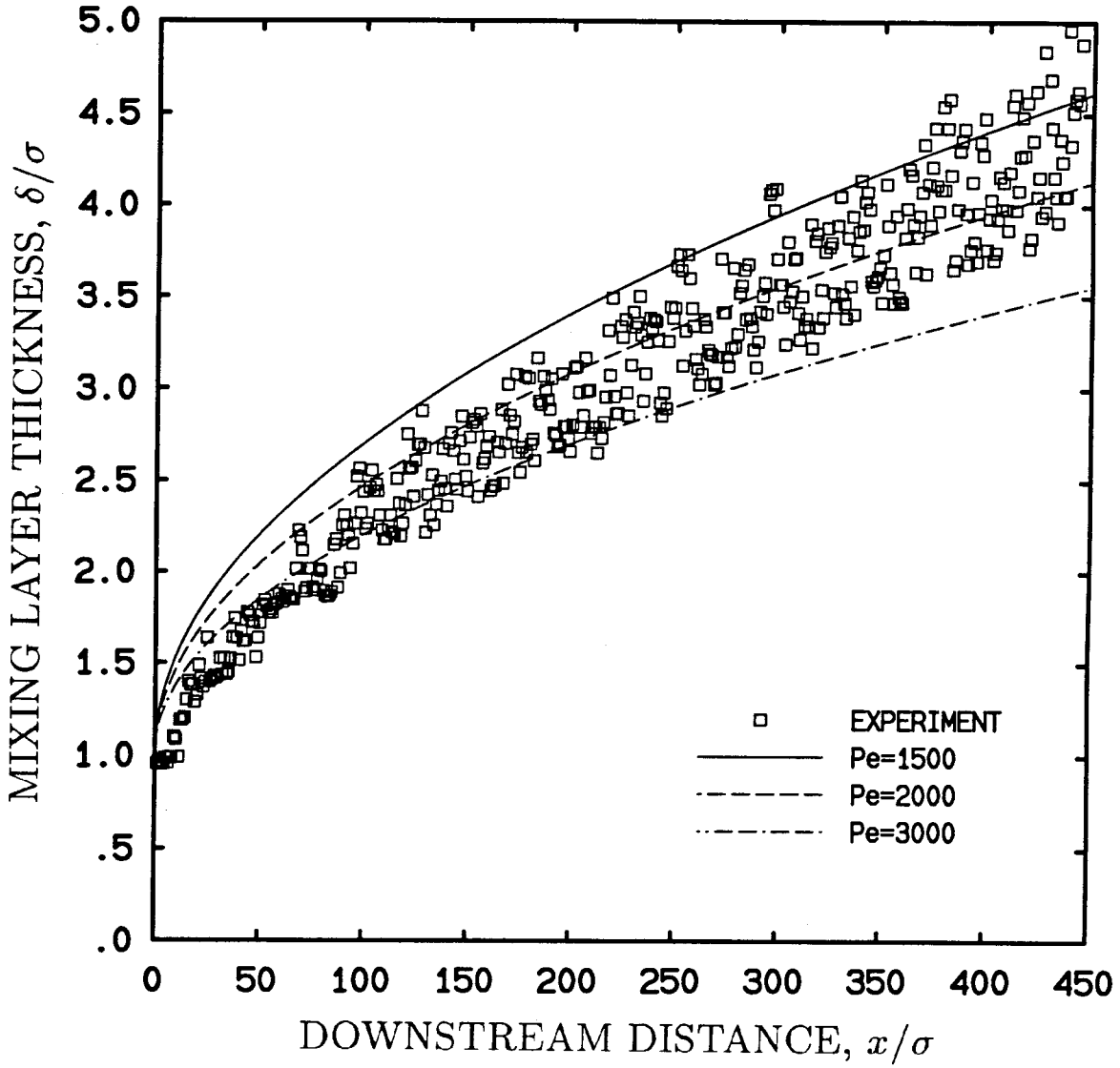

Figure 3.19: The growth of the mixing-layer thickness, δ/σ, as a function of downstream distance, x/σ, using 2-mm beads with saw-tooth walls, $\dot{m} = 0.15$ kg/sec, and $2H = 2.54$ cm.

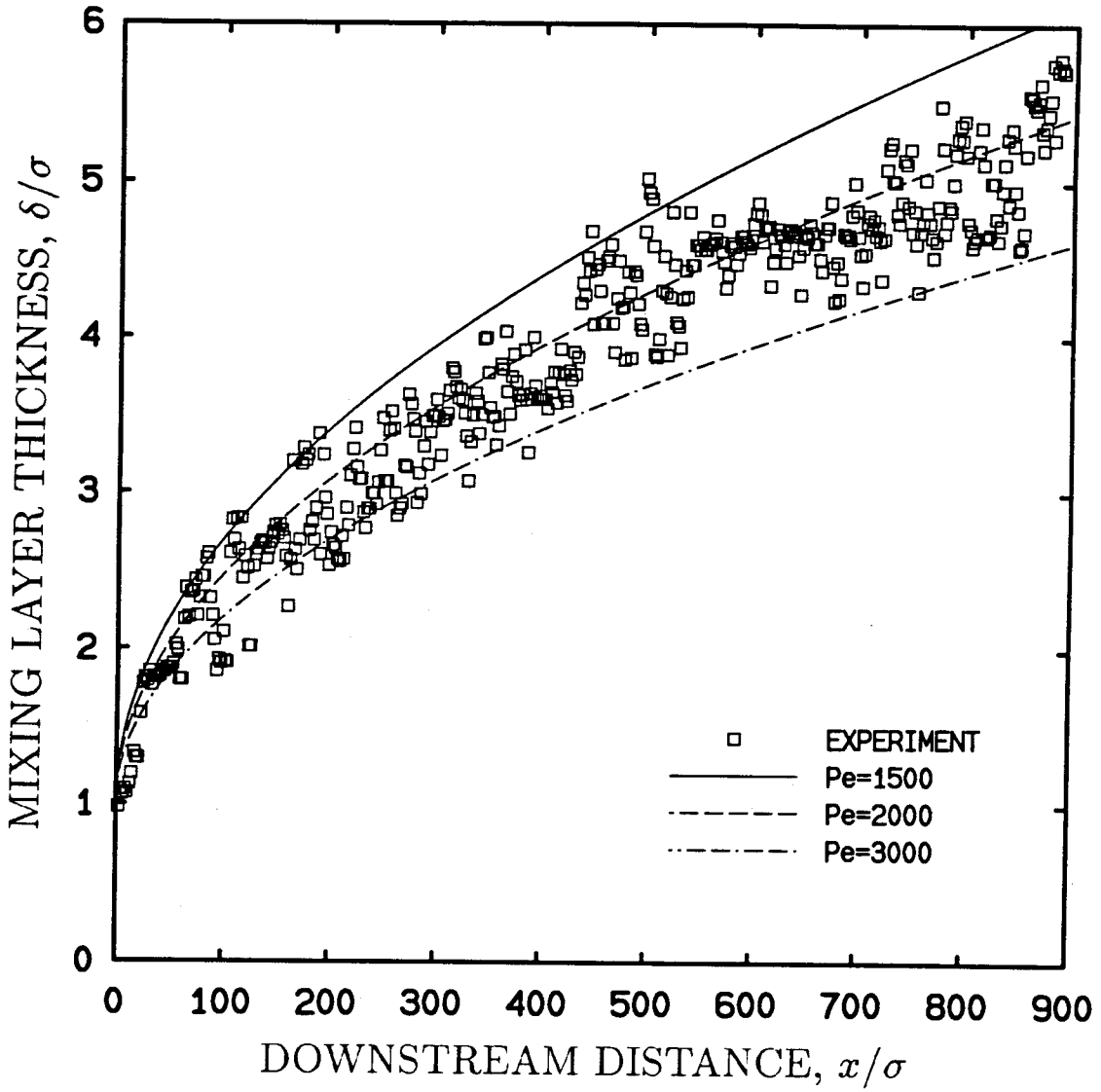

Figure 3.20: The growth of the mixing-layer thickness, δ/σ, as a function of downstream distance, x/σ, using 1-mm beads with saw-tooth walls, $\dot{m} = 0.077$ kg/sec, and $2H = 1.59$ cm.

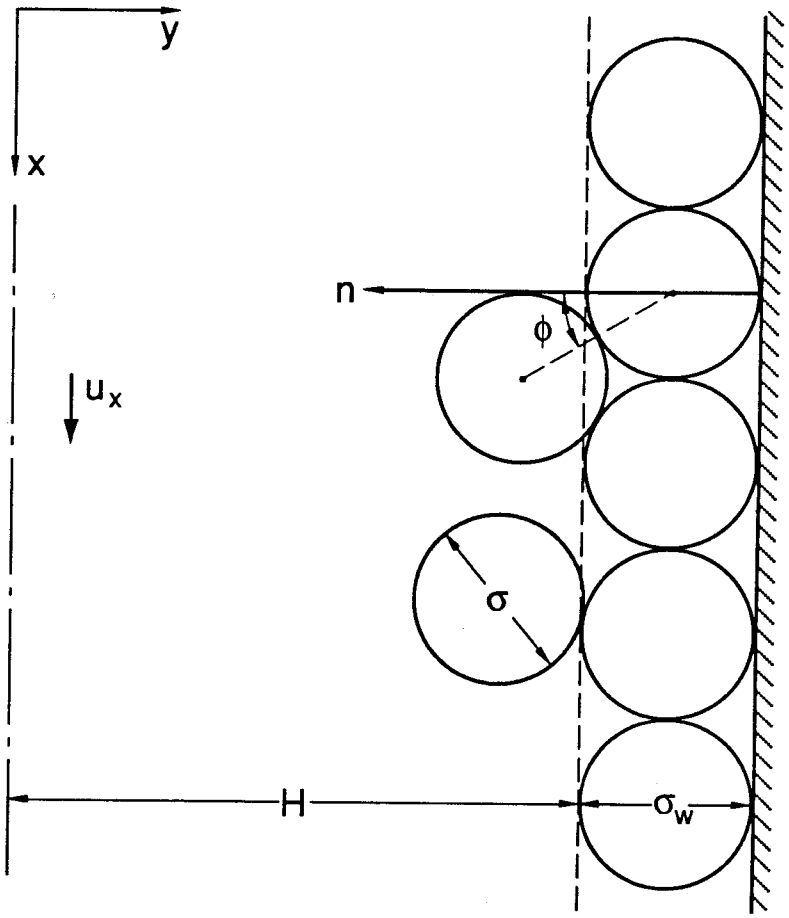

Figure 4.1: The coordinate system and wall geometry of a two-dimensional flow.

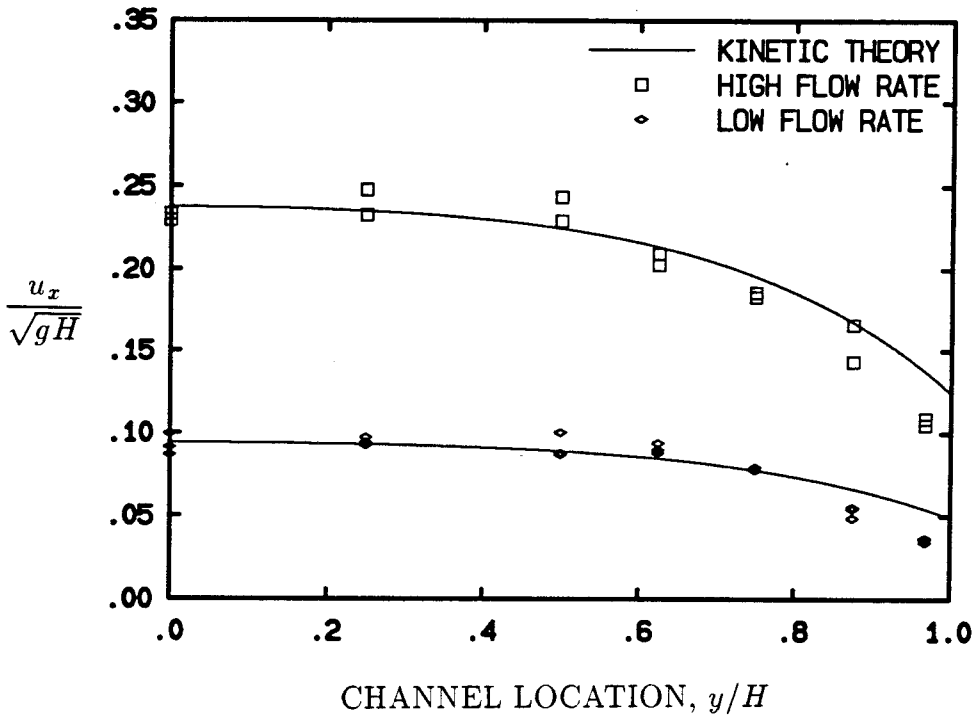

Figure 4.2: Local velocity distributions for the rough-walled wide channel, $2H$ = 5.08 cm. The curves are the calculated velocity profiles based on the kinetic theory analysis.

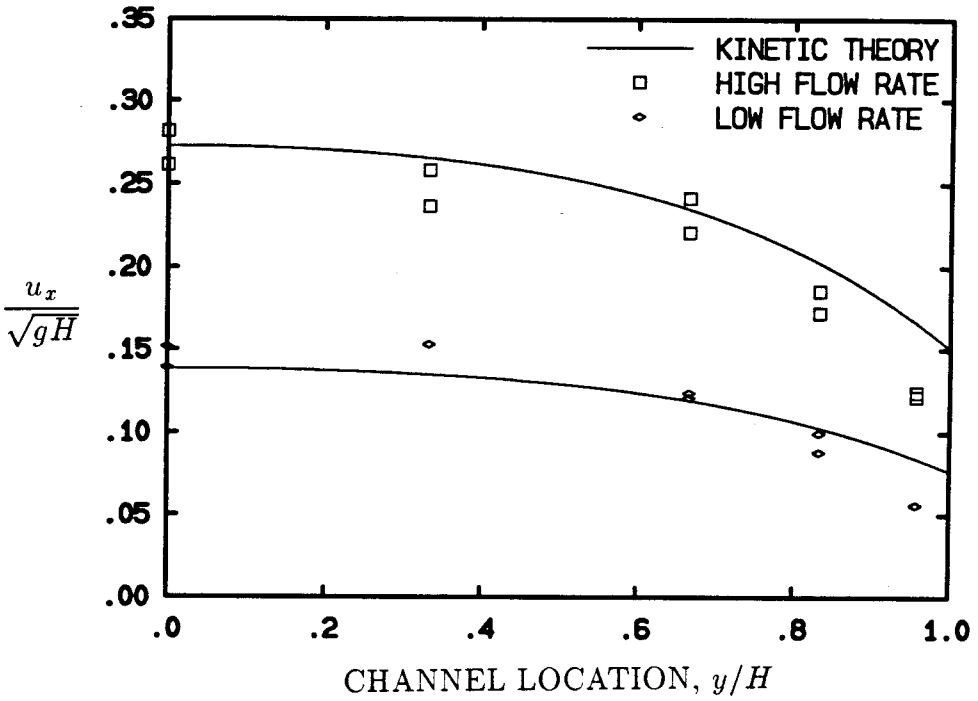

Figure 4.3: Local velocity distributions for the rough-walled narrow channel, $2H =$ 3.81 cm. The curves are the calculated velocity profiles based on the kinetic theory analysis.

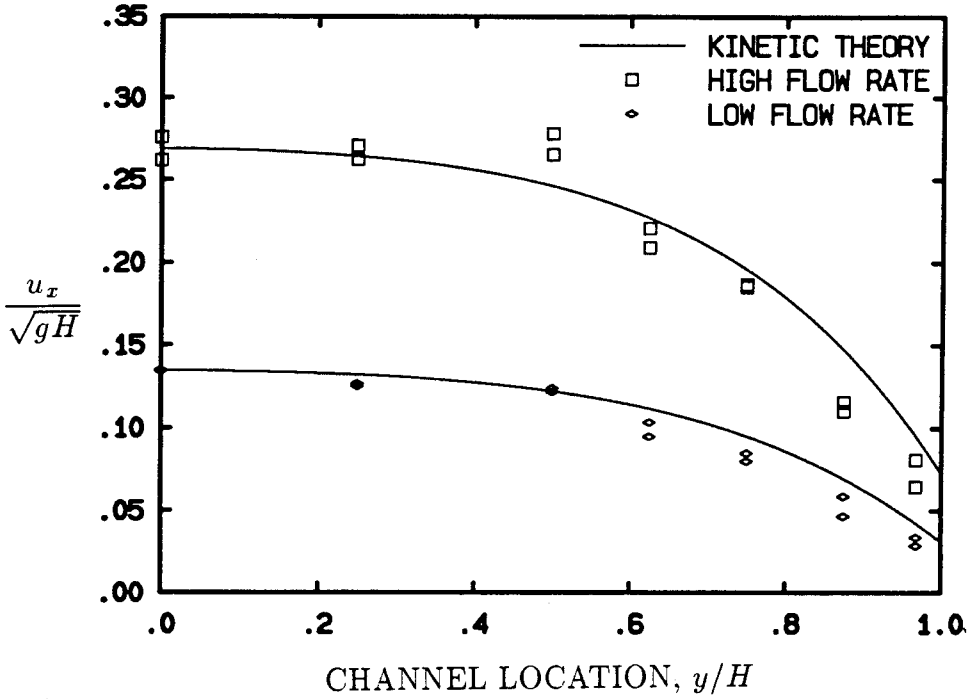

Figure 4.4: Local velocity distributions for the wide channel with saw-tooth walls, $2H = 5.08$ cm. The curves are the calculated velocity profiles from the kinetic theory analysis using the centerline and slip-velocities as boundary conditions.

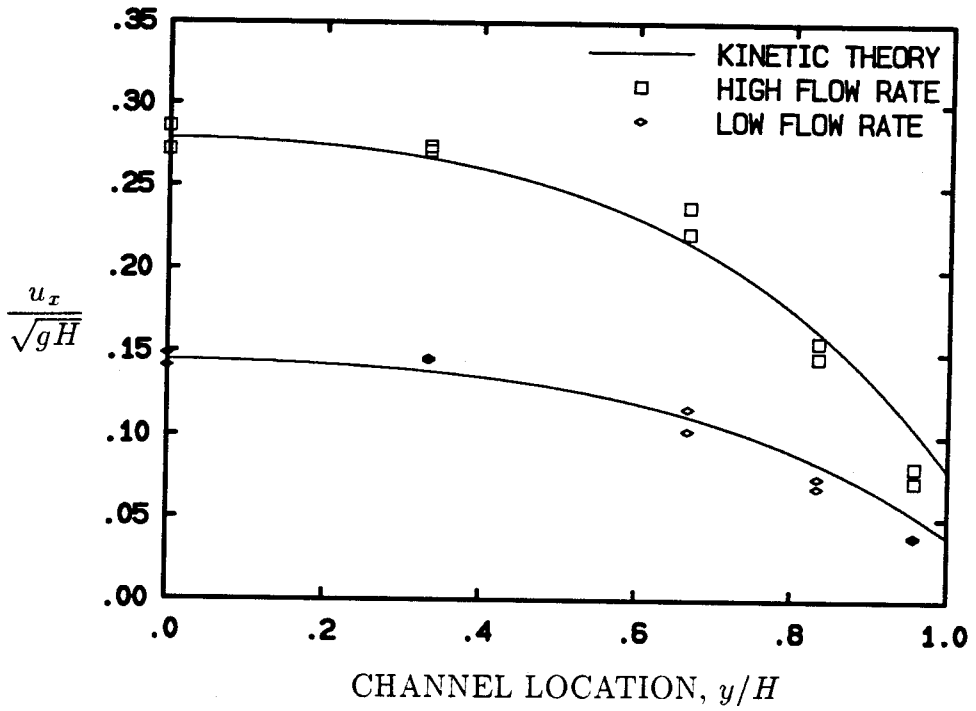

Figure 4.5: Local velocity distributions for the narrow channel with saw-tooth walls, $2H = 3.81$ cm. The curve are the calculated velocity profiles from the kinetic theory analysis using the centerline and slip-velocities as boundary conditions.

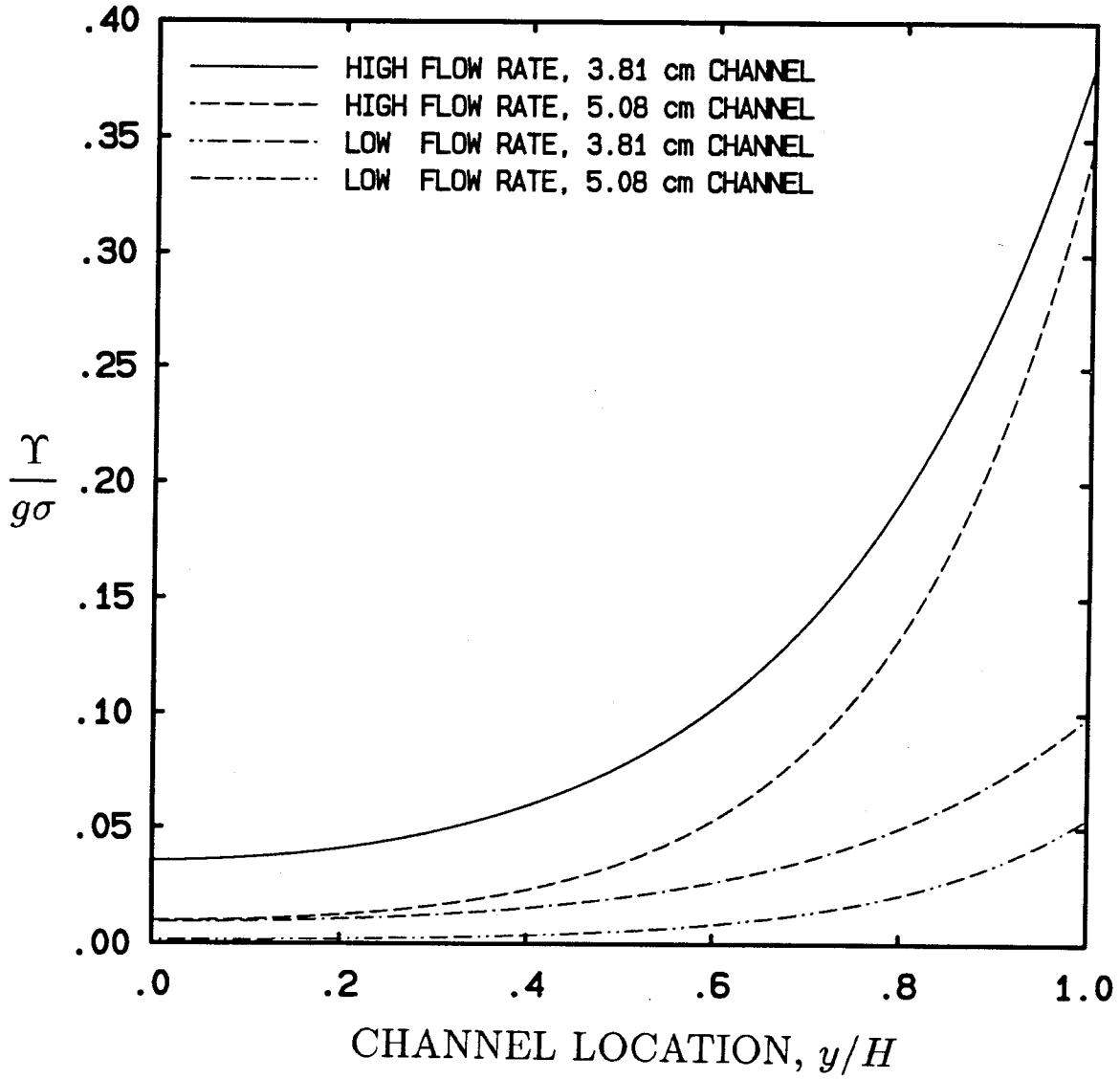

Figure 4.6: The calculated granular-temperature distributions, $\Upsilon/(g\sigma)$, for the four different flow conditions in the rough-walled channel.

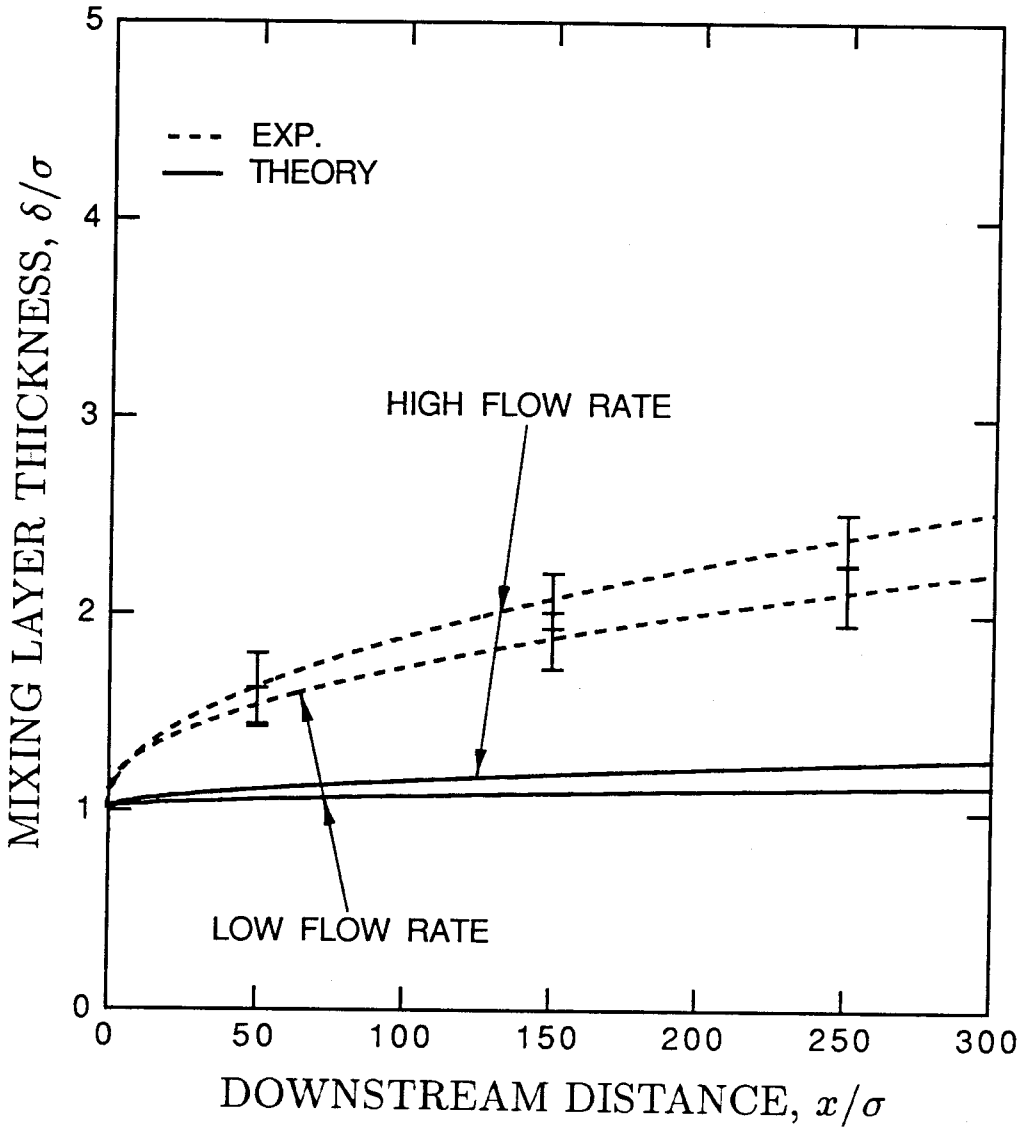

Figure 4.7: The growth of the mixing-layer thickness for the wide rough-walled channel. The dashed lines are found by curve fitting the experimental data shown in Figure 3.15, and the error bars are for ± one standard deviation.

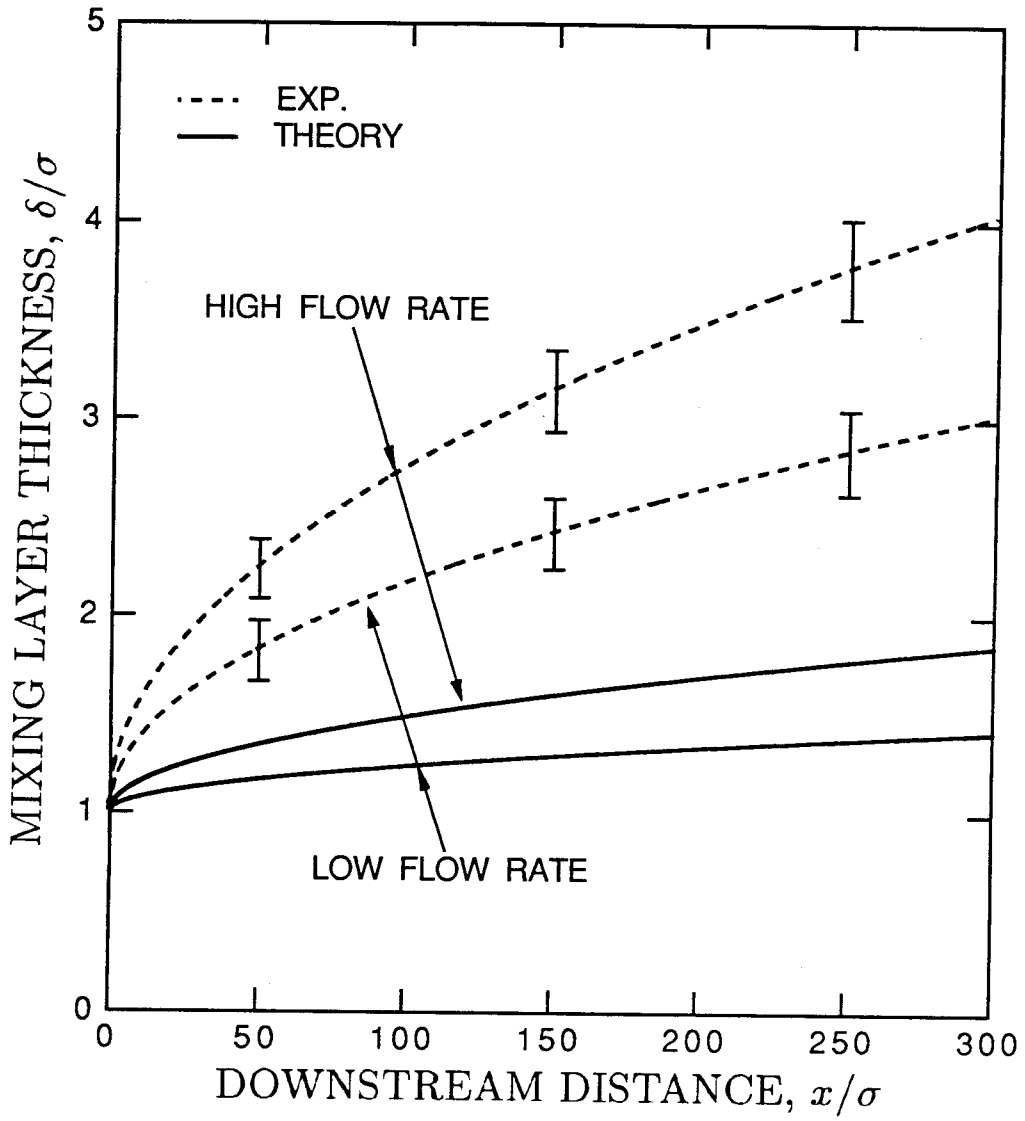

Figure 4.8: The growth of the mixing-layer thickness for the narrow rough-walled channel. The dashed lines are found by curve fitting the experimental data shown in Figure 3.16, and the error bars are for ± one standard deviation.

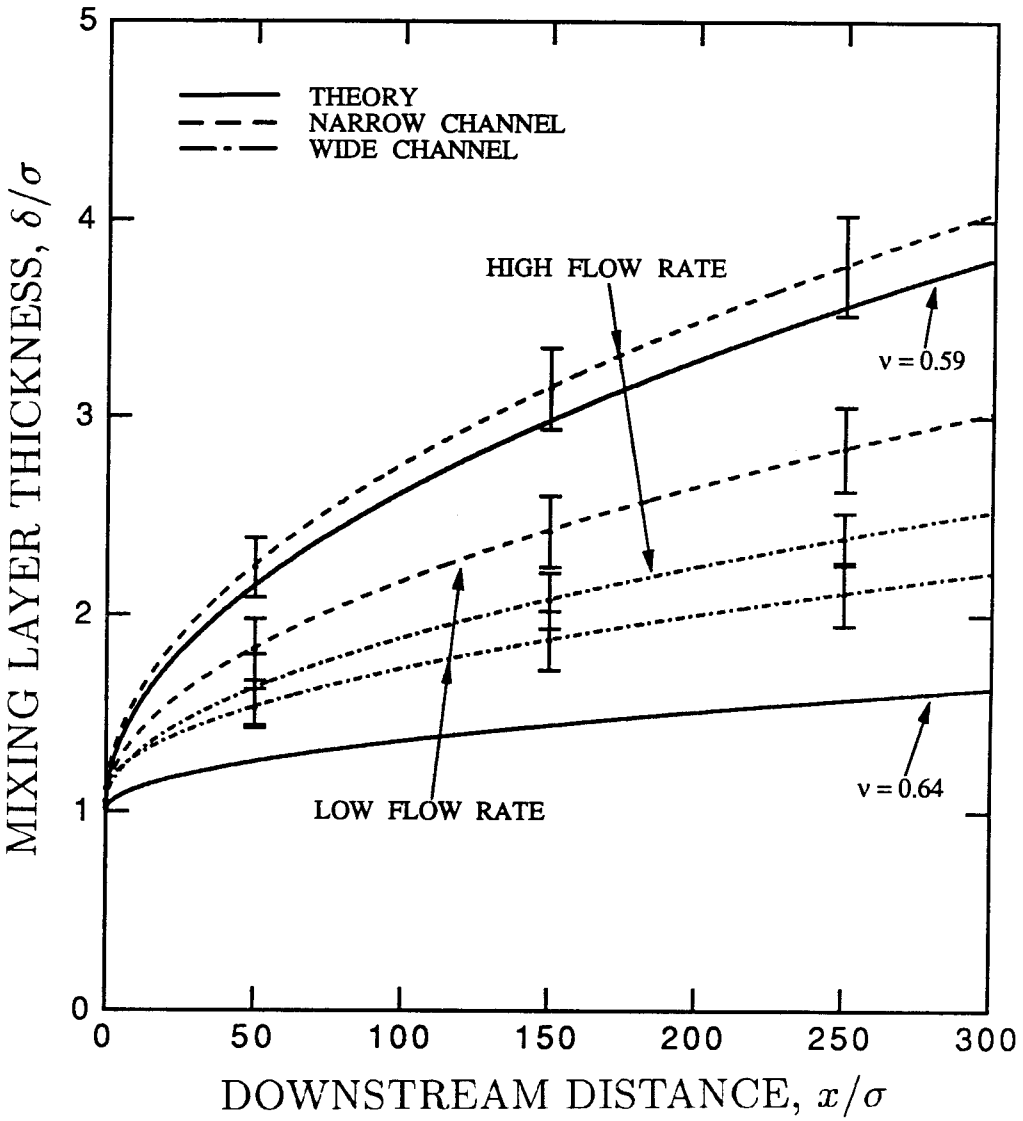

Figure 4.9: The growth of the mixing-layer thickness for the four conditions in the rough-walled channel. The dashed lines are found by curve fitting the experimental data shown in Figures 3.15 and 3.16, and the error bars are for ± one standard deviation.

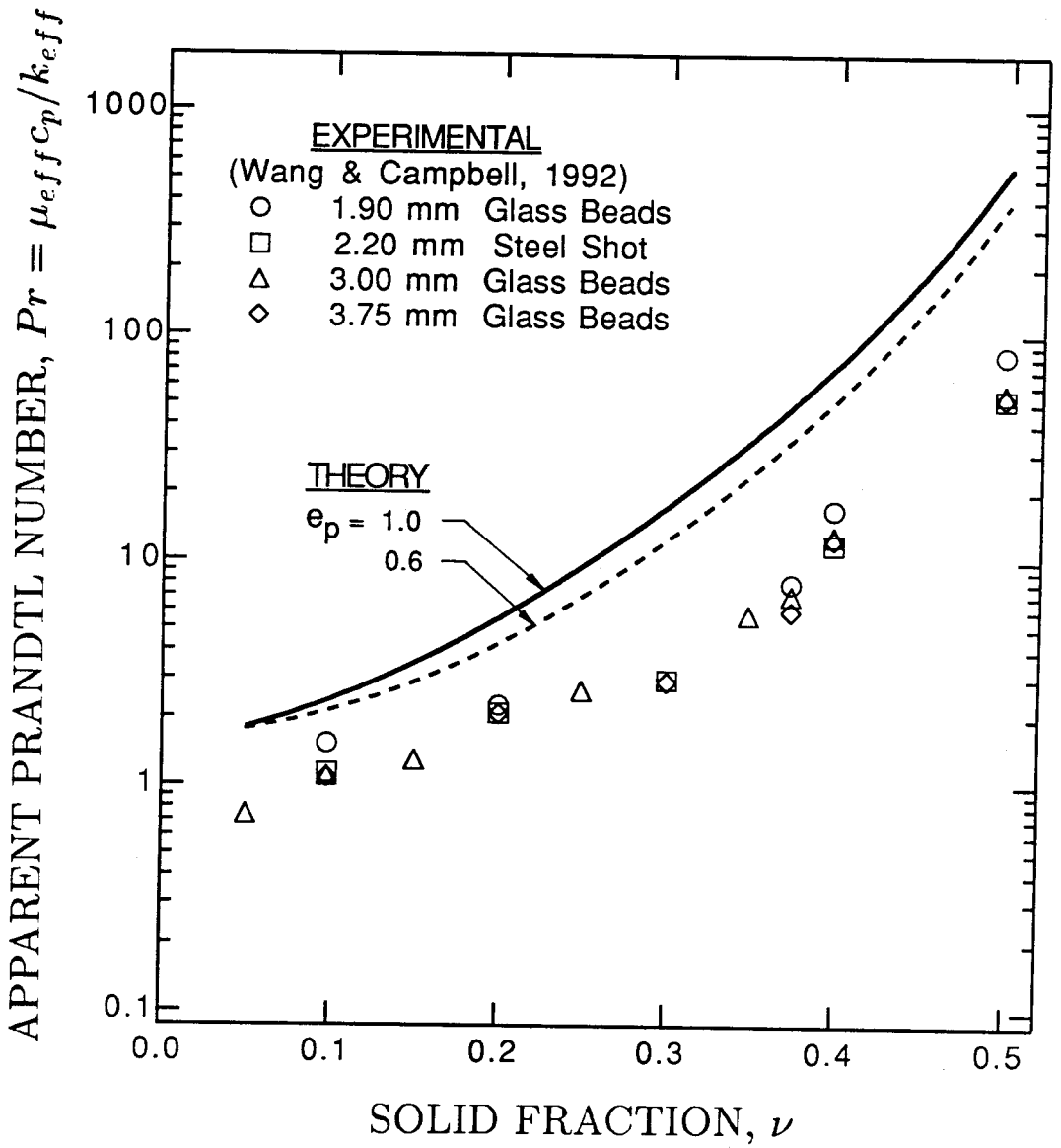

Figure 4.10: Comparison of the theoretical predictions for the apparent Prandtl number with the experimental shear-flow measurements by Wang and Campbell (1992).

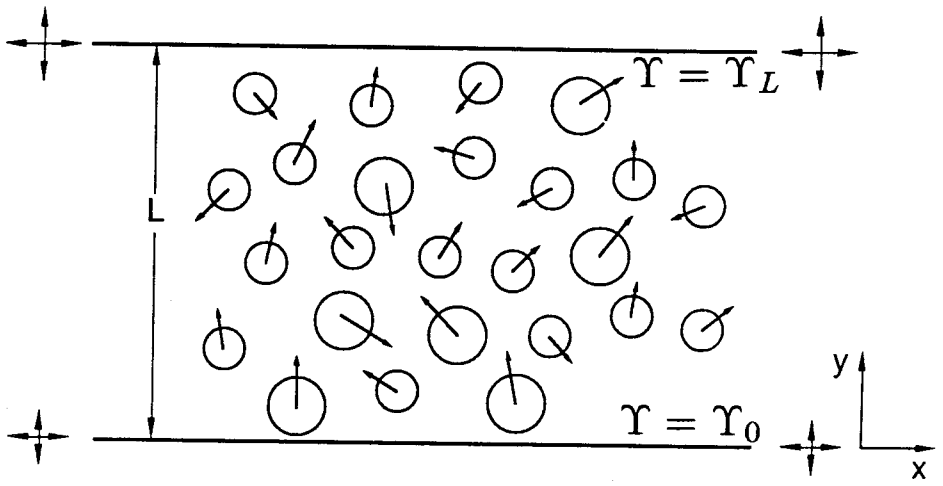

Figure 5.1: Configuration of an oscillatory no-flow system.

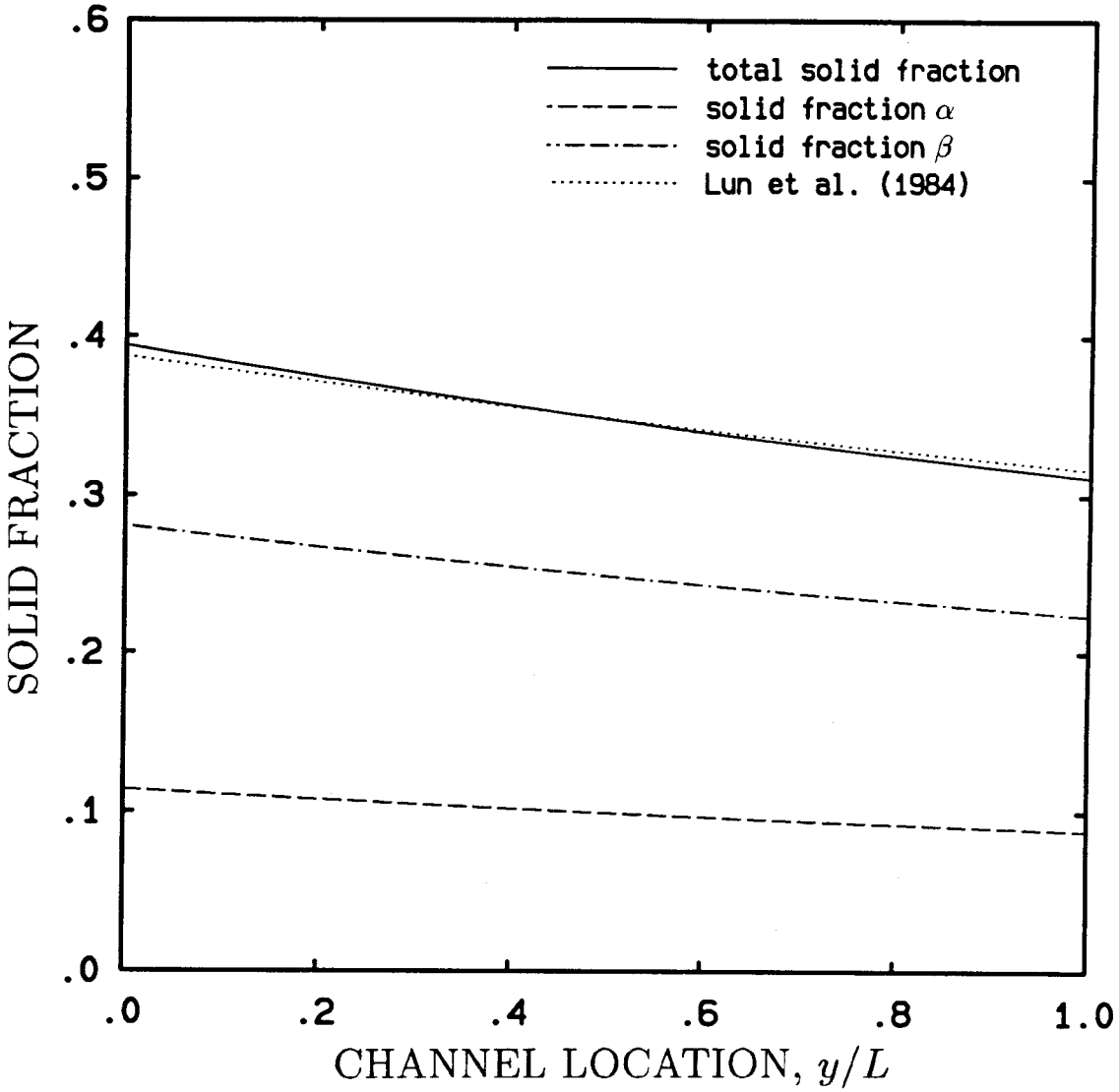

Figure 5.2: The distributions of solid fractions when two species are identical (case (a)). The dotted line is calculated from the theory of Lun et al. (1984) for the single-size material.

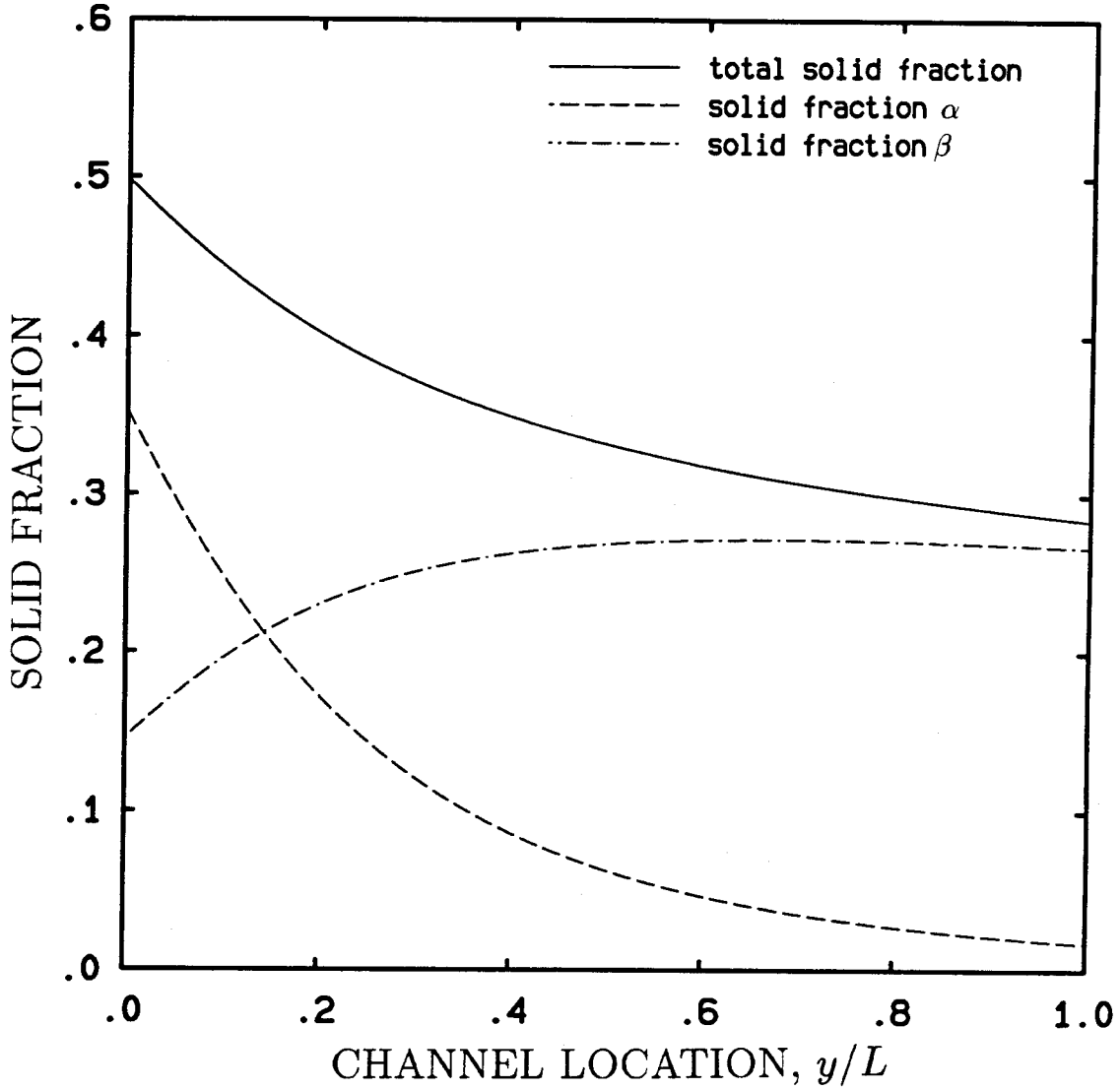

Figure 5.3: The distributions of solid fractions for case (d): $\sigma_\alpha = 2$-mm, $\sigma_\beta = 1$-mm.

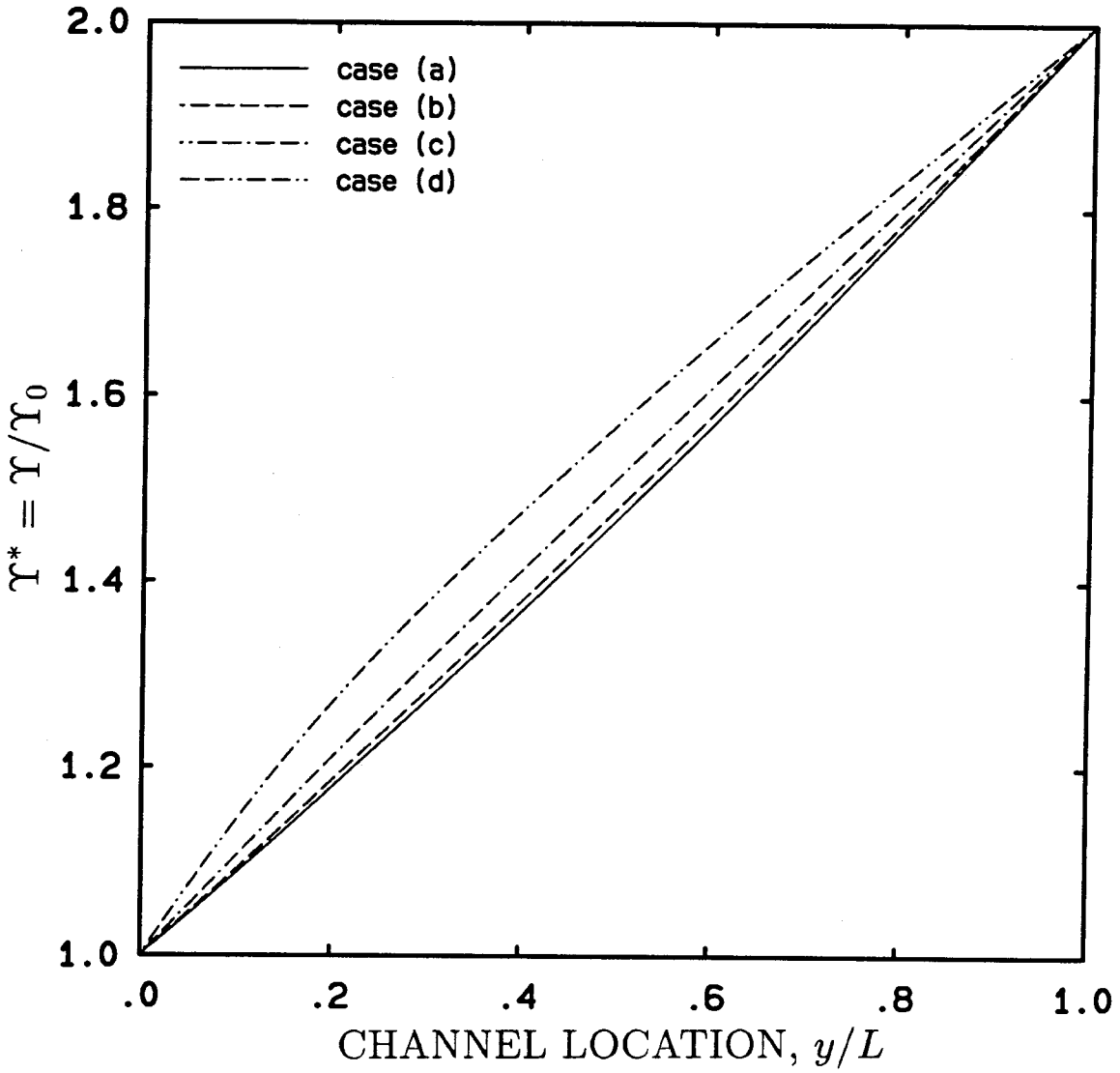

Figure 5.4: Granular temperature distributions for four different sizes of α: (a) σ_α = 1-mm, (b) σ_α = 1.2-mm, (c) σ_α = 1.5-mm, (d) σ_α = 2-mm.

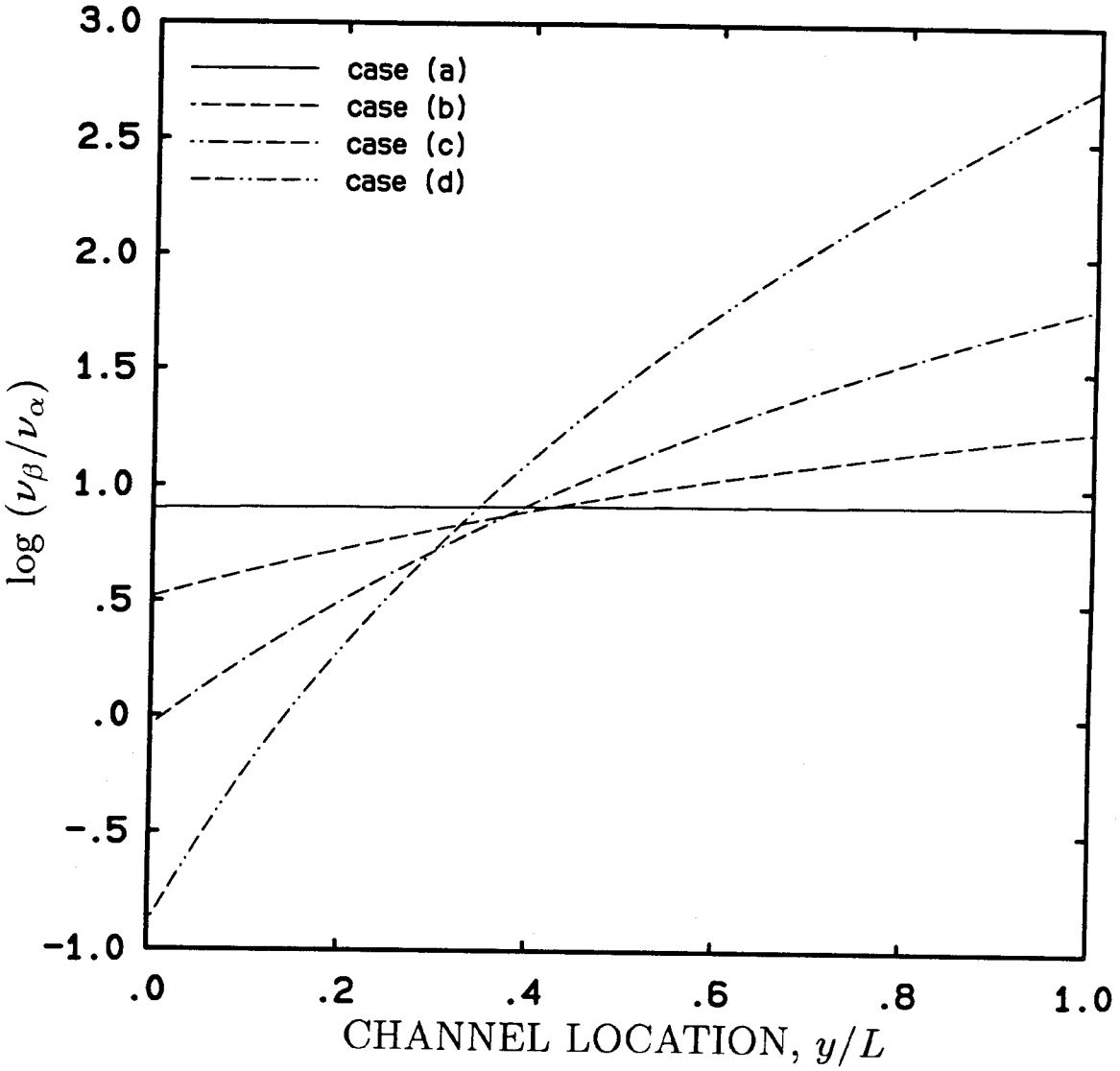

Figure 5.5: The distributions of the ratio of ν_β/ν_α for the four cases.

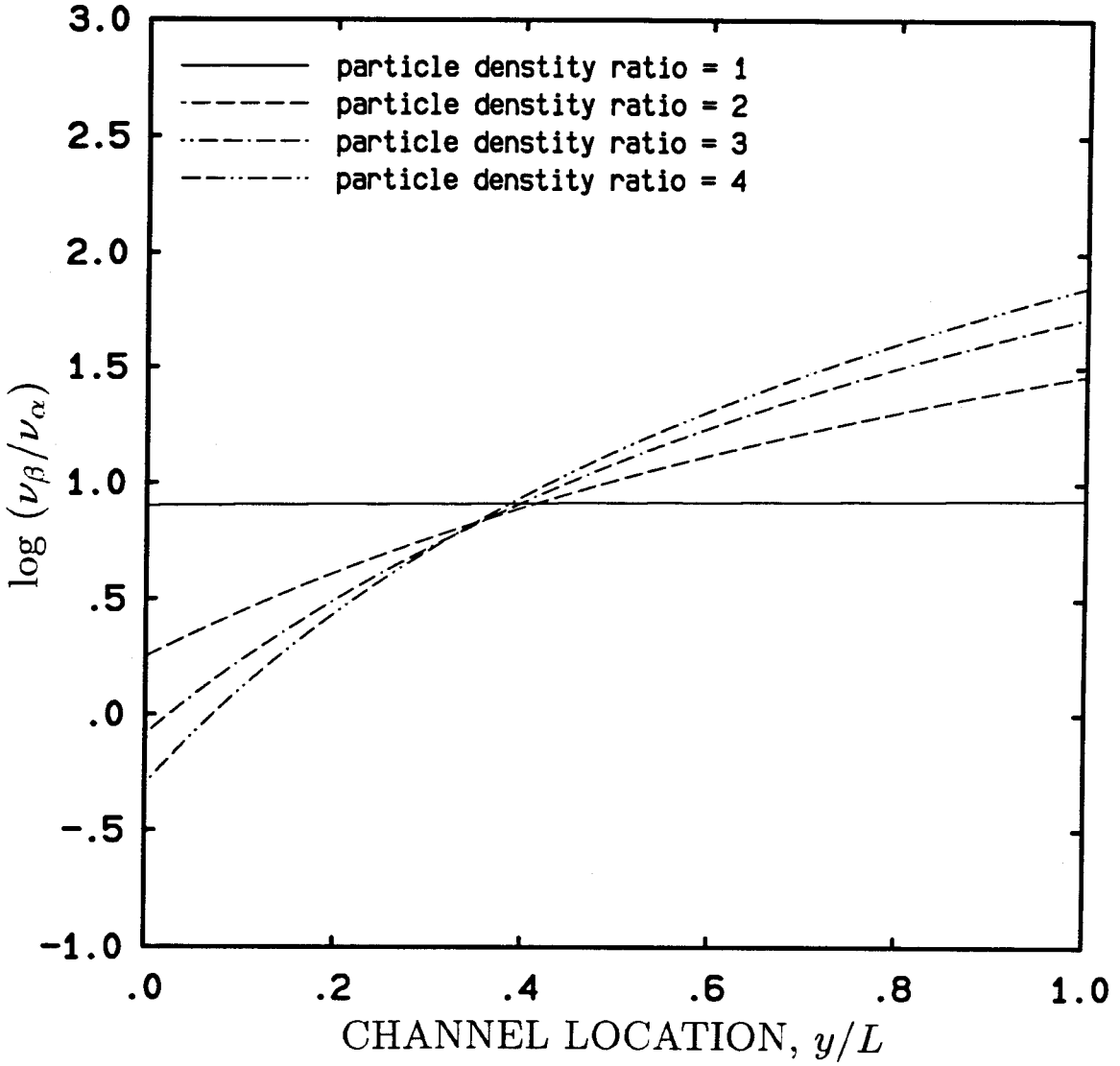

Figure 5.6: The distributions of the ratio of ν_β/ν_α for four different $\rho_{p\alpha}/\rho_{p\beta}$.

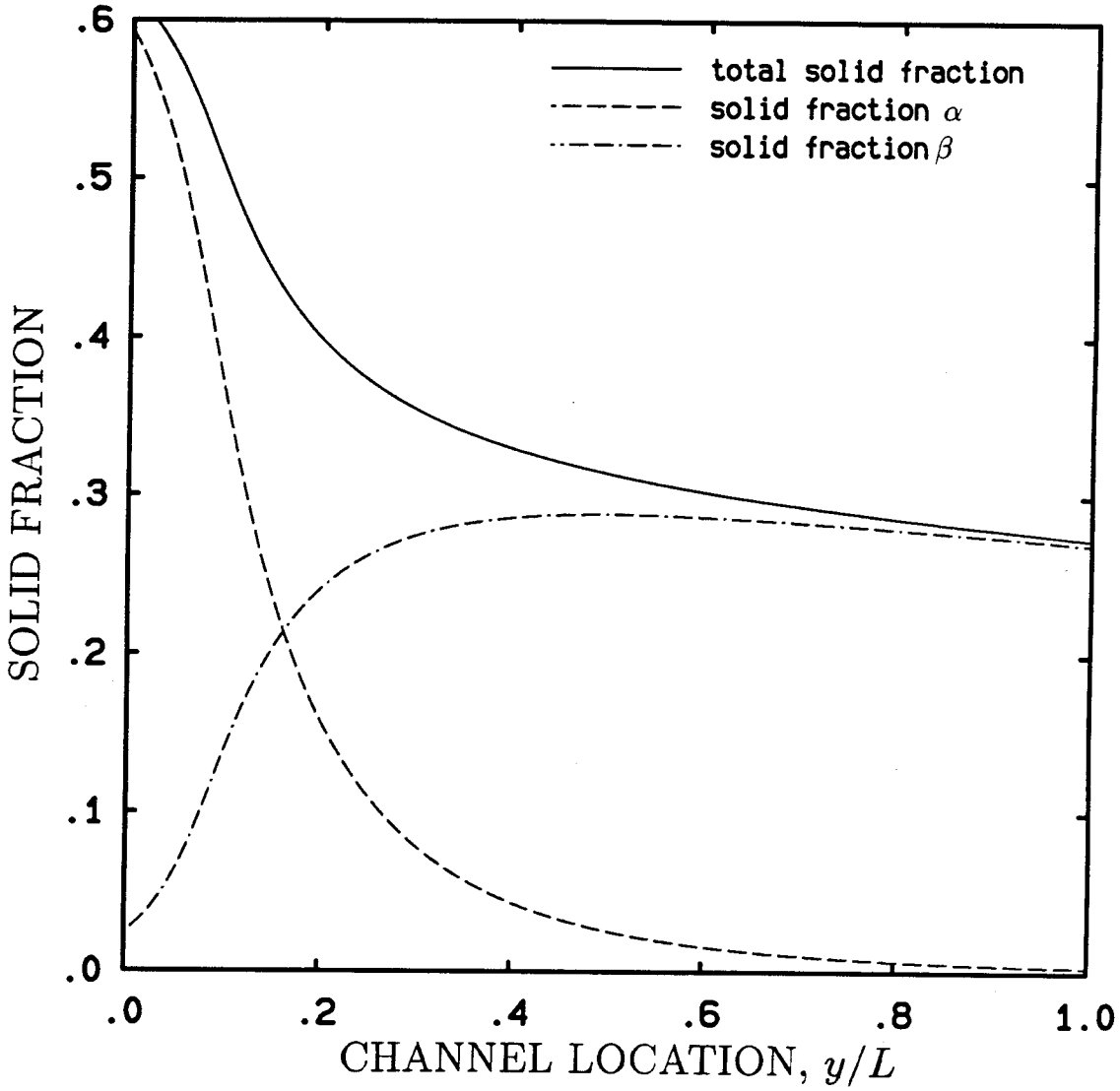

Figure 5.7: The distributions of the solid fractions for $\Upsilon_L/\Upsilon_0 = 3$, $\sigma_\alpha/\sigma_\beta = 2$, and $\rho_{p\alpha}/\rho_{p\beta} = 4$.

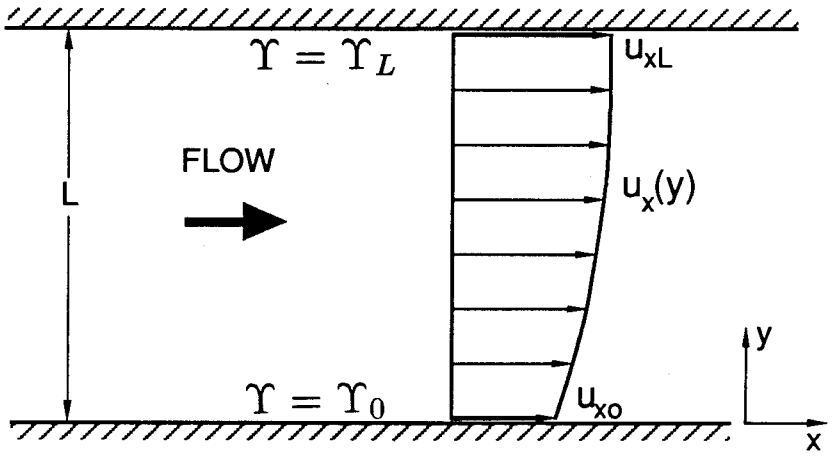

Figure 5.8: Configuration of a shear flow.

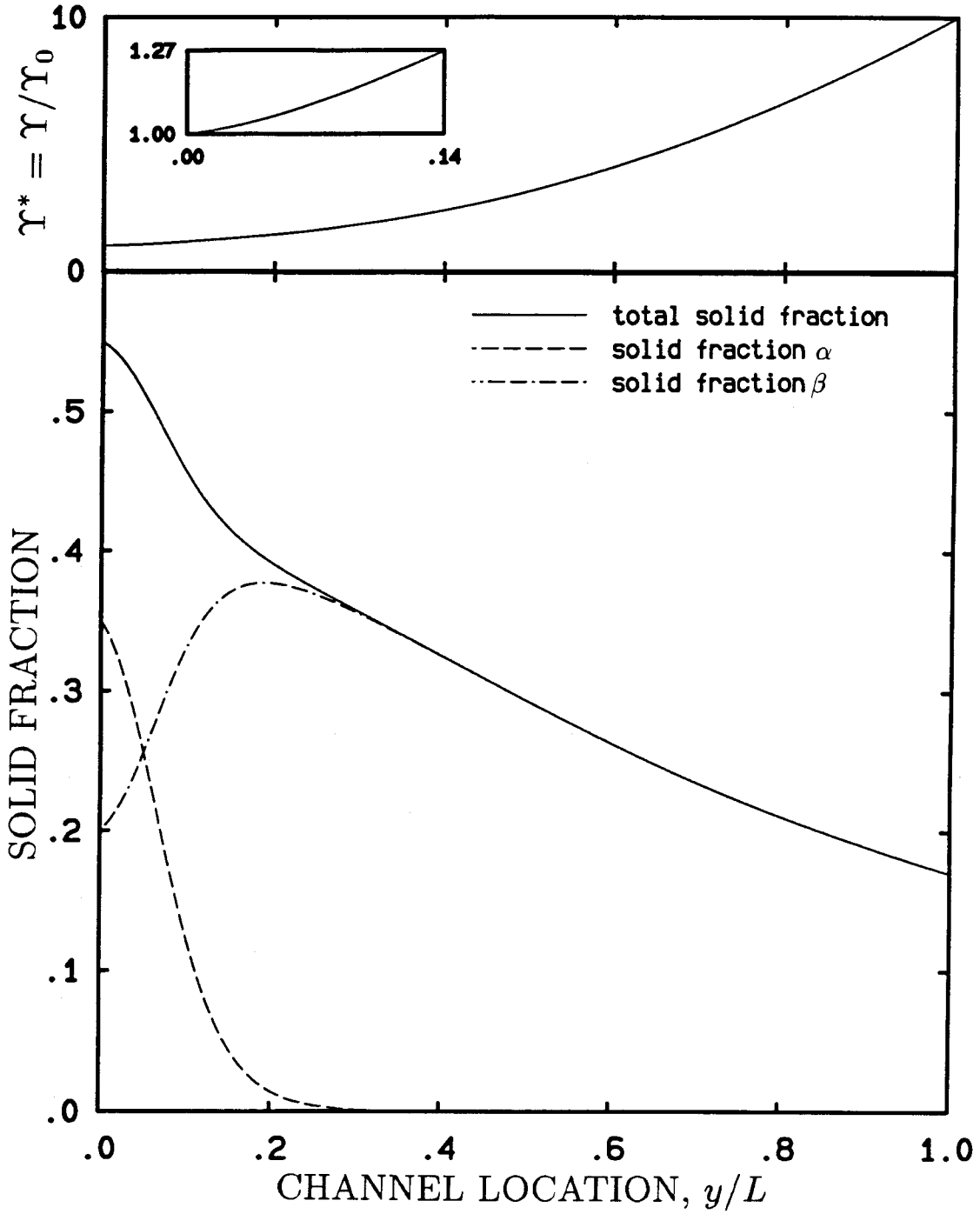

Figure 5.9: Granular temperature and solid fraction distributions in a shear flow for $T_L^* = 10$, $\overline{\nu_\alpha} = 0.03$, $\overline{\nu_\beta} = 0.28$, and $R_1 = 2.9$.

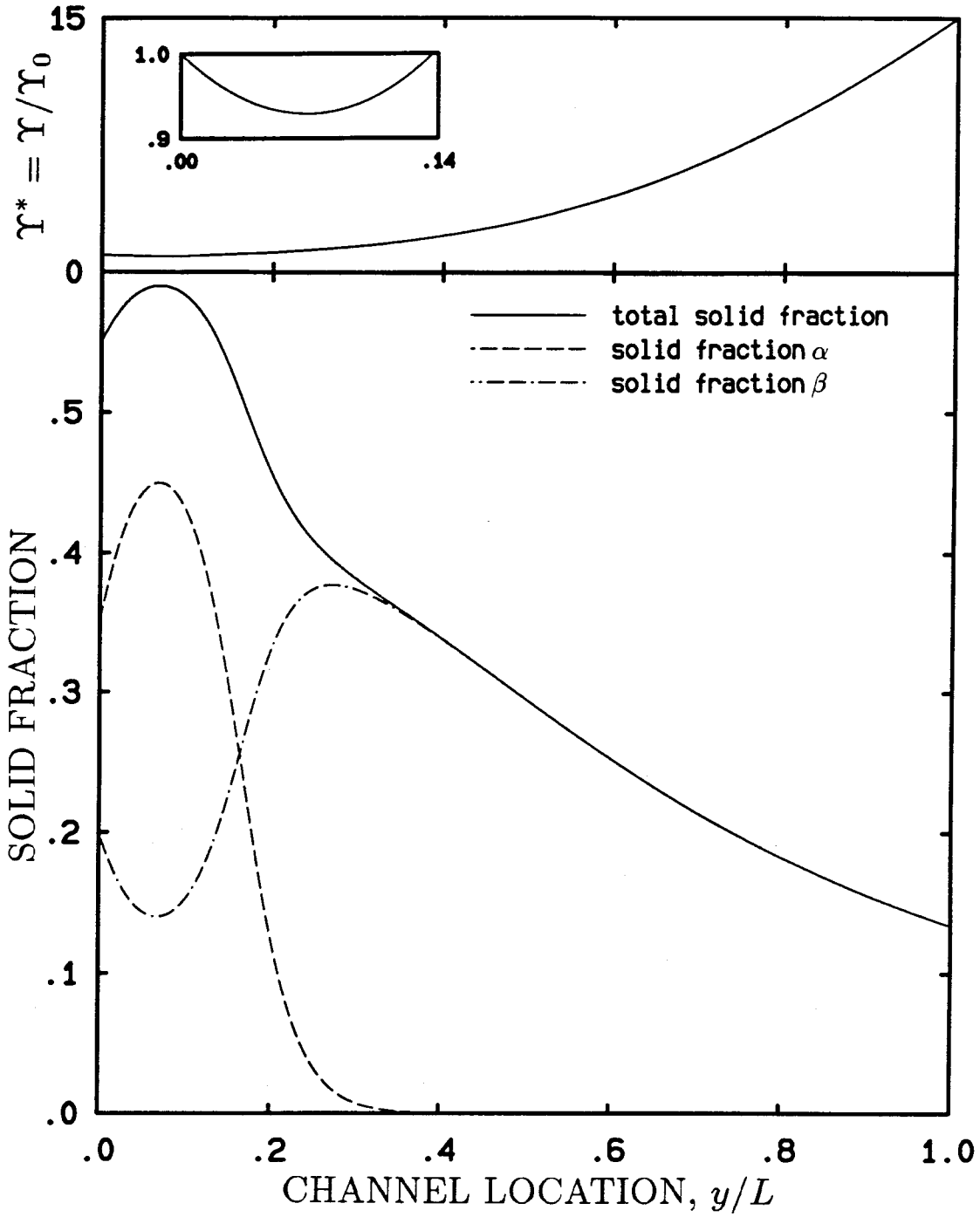

Figure 5.10: Granular temperature and solid fraction distributions in a shear flow for $T_L^* = 15$, $\overline{\nu_\alpha} = 0.08$, $\overline{\nu_\beta} = 0.25$, and $R_1 = 2.5$.

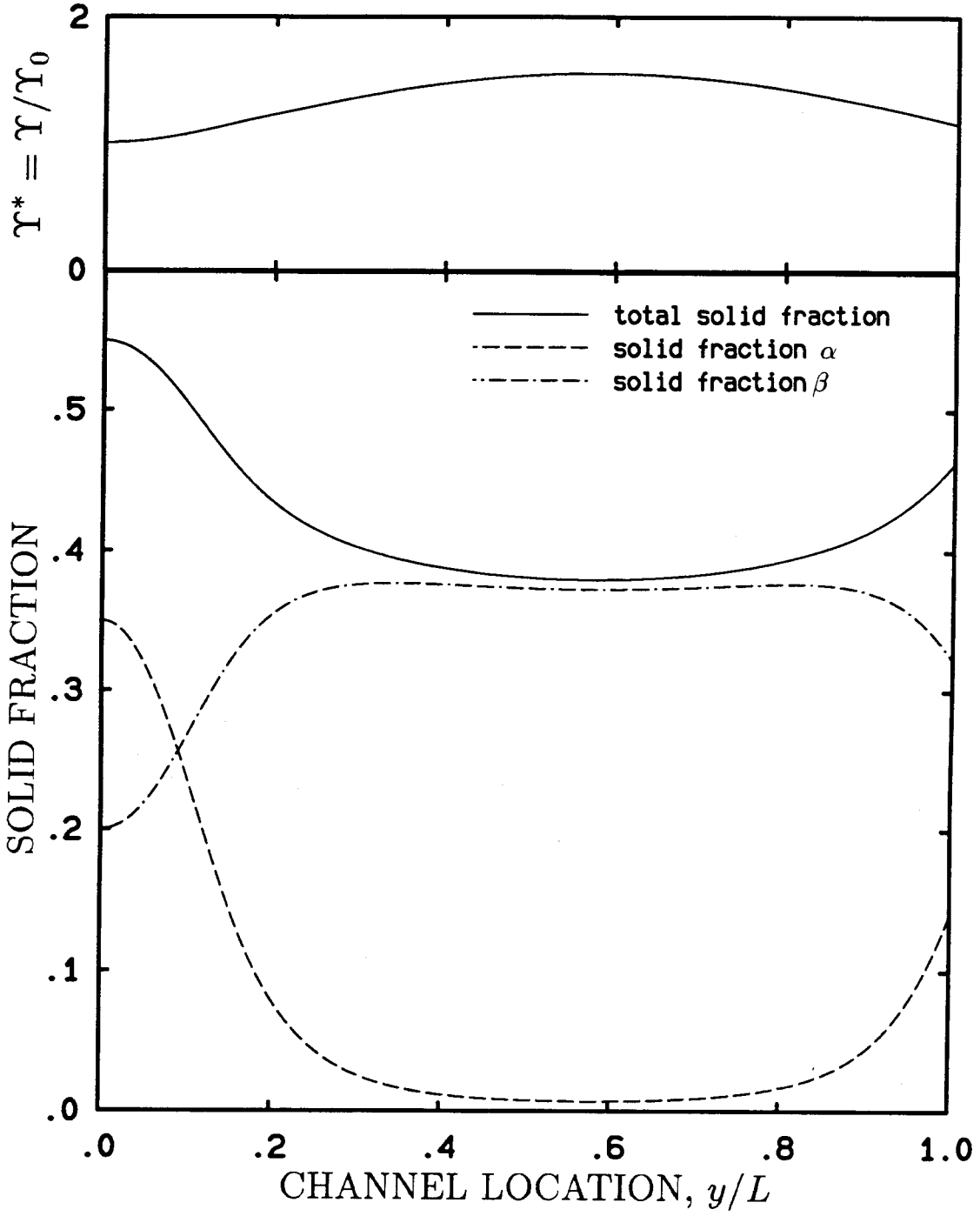

Figure 5.11: Granular temperature and solid fraction distributions in a shear flow for $T_L^* = 1.15$, $\overline{\nu_\alpha} = 0.07$, $\overline{\nu_\beta} = 0.35$, and $R_1 = 2.2$.

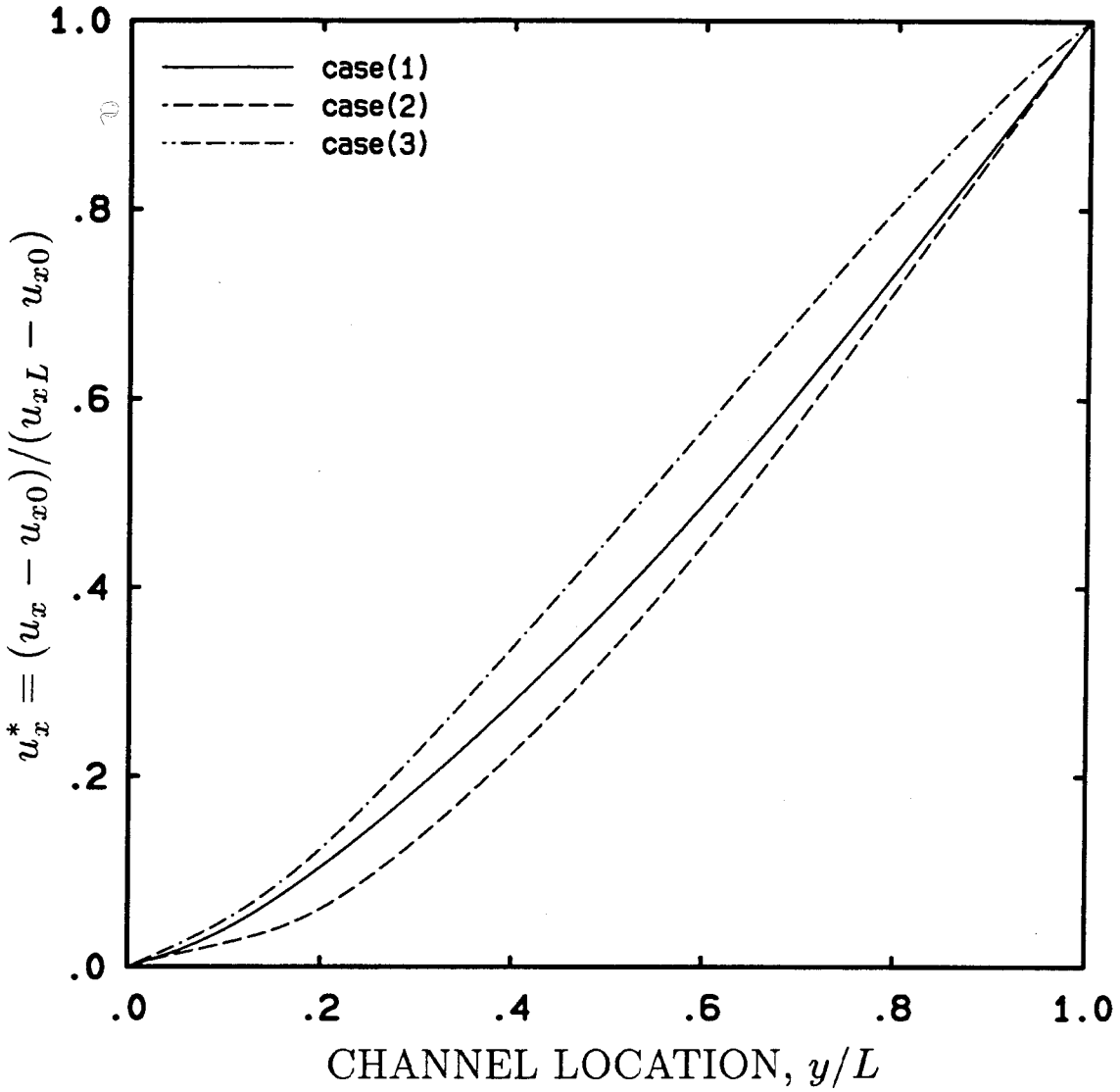

Figure 5.12: Velocity distributions for the case in Figure 5.9–5.11.

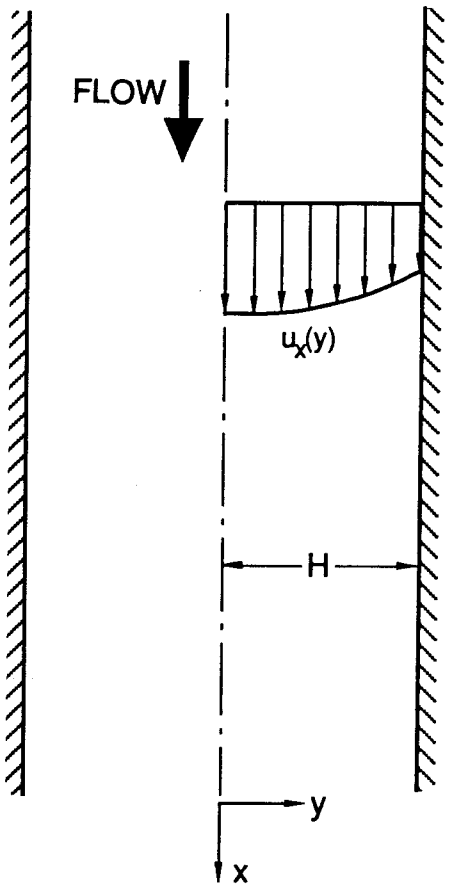

Figure 5.13: Configuration of a flow in a vertical channel.

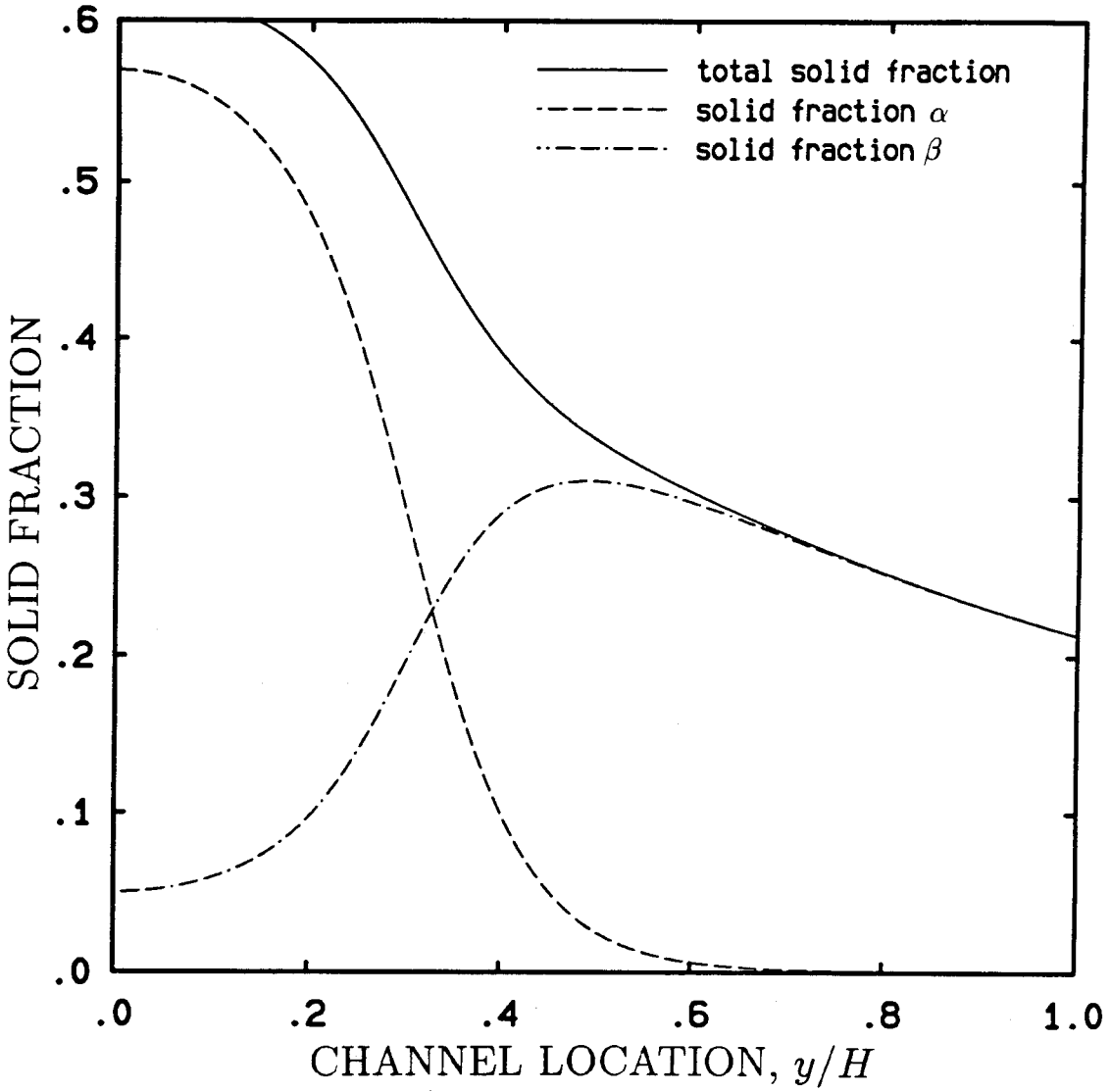

Figure A.1: Solid fraction distributions for the granular flow in a vertical channel for case (a): $\dot{m}_0 = 2.20$ kg/sec.

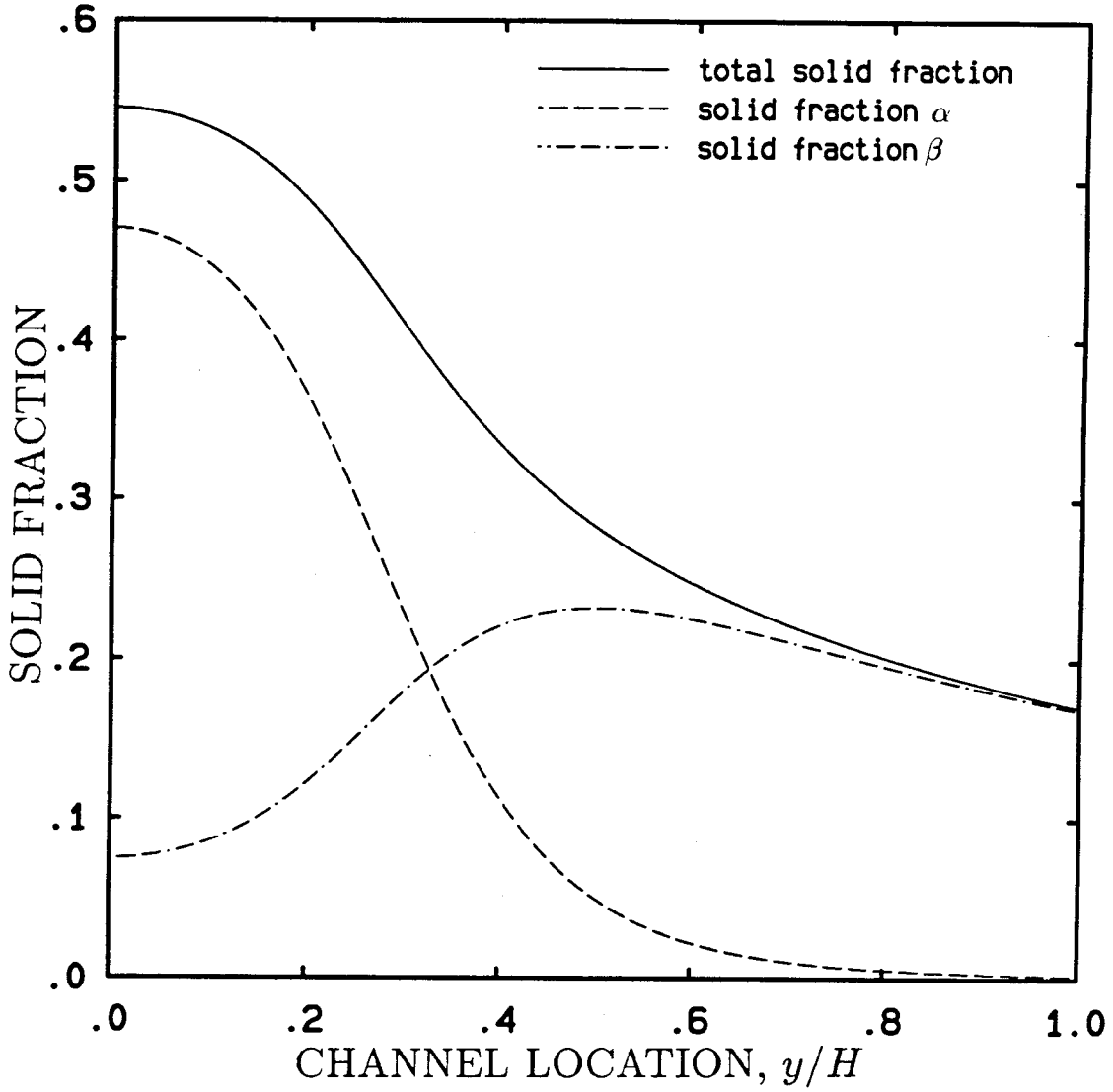

Figure A.2: Solid fraction distributions for the granular flow in a vertical channel for case (b): $\dot{m}_0 = 2.00$ kg/sec.

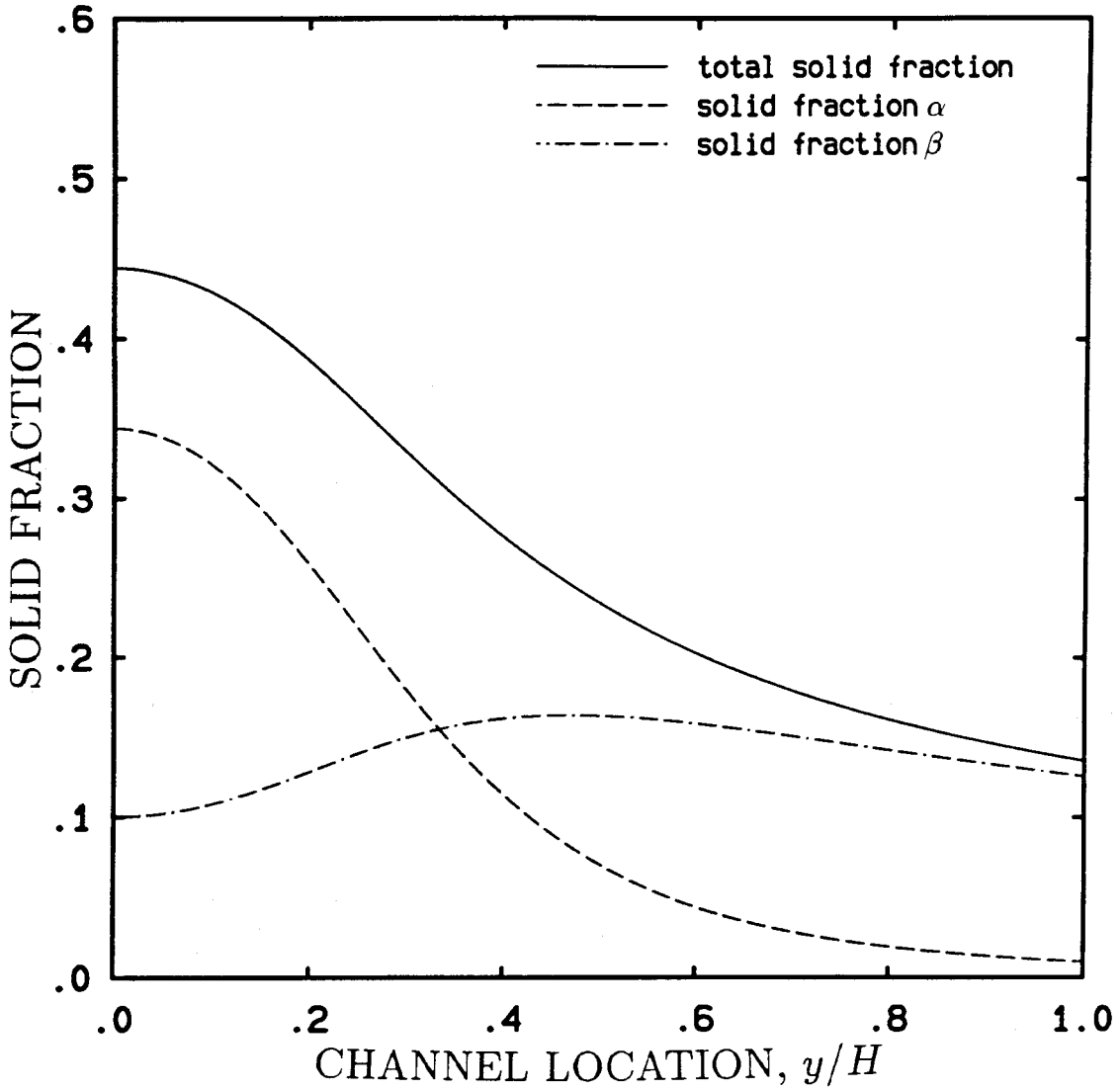

Figure A.3: Solid fraction distributions for the granular flow in a vertical channel for case (c): $\dot{m}_0 = 1.68$ kg/sec.

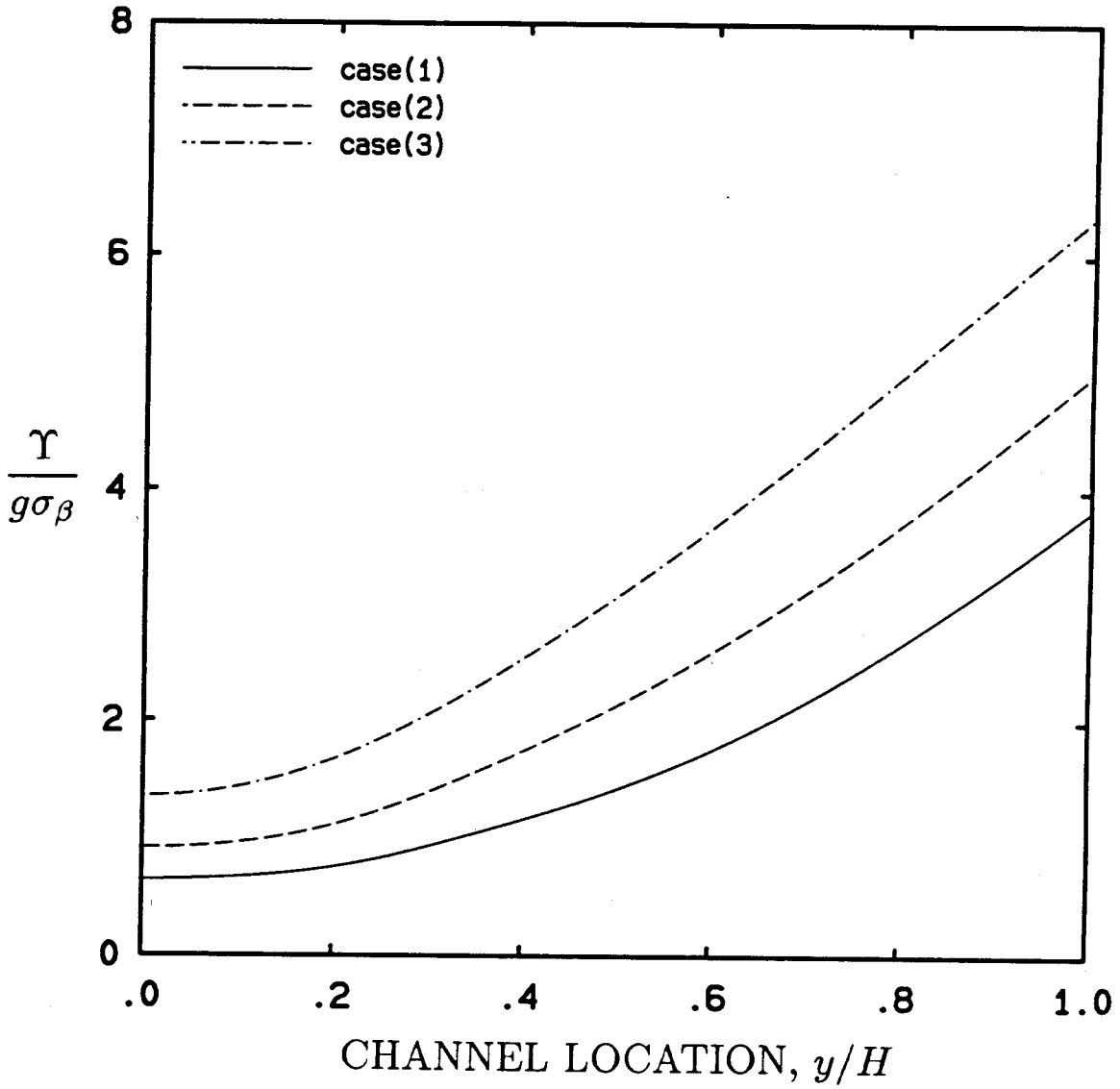

Figure A.4: Granular temperature distributions for the granular flow in a vertical channel for the three cases.

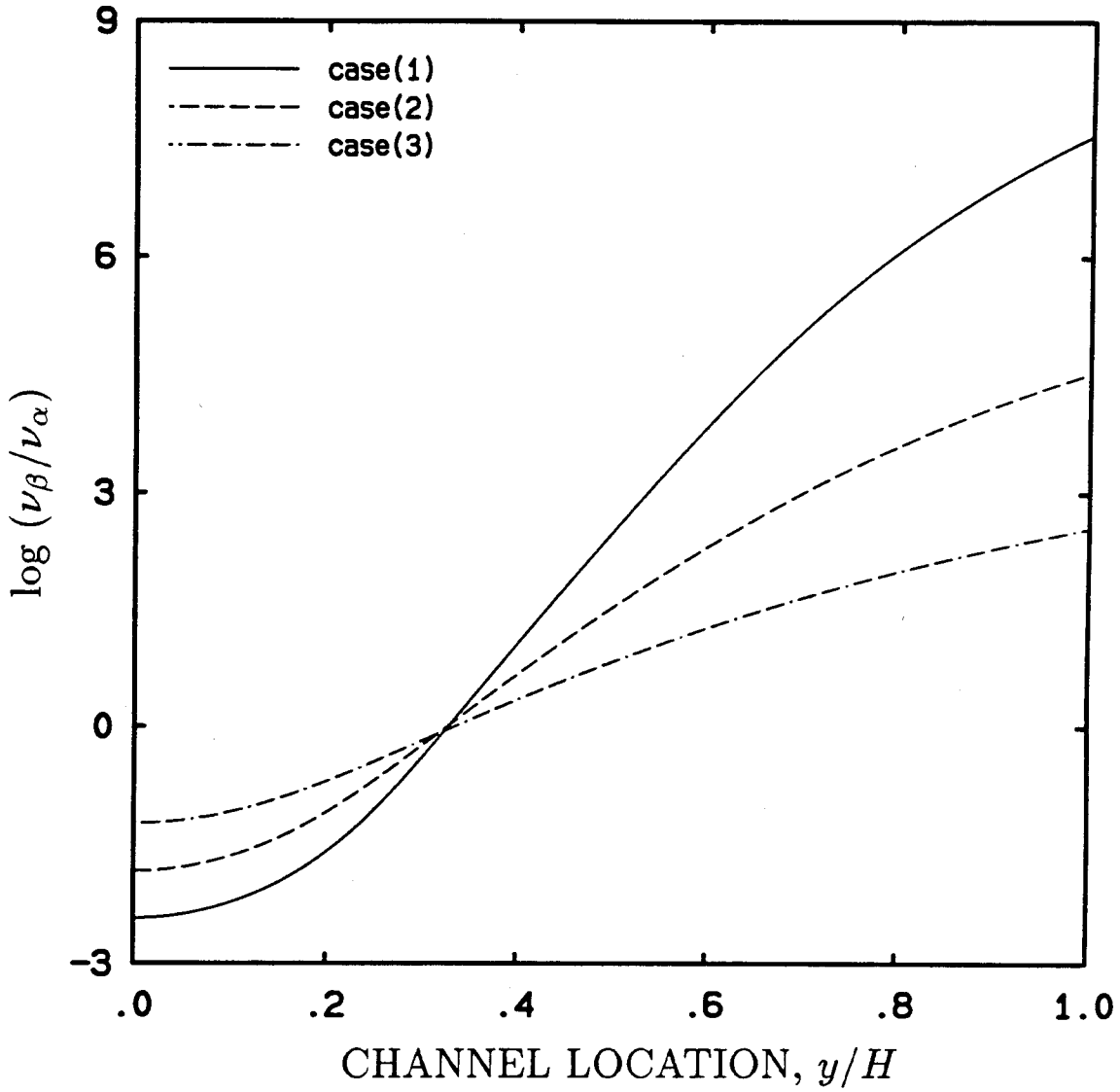

Figure A.5: The distributions of the ratio of ν_β/ν_α plotted in $\log(\nu_\beta/\nu_\alpha)$ against Y.

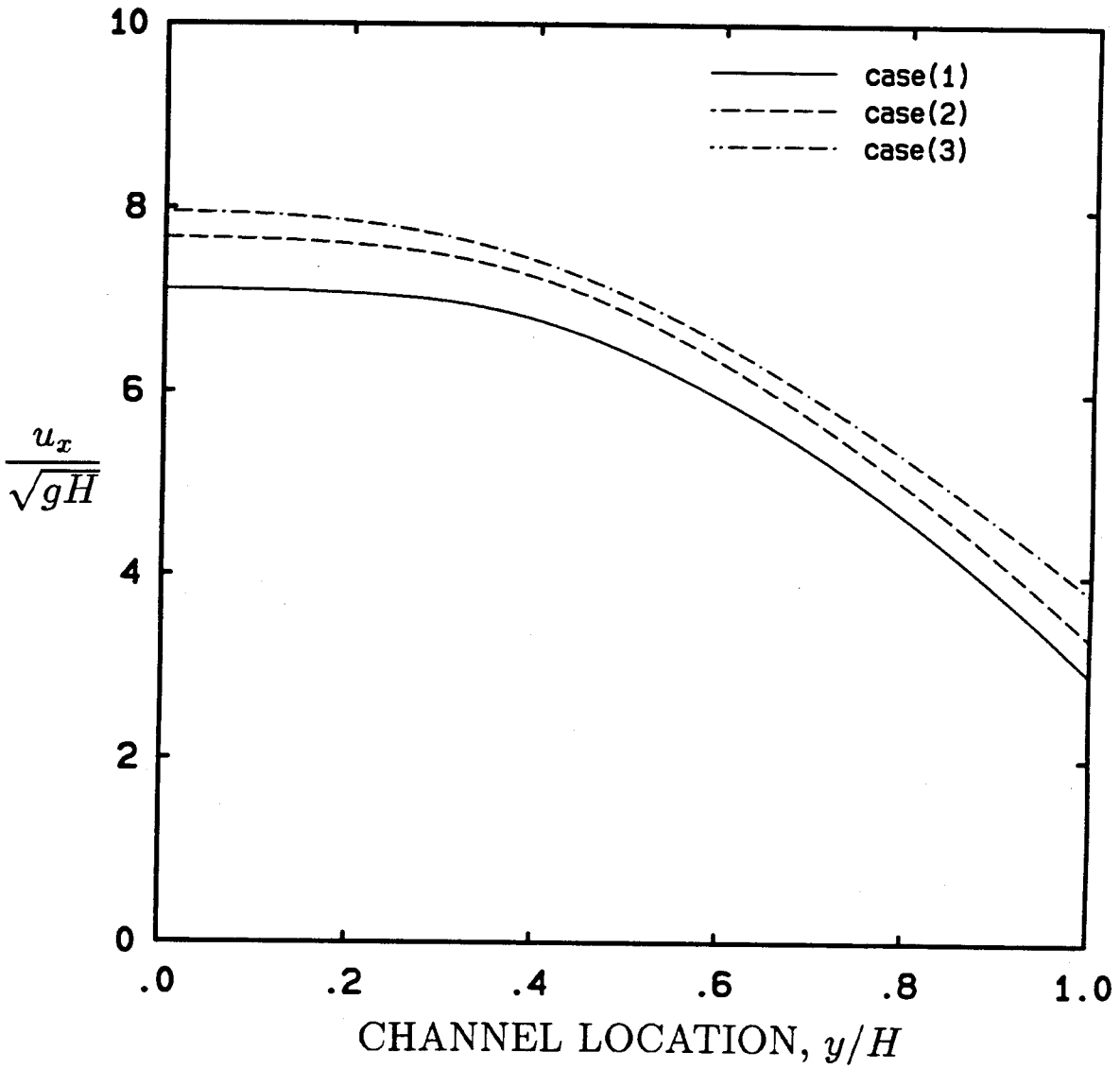

Figure A.6: Velocity distributions for the granular flow in a vertical channel.